The Technical Design of the Hall-D Polarized Photon Beam at the Thomas Jefferson National Accelerator Facility.

The GlueX Collaboration

October 28, 2008

Version 0.1

The Technical Design of the Hall-D Polarized Photon Beam at the Thomas Jefferson National Accelerator Facility

Contents

Chapter 1

Introduction

One of the unique opportunities presented by a CEBAF upgrade to energies of 12 GeV and beyond is the possibility of generating high-intensity continuous photon beams for high-energy photoproduction experiments. In this regime, photon beams represent an interesting extension to the meson spectroscopy program that has been actively pursued using beams of pseudoscalar mesons at hadron accelerator laboratories: with high energy photons one has essentially a beam of *vector* mesons. It is difficult, in fact, to conceive of any other way to obtain such a vector beam.

A key component of the 12 GeV Jefferson Lab upgrade is the GlueX experiment, devoted to the search for mesons with gluonic excitations. The experiment requires a photon beam with energies in the range 8-9 GeV and linear polarization. The preferred method for producing such a beam is coherent bremsstrahlung in an oriented crystal. Electrons of 12 GeV from the accelerator pass through a thin diamond radiator, generating an intense beam of high-energy photons with a continuous energy spectrum that is dominated by a single peak. A significant fraction of the total power in the beam is concentrated inside this peak, which has a width of less than 5% f.w.h.m. At a fixed electron beam energy E_0, the peak energy of the photon beam can be varied anywhere up to 90% E_0 simply by rotating the crystal. The photon spectrum inside the intensity peak has a large degree of linear polarization. The precise energy of an individual photon inside the peak is determined ("tagged") from the momentum of the recoil electron measured in a dedicated tagging spectrometer.

This report begins with a survey of the techniques for producing high-energy photons that were considered in the development of this design, and the reasons for the choice of coherent bremsstrahlung. The coherent bremsstrahlung source is then described in greater detail, followed by a discussion of the requirements that the design places on the electron beam properties at the source. The tagging spectrometer design is described next, followed by the photon beam collimation and shielding design. The report concludes with a description of the pair spectrometer and methods for monitoring the properties of the beam.

Chapter 2

Choice of technique

Two basic methods have been considered for producing photons of the highest possible energy, flux and polarization from electrons of 12 GeV. The methods are bremsstrahlung and Compton scattering of light. Both are well-established methods of producing photon beams, and both are actually described by the same set of Feynman diagrams, shown in Fig. 2.1. In the case of Compton scattering the incoming photon is real, whereas it is virtual for the case of bremsstrahlung.

Each of these techniques has its own limitations and advantages. In order to be suitable for GlueX, the photon source must be capable of producing photons of 80% E_0 with a significant degree of linear polarization. The energy resolution for individual photons in the beam should be better than 0.5%, ideally on the same order of magnitude as the energy spread of the electron beam itself. It should be capable of producing intensities up to 10^8/s in the range 8-9 GeV, with the flux outside the desired energy band as low as possible.

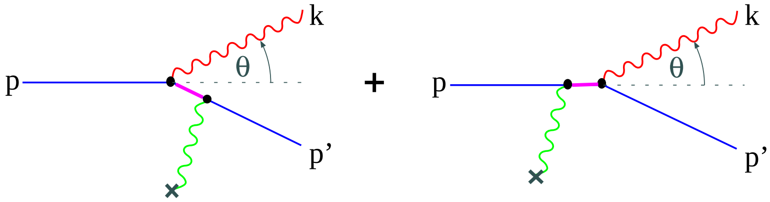

Figure 2.1: Generic diagrams for hard photon production from a high energy electron beam. The symbol × represents either a static charge distribution, in the case of virtual photons in the initial state (i.e. bremsstrahlung), or an optical cavity, in the case of real photons in the initial state (i.e. Compton scattering).

It is also important that the source be reliable and require a minimum of downtime for maintenance. The suitability of each approach is discussed below in the light of these criteria.

2.1 Compton back-scatter

A Compton source begins with a beam of visible or ultraviolet light, typically from a laser, that is aligned to intersect the incident electron beam at close to 180°. Some of the photons undergo Compton scattering with the beam electrons. In the lab frame, the scattered photons emerge in a narrow cone about the incident electron direction and carry a significant fraction of the electron energy.

The basic design of the Compton back-scatter source for this study was put forward by C. Keppel and R. Ent [1]. The design entails the use of a four-mirror high-gain cavity pumped by a 10 kW argon-ion laser putting out 2 ps pulses at a frequency of 100 MHz. The pulses in the cavity are synchronized so that the light pulses intercept an electron bucket each time they pass through the beam. The total length of the cavity is 2 m with a crossing angle of 1°. Both cavity and electron beam are focused to a tiny spot of 10 microns r.m.s. radius at the crossing point. A small spot size is necessary in order to get as high a scattering rate as possible. The gain of the cavity is 10^4, which is achievable using high-reflectivity dielectric mirrors. The wavelength of the light is 514 nm. The rate spectrum of the back-scattered beam from this source is shown in Fig 2.2a for a 1 μA electron beam at 12 GeV.

From the point of view of flux, this source is marginal. With a few μA of beam and mirror improvements, it might produce 10^8 photons/s in the upper $\frac{1}{3}$ of its energy spectrum. However, its maximum photon energy of 3.7 GeV is far below the 9 GeV needed for GlueX. To remedy this, a shorter wavelength light source is required. This can be achieved by the use of a frequency-doubling crystal that absorbs 514 nm light from a green laser and produces ultraviolet light at 257 nm. Storing this light in a cavity of similar design to that described above yields the back-scatter rate spectrum shown in Fig. 2.2b. The major reason for the drop in rate is the decrease in the cavity gain from 10000 to 250 imposed by the diminished reflectivity of mirrors in the UV. Other loss factors are the inefficiency of the doubling crystal, the factor two in rate from the doubling itself, and the decreasing Compton cross section with increasing energy. The maximum photon energy is still under 6 GeV and the flux is three orders of magnitude below the desired rate.

In order to reach photon energies of 9 GeV, a source of 20 eV light is

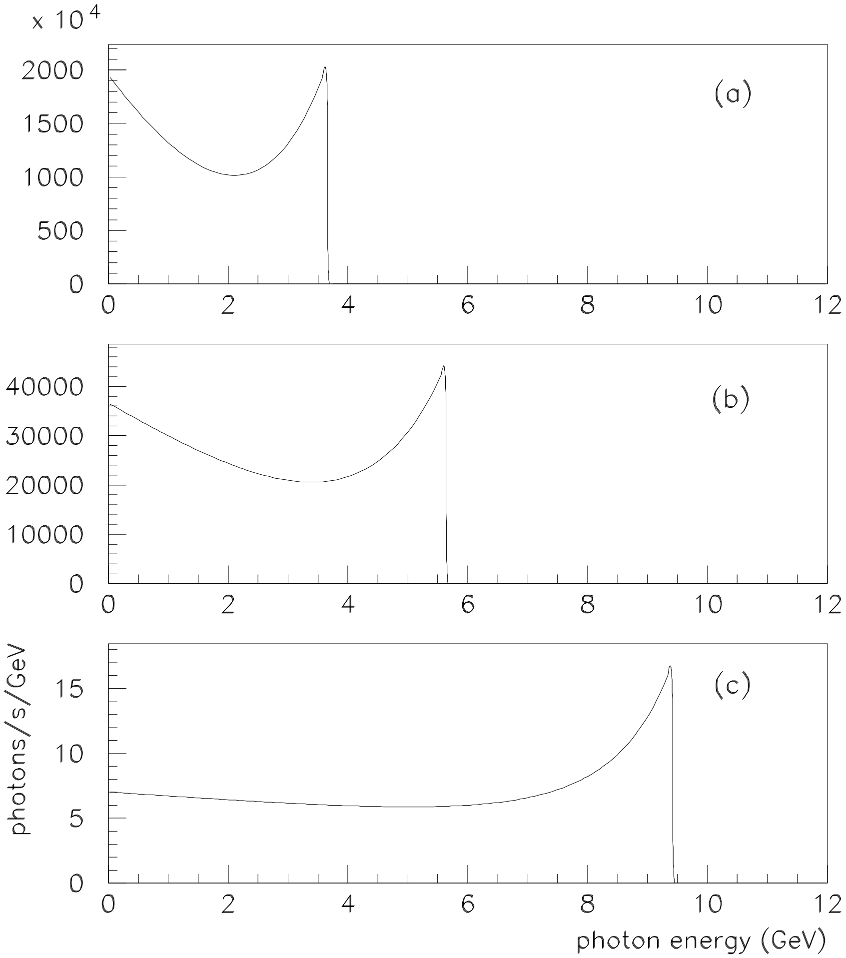

Figure 2.2: Photon energy spectrum from the Compton back-scatter source described in the text and a 12 GeV electron beam at $1\,\mu A$: (a) cavity of gain 10000 driven by a 10 kW Argon-ion laser (514 nm) at 100 MHz, (b) cavity of gain 250 driven by 3 kW frequency-doubler (257 nm) pulsed at 100 MHz, and (c) cavity of gain 1 driven by a hypothetical FEL source operating at 20 eV with the same time structure as CEBAF beam, peak power 1 kW.

needed. The brightest source of 20 eV photons would be synchrotron radiation. Mirrors that operate at these wavelengths typically have reflectivities around 70%. With these one could conceive of a scheme that uses a wiggler to extract energy from the 12 GeV beam before it enters the dump. This light would have the same time structure as the incident beam, and so it could be reflected back and made to cross the incident beam at a small angle for a Compton back-scatter source. An indication of the level of flux that could be achieved with such a source can be obtained by using the laser cavity model described above, setting the gain of the cavity to 1, the wavelength to 62 nm, and assuming 1 kW peak (1 W average) of synchrotron light within the peak. The back-scatter rate for this source is shown in Fig 2.2c. This plot shows that even if the full power of 1 μA in the 12 GeV electron beam were converted into 20 eV photons and back-scattered from the incident beam, the rate of 9 GeV photons produced would still be less than 100 Hz, six orders of magnitude below the design intensity for GlueX.

From the point of view of polarization, the Compton back-scatter source would be ideal. The polarization of the back-scattered beam is controlled by that of the laser, and can be essentially 100%. This source is also virtually background-free because the spectrum below any desired cutoff can be eliminated by collimation. The energy of the remaining beam can be measured to within the resolution of the electron beam by tagging. However the the combination of sufficient energy and sufficient flux for the purposes of the GlueX experiment in Hall D cannot be achieved using this source.

2.2 Tagged bremsstrahlung

A bremsstrahlung source consists of a thin piece of material (the radiator) that is placed in the electron beam and converts part of the energy of the beam into bremsstrahlung radiation. Bremsstrahlung offers the only practical way, starting with an electron beam at cebaf energies, to produce a photon beam with a significant flux in the vicinity of the end point. It produces a naturally collimated photon beam with a characteristic angular spread of m/E_0. This allows the low emittance of the cebaf beam to be effectively transferred into the secondary photon beam.

Bremsstrahlung does not suffer from the kind of flux limitations that were encountered in the examination of Compton back-scatter sources. The radiator thickness must be kept below 1% of a radiation length in order to maintain good energy resolution in the tagger. Keeping the thickness below 10^{-3} radiation lengths ensures that multiple scattering in the radiator does not significantly broaden the divergence angle of the photon beam. A 10^{-3} radiator and 1 μA of electrons would produce much more than sufficient flux for GlueX.

A bremsstrahlung source is, however, deficient in some other respects. Averaged over the bremsstrahlung cone, the photon beam has zero linear polarization. Circular polarization can be achieved by polarization transfer from a circularly polarized electron beam, but for the purposes of GlueX, linear polarization is essential. A bremsstrahlung source also suffers from a large low-energy flux in the beam. The power spectrum of a bremsstrahlung beam is approximately uniform from zero up to the energy of the incident electrons. This means that an experiment that uses the high-energy part of the beam must operate in a background of low-energy photons that are many times more frequent. Photon tagging is helpful in eliminating many of the false triggers in the detector that are produced by background beam photons, but this technique is only effective during offline analysis at rates above a few 10^7 tagged photons/s. For the typical large-acceptance experiment using tagged bremsstrahlung, background from low-energy beam particles limits the rate at which the experiment can run to less than $5 \cdot 10^7$ tagged photons/s. The GlueX tagged photon beam design pushes that limit up to 10^8/s by taking advantage of *coherent* bremsstrahlung with collimation.

2.3 Coherent bremsstrahlung

The source described in the previous section meets most of the requirements for GlueX, but is deficient in the areas of polarization and backgrounds. Both of these deficiencies can be remedied by replacing the conventional amorphous or polycrystalline radiator with a thin mono-crystalline wafer. At special settings for the orientation of the crystal, the atoms in the radiator can be made to recoil together from the radiating electron. When they do this they produce a coherent enhancement at particular energies in the radiation spectrum, which correspond to the reciprocal lattice vectors of the crystal. The kinematics are such that a randomly oriented lattice vector would make a tiny peak located up at the end point of the energy spectrum, where the coherent gain factor is negligible. By careful orientation of the crystal, however, one of the lattice vectors can be aligned with the favored kinematics for bremsstrahlung, at which point its coherent peak appears well below the end point, and its coherent gain can be large enough that it contributes a large fraction of the total radiated power.

This is illustrated in Fig. 2.3. This plot shows the intensity (dP/dE) or

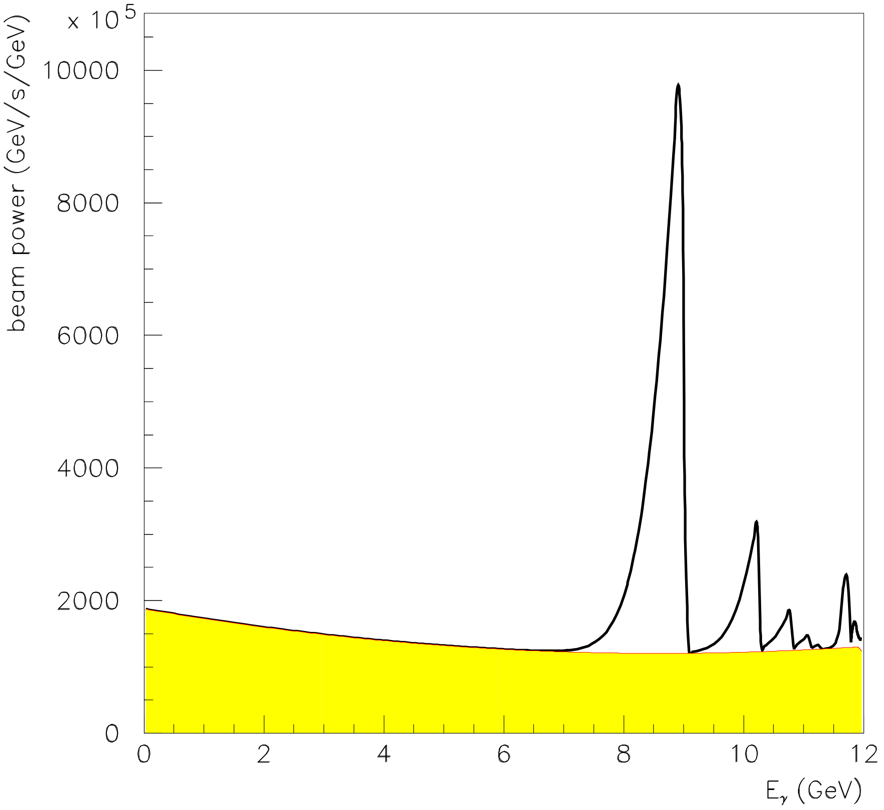

Figure 2.3: Photon power spectrum from an oriented diamond radiator. The y axis is dP/dE with power P expressed in GeV/s and E in GeV. The radiator thickness is 20 microns and the electron beam current is 1 μA. Shown is what emerges after the photon beam passes through a collimator 3.4 mm in diameter located 75 m downstream from the radiator.

power spectrum of the coherent bremsstrahlung beam after collimation. The sequence of secondary peaks above the primary correspond to integral multiples of the fundamental reciprocal lattice vector and so they are always present. By careful choice of orientation angles it is possible to suppress all other vectors and isolate just one primary peak in the energy band of interest, as shown in the figure. By a small rotation of the crystal, the position of the peak can be moved from one end of the spectrum to the other. Note that the coherent peaks appear as enhancements on top of the incoherent bremsstrahlung continuum.

Unlike those from the incoherent process, coherent bremsstrahlung photons have significant net linear polarization in the plane given by the beam direction and the crystal lattice vector. This polarization is enhanced by collimating the photon beam below its intrinsic angular spread, as discussed in the next section. The loss in flux from collimation can be recovered by increasing the electron beam current. As will be shown in the following section, even in the case of very thin crystals and severe collimation, quite modest electron beam currents are needed to produce the required photon flux.

The use of coherent bremsstrahlung improves the background conditions of the beam by enhancing the spectral intensity in the desired energy band relative to the incoherent continuum. For measurements that do not require polarization, a crystal radiator can be used without collimation to reduce the low-energy beam background for a given rate of tagged photons. Where polarization is required, coherent bremsstrahlung is indispensable.

Chapter 3

Photon source

A horizontal plan view of the photon beam line is shown in Fig. 3.1 with the major components labeled. The electron beam enters the figure from below ground at the left and is bent into the horizontal plane to enter the tagger building. There it passes through a pair of steering dipoles and passes through the bremsstrahlung radiator. Immediately downstream from from the radiator, the electron beam enters into the tagging spectrometer, where the primary beam is bent in the direction of the electron beam dump. The radiator crystal is thin enough that the average energy loss by the electrons in traversing the radiator is less than the intrinsic energy spread of the incident beam. Those electrons which lose a significant fraction of their initial energy inside the radiator predominantly do so by emitting a single bremsstrahlung photon. These degraded electrons are bent out of the primary beam inside the tagger magnet and exit the vacuum chamber through a thin window, passing through air for a short distance before they reach the tagging counters located near the focal plane of the spectrometer. The primary electron beam is contained inside vacuum all the way to the dump.

The photons that are produced in the radiator pass through a small hole bored in the return yoke of the tagger magnet in the forward direction. They then pass into an evacuated photon beam pipe and travel to the experimental hall. Just before entering Hall D, the photon beam passes through a small collimator which blocks a large fraction of the incident beam intensity, and selectively passes the coherent bremsstrahlung component. The primary collimator is housed in a separate enclosure from the experimental hall for shielding purposes. Debris from interactions along the inside surface of the collimator bore forms a halo around the photon beam that exits the primary collimator. The charged component of the halo is deflected away from the beam axis by a dipole "sweeping" magnet just downstream of the collimator and stopped

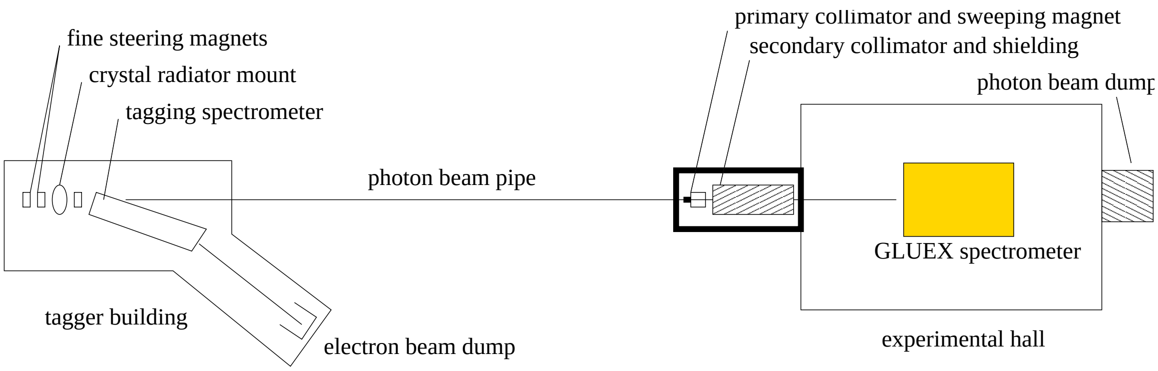

Figure 3.1: Schematic plan view of the photon beam line, shown in the horizontal plane as viewed from above. The objects in this figure are not drawn to scale.

in a thick wall of shielding material. Downstream of this there is a second collimator whose purpose is to block the halo of secondary photons generated by the first collimator. The secondary collimator is of a larger diameter than the primary and so sees a reduced rate of secondary interactions on the inner surface of the hole. What new showers are generated there are cleaned up by a second sweeping magnet. This two-stage collimation system is similar to the setup at the SLAC coherent bremsstrahlung beam line [2]. The clean collimated beam is then sampled in a pair spectrometer, which monitors the spectrum and flux of the beam just before it enters the experimental target.

After passing through of order 3% radiation lengths of liquid hydrogen in the GlueX target, the photon beam passes through the detector and into the photon beam dump at the back of the hall. Based upon a design upper limit of 60 kW (5 μA at 12 GeV) being delivered to the electron beam dump, the total power in the photon beam is not more than 1.5 W in the experimental hall and not more than 15 W in the collimator enclosure.

3.1 Essential features

The adjective ‘coherent’ in coherent bremsstrahlung does not indicate that the photons in the beam are in a coherent state, as is light from a laser. Rather it refers to the coherent effect of multiple atoms in a crystal lattice in absorbing the recoil momentum from a high energy electron when it radiates a bremsstrahlung photon. In X-ray spectroscopy one encounters the same thing in the Mössbauer effect. In that case, the chief physical consequence is the disappearance of the recoil Doppler shift from the photoabsorption/emission spectrum. In the case of coherent bremsstrahlung, the chief consequence is the enhancement of the cross section at those particular kinematics for which the recoil momentum matches one of the reciprocal lattice vectors of the crystal.

It is helpful to view the process of coherent bremsstrahlung as virtual Compton scattering. To the high energy electron, the atoms in the radiator appear as clouds of virtual photons. For a disordered radiator material, the virtual photon spectrum is given simply by the atomic form factor, averaged over the different species in the material. If the radiator is a single crystal, however, the atomic form factor gets multiplied by the form factor of the crystal, which for an infinite static crystal looks like a series of delta-functions located at the sites of the reciprocal lattice. In effect, the crystal provides a set of virtual laser beams, each one a standing wave tuned to a specific reciprocal lattice vector. In this view, the process of hard bremsstrahlung is seen to be the same as Compton back-scattering of laser light. For a more detailed discussion of the physics of coherent bremsstrahlung there are a number of good references [2, 3, 4, 5].

The use of Compton back-scattering of laser light as a photon source was earlier noted as ruled out by the limitations of high-power laser cavities to wavelengths above 100 nm. The characteristic wavelength of the virtual photons in a crystal is a few Angstroms, three orders of magnitude shorter than the limit for lasers. At keV energies, 180° Compton scattering results in essentially 100% of the electron beam momentum being transferred to the photon in the lab frame. However, the Compton cross section contains a factor of $1/(\vec{q} \cdot \vec{p})^2$ where $\vec{q}$ is the virtual photon momentum and $\vec{p}$ is that of the electron. This factor strongly favors incident photons with $\vec{q}$ nearly orthogonal to $\vec{p}$. With reciprocal lattice vectors pointing in almost every direction, only those nearly perpendicular to the beam contribute appreciably to the scattering rate. This fact applies equally to ordinary bremsstrahlung; in fact, to a first approximation the bremsstrahlung spectrum from a single crystal is the same as that from a disordered radiator. The reason is that replacing the sum over crystal momenta in the coherent bremsstrahlung cross section formula with a continuous integral recovers the cross section for ordinary bremsstrahlung from isolated atoms.

Furthermore, beyond a few unit cells from the origin in reciprocal lattice space the atomic form factor and kinematic factors become slowly varying on the scale of the lattice spacing, so that the higher-order terms in the sum become indistinguishable from the the high-q part of the corresponding integral. Besides that, the uncertainty principle requires that atoms localized at the sites in a crystal undergo fluctuations about their mean position. This has the effect of attenuating the discrete peaks in the crystal form factor at progressively higher-order crystal momenta, eventually washing them out and filling in the gaps between them, so that the sum deforms smoothly into the integral at high momentum transfer. Hence, the sum over crystal indices that yields the final photon spectrum can be separated into two parts: a discrete sum over a limited set of small crystal indices and an integral over the continuum of momentum transfer values beyond. The latter appears in the coherent bremsstrahlung beam as the ordinary continuum bremsstrahlung spectrum, while the former appears as a set of intensity peaks superimposed upon it. The $1/k$ continuum, referred to as the incoherent component, is invariant as the crystal is rotated, whereas the coherent peaks change in position and intensity, depending on crystal orientation.

A typical coherent bremsstrahlung spectrum is shown in Fig. 3.2. The distinction between incoherent and coherent components in the figure is artificial; it is there to distinguish the invariant part of the spectrum from the part that shifts as the crystal is rotated. The vertical scale in the figure gives the photon rate for the given beam current and crystal thickness. Note that the intensity of the incoherent background is less than what would be obtained with an amorphous carbon radiator of the same thickness, because a part of the momentum transfer integral in the Bethe-Heitler formula has been moved into the discrete sum and appears as the coherent part[1]. In the calculation used to produce Fig. 3.2, the leading 400 lattice sites were included in the discrete part of the calculation, but only two or three of them contribute with sufficient intensity to be identified with individual peaks visible in the spectrum.

3.2 Use of collimation

The presence of the large incoherent continuum in Fig. 3.2 presents a significant handicap to a photoproduction experiment. Not only do the continuum photons produce background in the detector, but they diminish the polarization of the beam. The entire beam polarization appears in the coherent component; the underlying incoherent flux only serves to dilute the polarization. However there is a difference between the angular distributions of the two components that allows them to be separated to some extent. The kinematics of bremsstrahlung confines most of the intensity of the photon beam to

---

[1] The typical figure of 12 cm for the radiation length of diamond is actually an average over all orientations of the crystal.

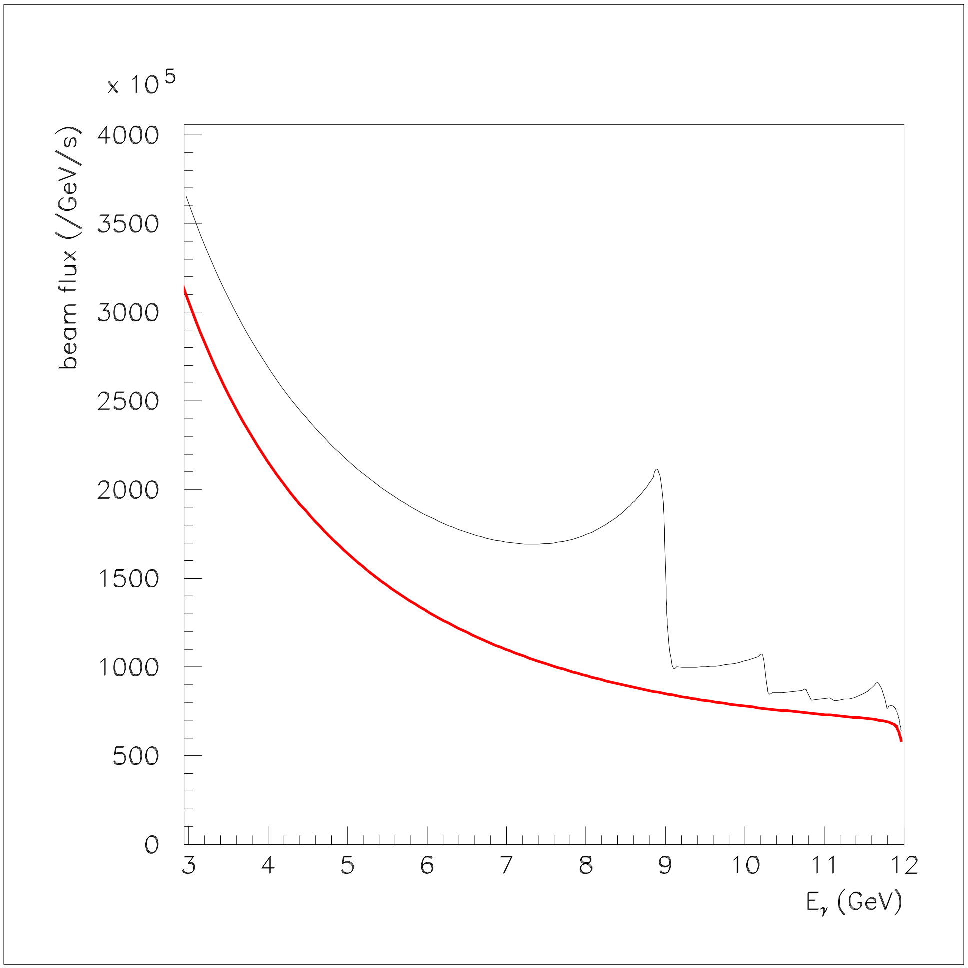

Figure 3.2: Uncollimated coherent bremsstrahlung spectrum, calculated for a diamond crystal radiator 20 microns thick and a 1 μA electron beam of 12 GeV energy. The sharpness of the edge at 9 GeV is a result of the excellent emittance of the 12 GeV electron beam.

forward angles within m/E radians of the incident electron direction[2]. This is true both for the incoherent and coherent components. The difference lies in the fact that a peak in the coherent component corresponding to a single reciprocal lattice vector has the two-body kinematics of Compton scattering, so there is a well-defined relation between the emission angle and the energy of the emitted photon in the lab: for a given reciprocal lattice vector, emission at 0° yields a maximum photon energy, and energy decreases with increasing angle. This accounts for the shape of the coherent peaks in Fig. 3.2, with the sharp right-hand edge of the peaks corresponding to 0° emission and the tail to lower energies corresponding to emission at higher angles.

The incoherent component, because it comes from a sum over momentum transfers at all angles, has essentially no correlation between photon energy and emission angle. This means that collimating away all photons beyond some angle $\theta_{max} < m/E$ uniformly attenuates the incoherent spectrum at all energies, whereas it preserves all of the coherent photons from the maximum energy for the given peak down to some cutoff. The kinematic relations for coherent bremsstrahlung are as follows,

$$\theta^2 + 1 = \left(\frac{1-x}{x}\right)\left(\frac{x_{max}}{1-x_{max}}\right) \tag{3.1}$$

$$x_{max} = \frac{2\vec{p}\cdot\vec{q}}{2\vec{p}\cdot\vec{q} - m_e^2} \tag{3.2}$$

where x is the photon energy in units of the incident electron energy and θ is the lab emission angle of the photon relative to the incident electron momentum axis, in units of m/E.

The effects of collimation are demonstrated in the calculated spectra shown in Fig. 3.3. First, note that the collimation angles are very small, which requires a long flight path of order 100 m in order that the collimator can be larger than the intrinsic beam spot size, otherwise the collimator is cutting in transverse coordinate instead of in angle. This distance is, in fact, a sensitive function of the electron beam emittance from the machine, and must be increased in proportion to the beam emittance if the effectiveness of collimation is held constant. This issue, along with the associated demands placed on beam alignment and position stability, are taken up in more detail in the following section on the electron beam line.

Second, note that the cut imposed on the coherent peak by collimation does not produce a perfectly sharp edge as would be expected from two-body

---

[2] In the lab frame this is a small angle, but in the rest frame of the electron-photon system it subtends all angles in the forward hemisphere.

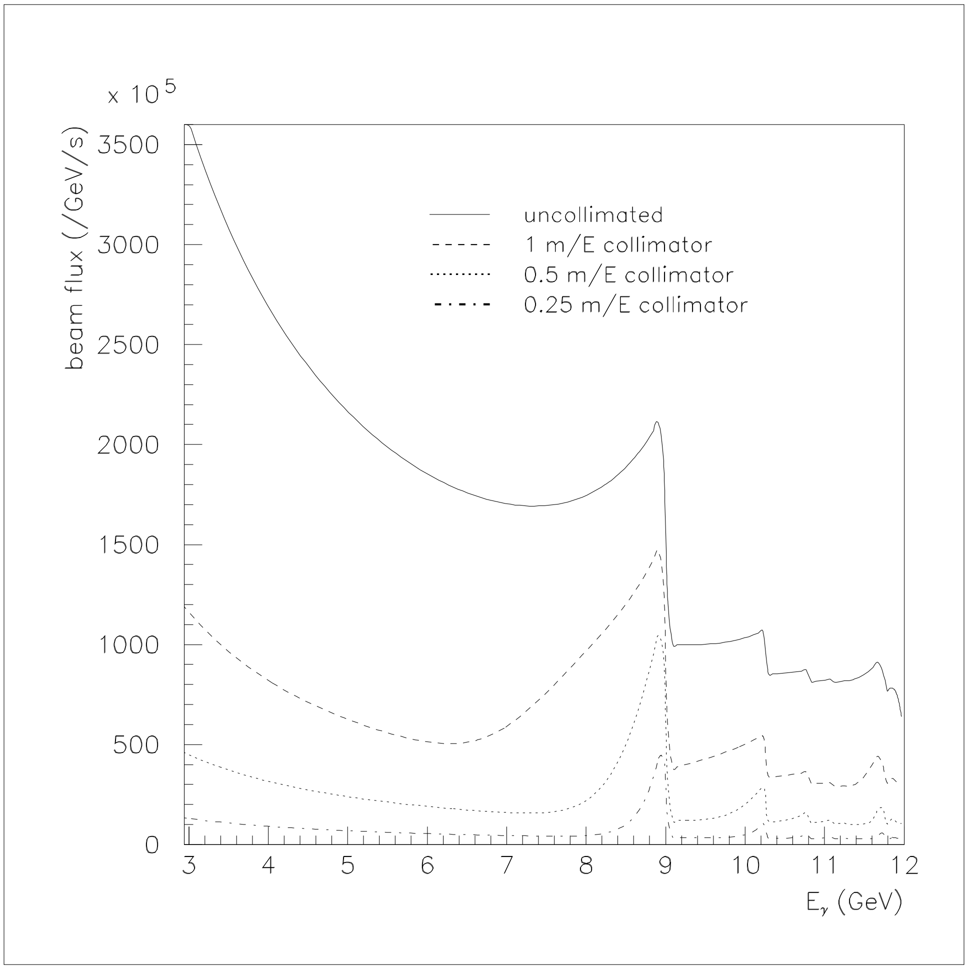

Figure 3.3: Coherent bremsstrahlung spectrum, calculated under the same conditions as in Fig. 3.2, with varying amounts of photon beam collimation. Curves shown from top to bottom are (1) the uncollimated spectrum, and collimated spectra with (2) a 1 m/E collimator, (3) a 0.5 m/E collimator, and (4) a 0.25 m/E collimator.

kinematics. This is because the collimator cuts on radius at some fixed distance, which translates into a cut on emission angle only in an approximate way. Multiple scattering by the electron in the radiator prior to emission, and beam spot size and divergence are the major contributors to the error involved in translating a collimator radius into a cut on emission angle. All of these effects have been incorporated into the analytical calculation of the yields from a collimated coherent bremsstrahlung source that has been used in optimizing the design of the source. Crystal imperfections, which amount to an intrinsic spread in the direction of the incoming virtual photon, are also taken into account in the model.

Third, note that the relatively weak collimation of 1 m/E reduces the incoherent background without significantly affecting the coherent flux near the maximum, thereby almost doubling the polarization of the beam at the peak relative to the uncollimated case. Further reducing the collimator diameter continues to narrow the peak and reduce the incoherent flux relative to the peak, albeit at some cost in peak intensity. The 0.5 m/E collimator has been chosen for this design because it provides for a maximum reduction in the incoherent flux while transmitting more than 90% of the coherent flux at the peak. This is implemented by placing a tungsten collimator with a circular aperture of diameter 3.4 mm at a distance 75 m downstream from the cyrstal.

Most of the photon beam energy coming from the crystal is absorbed by the collimator. To prevent the radiation produced at the collimator from producing background in the experimental, it is located in a separate enclosure just upstream of the experimental hall, and surrounded by a large amount of shielding. The peak in Fig. 3.3 for the 0.5 m/E collimator contains 4.8×10^7 photons/s in the primary coherent peak per μA of electron beam current. The GlueX experiment is designed to run at up to 10^8 photons/s in the coherent peak region 8.4-9.0 GeV. If the crystal is large enough to contain the entire electron beam spot at the radiator, this corresponds to 2.1 μA of electron beam current, safely below the design limit of 5 μA for the Hall D beam dump.

Fourth, note that the rate seen in the focal plane of the tagging spectrometer corresponds to the upper curve in Fig. 3.3, regardless of the collimation. This means that collimating the bremsstrahlung beam increases the rate in the tagger focal plane relative to what is seen at the detector. For full-intensity running at 10^8 photons/s on target in the coherent peak, Fig. 3.3 implies a rate of 250 MHz in the focal plane within a 600 MeV window around the peak. Combining this rate with the beam pulse spacing of 2 ns leads to an accidental tagging rate of about 50% and to a fraction of ambiguous tags of 40%. Even with ideal electronics, the per-second yield of single-tag events is close to saturation at this intensity. The detector and tagging spectrometer design are based upon a maximum rate of 10^8 photons/s on target and 400 MHz per GeV in the tagger.

The linear polarization of the photons in the coherent peak is shown in Fig. 3.4 as a function of the energy of the electron beam. This figure demonstrates why it is essential to have electrons of as high energy as possible, even though photon energies of no more than 9 GeV are required. The intensity of the coherent peak, not shown in the figure, has a similar dependence on the electron beam energy in this region.

Shown in Fig. 3.5 is the linear polarization of the photon beam *vs* photon energy for fixed electron beam energy. The dashed curves show how the maximum polarization in the primary peak varies as the peak energy is changed by rotating the crystal. The polarization in all cases is zero at the end-point. Without collimation it rises as $(E_0 - k)^2$, one power coming from the intensity of the coherent peak relative to the incoherent component, and the other from the intrinsic polarization of the coherent photons. Collimation allows one to essentially isolate the coherent component, so that the polarization available to the experiment rises from zero at the end-point in a linear fashion. The dashed curves in Fig. 3.5 demonstrate this point.

In order to obtain the full polarization enhancement from collimation, it is necessary to have a distance between the radiator and collimator on the order of 100 m. This distance scale is set by the requirement that the collimator aperture must be large compared to the virtual electron beam spot on the collimator but small compared to the actual photon spot size. The virtual electron beam spot is defined as the profile that the electron beam would have at the entrance to the collimator if it were allowed to propagate freely instead of being bent by the tagger dipole field into the beam dump.

The size of the virtual spot at the collimator is determined by the beam emittance combined with an upper limit of 20 μr on the angular spread of the electron beam at the radiator. The latter value was chosen to match the spread in the beam incidence angle to the mosaic spread of the crystal because it is the combination of the two that limits the definition of the coherent edge. Taking a conservative estimate of 10^{-8}m·r for the 12 GeV electron beam emittance[3] leads to a virtual spot size of 0.5 mm r.m.s. (1.2 mm f.w.h.m.). Note that this argument does not assume any scale for the radiator-collimator distance. The size of the real photon spot is given by one characteristic angle m/E which defines a circle on the collimator containing approximately 50% of the total photon intensity. The real spot size is proportional to the radiator-collimator

---

[3] Simulations of the 12 GeV accelerator design indicate that the horizontal emittance of the beam will be a factor 2 better than this, and a factor 4 bette in the vertical.

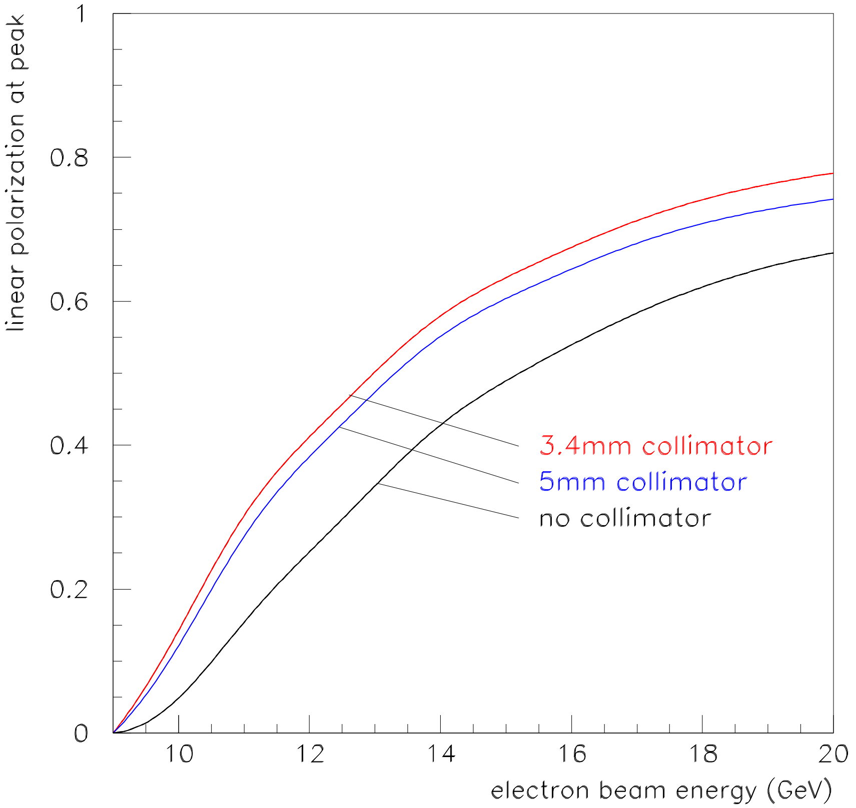

Figure 3.4: Linear polarization in the coherent bremsstrahlung peak as a function of electron beam energy keeping the energy of the coherent peak fixed at 9 MeV. The 3.4 mm [5 mm] collimator represents a cut at 0.5 [0.75] m/E.

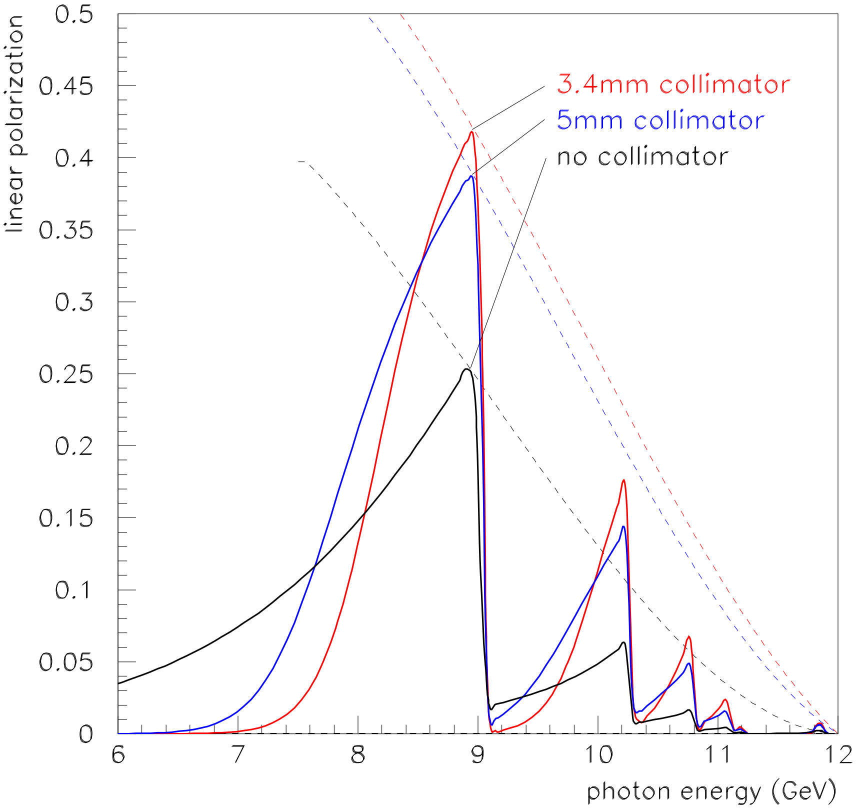

Figure 3.5: Linear polarization of the coherent bremsstrahlung beam for a fixed electron beam energy of 12 GeV. The dashed lines indicate the trajectory of the peak polarization as the peak energy is swept by rotating the crystal. The 3.4 mm [5 mm] collimator represents a cut at 0.5 [0.75] m/E.

distance. At a distance of 75 m the ratio of spot sizes is 6, sufficient to allow collimator apertures that satisfy both of the above inequalities.

Fig. 3.6 shows the peak polarization of the beam as a function of radiator-collimator distance for a coherent peak at 9 GeV. In this calculation the collimator diameter is held constant at 3.4 mm to make sure that the virtual beam spot of 1.2 mm f.w.h.m. is well-contained within the aperture, which is the main condition for effective collimation. At zero distance the collimator has no effect except to attenuate the beam, and so the uncollimated polarization from coherent bremsstrahlung is obtained. At 100 m separation distance the polarization enhancement from collimation has saturated. The design for Hall D calls for a radiator-collimator distance of 75 m.

3.3 Choice of radiator

The ideal radiator would be a layered structure with strong transverse fields that alternate between layers spaced about 50 nm apart, thus simulating the standing wave in a cavity driven by a 15 eV laser. While it is possible to construct ordered materials with unit cells as large as this, the self-shielding of atoms means that beyond the atomic length scale the residual fields are comparatively weak. Hence heterogeneous structures are not viable for use as a coherent radiator. Since the strong fields inside a solid are revealed at the atomic scale, the first requirement for a good radiator is that the unit cell be compact and closely packed. The best radiators are those with the smallest unit cells because these provide the best match between the atomic and the crystal form factors. This match is best for the light elements, and essentially prohibits the effectiveness of materials containing substantial amounts of any elements heavier than carbon. An extensive survey of possible radiator materials is presented in Ref. [3]. In Table 3.1 is shown the figure of merit that those authors report for favored crystalline materials. The figure of merit is the product of the atomic times the crystal form factor evaluated at the leading peak, normalized to the value for diamond.

Table 3.1 shows that the list of viable materials for a crystal radiator is relatively short. Silicon would be an excellent choice from the point of view of price and fabrication, but unfortunately it is far inferior in terms of performance. The material shown with the highest figure of merit is the binary crystal Be_2C. In general, multi-element crystals are more sensitive to radiation damage than single-element crystals because annealing of dislocations is significantly less efficient when more than one atomic species is involved. This leaves diamond and beryllium as the two alternatives.

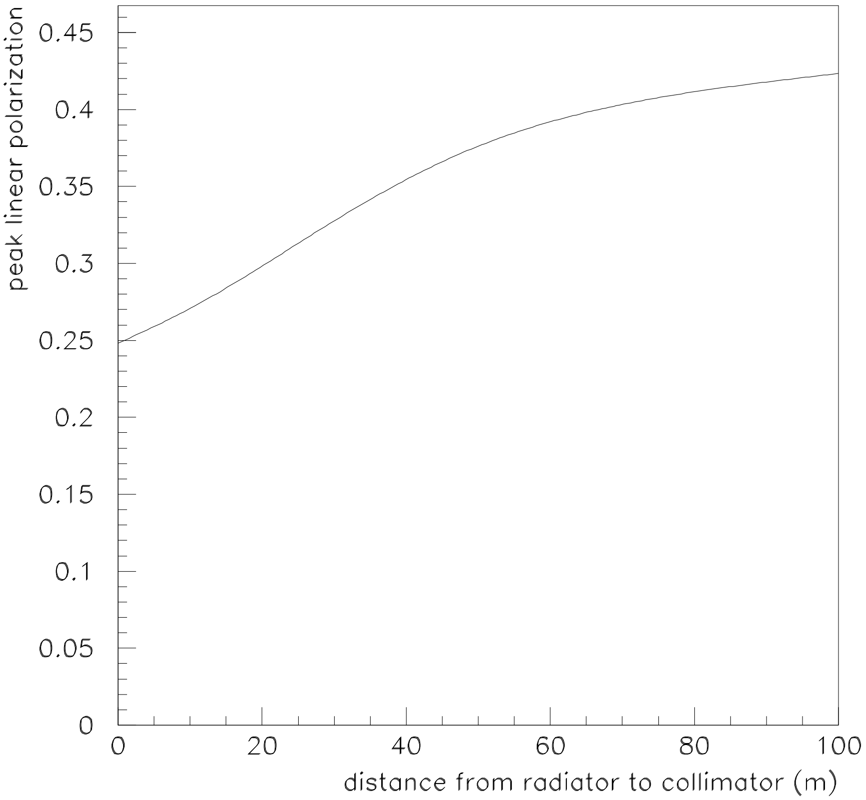

Figure 3.6: Maximum polarization *vs* radiator-collimator distance for a coherent peak at 9 GeV. The collimator diameter is held fixed in this calculation to keep a constant ratio between the sizes of the virtual electron spot and the collimator.

crystal	best reciprocal vector	P/P_{diamond}
diamond	2,-2,0	1.00
beryllium	0,0,2	0.86
boron	2,0,8	0.38
silicon	2,-2,0	0.19
Be_2C	2,2,0	1.10

Table 3.1: Figure of merit for various materials that might be used as a coherent bremsstrahlung radiator. This table is reproduced from Table 2 in Ref. [3].

Both diamond and beryllium have unusually high Debye temperatures. A high Debye temperature is important for a bremsstrahlung radiator material for three reasons. First, the cross section for coherent bremsstrahlung from a discrete crystal momentum vector $\vec{q}$ contains a factor $e^{-q^2/4M\theta_D}$ which reflects the fact that position fluctuations of atoms in the lattice diminish the coherent effect. This factor is near unity for the low-order crystal momenta provided that the Debye temperature θ_D is sufficiently large. Second, the Debye temperature is, roughly speaking, a measure of the stability of the crystal structure and hence its capacity to survive significant doses of radiation. Third, the radiator material will inevitably be heated by the beam, and will normally operate in vacuum well above the ambient temperature. A high Debye temperature means that there is a large range of temperatures over which the material may operate without degraded performance as a crystal radiator. The Debye temperature of diamond is 2200°K, while that of beryllium is 1400°K.

Considerable experience exists with both diamond and beryllium single crystals for use as monochromators within in the X-ray diffraction community. Single crystals of both can be produced with diameters larger than 10 mm, which is sufficiently large for use as a coherent bremsstrahlung radiator. However there are a number of features, besides the performance figure showin in Table 3.1, that make diamond a clear winner in this application. First of all, diamond has a thermal conductivity that is a factor 10 larger than that of beryllium. Although both are excellent thermal conductors, the difference makes a difference when the crystal is made very thin, while keeping the heat load constant, which is the optimization scenario for a coherent bremsstrahlung source. As shown in a following section, the thermal load on the radiator in the Hall D source is enough to heat the crystal to several hundred degrees at full operating intensity. Therefore a factor 10 higher thermal conductivity is a significant advantage for diamond. Combined with this, the thermal expansion coefficient for beryllium is about a factor 10 higher than that of diamond, which means that it will be much more subject to thermal stress and distortion in the beam than will diamond. More importantly, published rocking curves for beryllium single crystals have widths greater than 300 μr f.w.h.m., as compared with less than 20 μr f.w.h.m. for the best large-area diamonds [6]. For these reasons, diamond has been adopted as the unique choice for the radiator material in the Hall D coherent bremsstrahlung source.

Most of the experience to date with coherent bremsstrahlung has been with diamond radiators. Extensive expertise with large diamond crystals, such as would be required for the production of coherent bremsstrahlung radiators, already exists within the gem industry [7, 8]. Although the details of the crystal growth process are typically treated in the highly competitive diamond business as sensitive corporate information, researchers both in Europe and Japan have been able to obtain large-area crystals from the firms Element Six and Sumitomo Electric Industries and demonstrate that they have X-ray rocking curves that are very close to the theoretical ideal for a perfect crystal [9, 10]. Within the GlueX collaboration, the University of Glasgow group has been able to obtain a significant number of high-quality crystals from Element Six, cut along the desired crystal direction and polished down to a desired thickness. The techniques used for assessing the quality of the diamonds are discussed in the next section.

In general terms, diamonds are classified as type I or type II, where type II have been subjected to greater stresses during their formation than type I. Commonly, type II exhibit substantial plastic deformation. Diamonds are also classified according to the form in which nitrogen atoms are present in the crystal lattice. In type *a* the nitrogen is aggregated into clusters of atoms, whereas in type *b* the nitrogen is almost uniformly distributed throughout the crystal. For coherent bremsstrahlung radiators, type Ib diamonds are the most suitable. Unfortunately, type Ib natural diamonds are very rare. The only known way to obtain large high-quality Ib diamonds is through the process of synthetic crystal growth. The primary impurity in these synthetics is nitrogen, which is artificially introduced as a growth catalyst. At present type Ib diamond mono-crystals can be obtained with nitrogen concentrations as low as 100 ppm.

Synthetic diamonds are made using either vapor deposition (CVD) or high pressure high temperature (HPHT) techniques. CVD diamonds have an extensive mosaic and are unsuitable for coherent bremsstrahlung. Synthetics from the HPHT process are not uniform in their crystal quality, but it is not rare to find large regions of a crystal that approach the theoretical limit in the X-ray rocking curve width. Among the high-quality crystals obtained by the Glasgow group from Element Six, one of them was polished down to a thickness less than 18 microns, demonstrating the feasibility of producing the 20 micron diamonds needed for GlueX.

3.4 Crystal quality

In the calculation of the coherent bremsstrahlung spectrum it is necessary to take into account the fact that even the very best crystals have some dislocations and other defects. Besides locally disrupting the regularity of the crystal, these defects impose stresses which produce small ripples in the crystal planes. If these ripples were amplified, the surface of a crystal would appear like a mosaic of planar regions whose local normal unit vectors are slightly misaligned with one another. The angular scale of the deviations between the local normals across the face of a single crystal plane is termed the *mosaic spread* of the crystal. Because crystal lattice distortions affect all of the planes in that region of the crystal, mosaic spread tends to have the same scale for all sets of planes in a given region, and is characterized by a single parameter. In coherent bremsstrahlung, the mosaic spread contributes in the same way as electron beam divergence to the blurring of the exact energy-angle relation for coherent photons.

Besides dislocations, there are other kinds of crystal defects. The presence of foreign atomic species during the crystal growth process can result in the substitution of impurities at some lattice sites, or the formation of voids where impurities tend to collect in clusters of several atoms. In the growth of diamond crystals under conditions of high pressure and temperature, the growth rate is greatly enhanced by the presence of a small amount of nitrogen. Thus it is normal that small amounts of nitrogen impurities should exist even in the best natural stones, as well as in the synthetics created by the HPHT process.

The ideal conditions for growth of a perfect synthetic crystal require preexisting mono-crystalline diamond with clean planar facets cleaved along the major crystal planes, upon which new layers of carbon are deposited in succession. If conditions are right, the registry of the atoms with the original crystal is preserved over millions of deposited layers, starting from the original seed. In principle, the new planes of the regular lattice should continue to match up perfectly at the boundaries between the different growth surfaces that originated on the facets of the seed, but in practice the strains from the accummulation of small imperfections that occur during the growth process

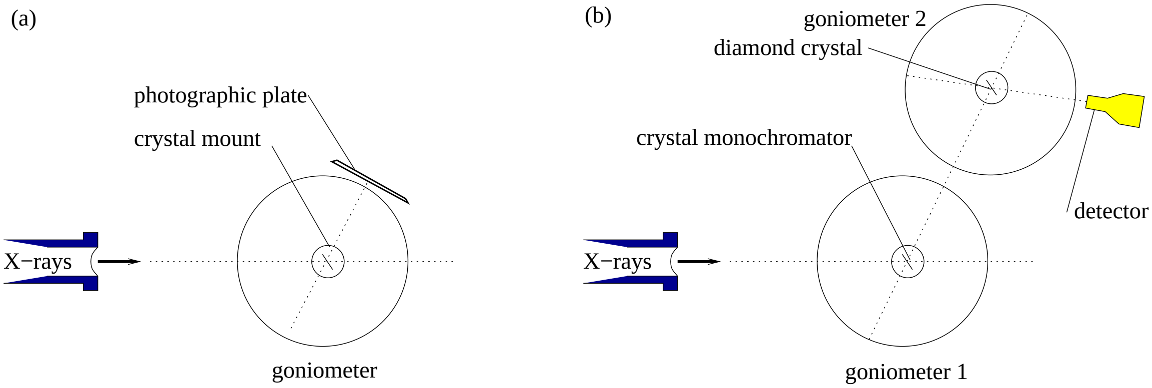

Figure 3.7: Experimental setup for assessment of diamond crystals at the Daresbury Synchrotron Light Source beam line, configured for topograph measurements (a), and rocking curves (b).

tend to build up there, forming recognizable patterns of concentrated defects known as *growth boundaries*. If the stresses grow too large then new strain regions develop, leading to a more pronounced mosaic pattern in the subsequent layers.

Unfortunately the growth process has proved difficult to control in a reproducible fashion. As a result, out of several dozen stones produced, typically only one or two are of sufficient quality for use as a coherent bremsstrahlung radiator for. The selection process described below was formerly developed by the Glasgow group to supply crystals for the coherent bremsstrahlung source at Mainz, Germany and subsequently for the Hall B source at Jefferson Lab. The requirements for HALL D are very similar to those of Mainz and Hall B, except that the electron beam current will be higher by about an order of magnitude and the crystals will be thinner.

To produce a coherent bremsstrahlung radiator from a synthetic diamond, the ingot from the synthetic process was sliced into sections along the (1,0,0) axis using a diamond saw. This cut was made by the vendor at the laboratory where they are produced. Sample slices from different regions along the axis were provided to the Glasgow group for assessment. The samples were first examined under a microscope with polarized light. Crystals which exhibit large plastic deformation were discovered and eliminated at this stage. Those which appeared clear and featureless under polarized light where then taken to a synchrotron light source and examined using X-ray diffraction. Two types of X-ray measurements were performed, topographs and rocking curves.

1. Topographs
   A topograph is a real-space image of a diamond formed from X-rays that Bragg-scatter from a particular set of planes in the crystal, as shown in Fig. 3.7a. Using the highly-parallel X-ray beam from the Daresbury Synchrotron Light Source (SRS) and setting the detector at twice the Bragg angle for a known set of planes for diamond, X-rays of the appropriate wavelength to satisfy the Bragg condition are scattered at a precise angle θ into the detector. If the crystal is a single crystal then the X-ray image formed on the plane of the detector is a real-space image of the crystal, called a *projection topograph.* If the vertical slits defining the X-ray beam are narrowed forming the incident beam into a thin ribbon a few μm wide, then the image at the detector reveals a slice though the crystal, called a *section topograph.* Projection topographs reveal any large-scale imperfections in the crystal. Section topographs can be used to examine the depth profile of imperfections. Topographs sample the whole volume of the crystal. Hence, by measuring projection and section topographs, a 3-dimensional picture of the diamond can be obtained. It is also possible to differentiate between screw and edge dislocations. The topograph image reveals dislocations, growth boundaries and any feature which suppresses or enhances Bragg scattering at the selected angle. In principle, topographs taken at different angles provide independent views of the crystal structure. In in practice, however, the imperfections that are revealed with one set of planes appear in a similar fashion when viewed from other orientations.

2. Rocking curves
   A rocking curve is a plot of Bragg-scattering intensity *vs* angle between the incident X-ray beam and the normal to the crystal planes. A diagram of the setup used at the Daresbury SRS is shown in Fig. 3.7b. First the broad-band X-ray beam from the SRS is monochromated by scattering at a known fixed angle from a reference crystal, in this case silicon. This beam is then directed at the diamond crystal under study, from which it scatters a second time and is detected. The scattering is appreciable only when the diamond is at just the right angle with respect to the incident beam such that the Bragg condition is satisfied at both crystals. The variation in the scattering intensity with angle as the diamond wafer is rotated through the scattering peak is called the *rocking curve* for that diamond. A perfect crystal exhibits a rocking curve consisting of a single peak whose width is called the *natural width* and depends on the material and the crystal plane. The natural width of the (2,2,0) planes in diamond

> is about 5 μr. Instead of a single peak, for actual crystals one typically sees a number of peaks spread out over a region in angle known as the rocking curve width. Rocking curves widths, for a selected set of crystal planes, measure quantitatively how defects distort the crystal lattice. By adjusting the slits it was possible to examine the rocking curve in a local region of the crystal or to measure the entire crystal at once. From the rocking curves it is straight forward to determine how close to ideal the lattice structure of the diamond is for coherent bremsstrahlung.

Figs. 3.8-3.9 show some of the results that were obtained at the SRS in January, 2002. At the left of the figures is shown a projection topograph taken with the (0,4,0) planes. At the right is shown the corresponding rocking curve taken in combination with a silicon crystal set to reflect from the (3,3,3) planes at a wavelength of 1Å. The two diamond wafers had been cut from the same original type Ib stone, with Fig. 3.8 coming from the end close to the seed, and Fig. 3.9 coming from near the middle of the ingot. The topographs are negatives, meaning that the image is dark in regions where the X-ray intensity was largest.

The first thing to notice from the topographs is that both wafers are monocrystalline; there are no regions within the boundaries of the crystal where X-rays do not scatter. Even so, there are important differences between the two samples. The growth boundaries (the picture-frame pattern) which are visible in Fig. 3.8 spread out and become less pronounced in slice 2 which was taken further from the seed. It is interesting that the strain pattern appears mostly as dark regions rather than light, which indicates stronger scattering in the defects than in the ordered regions. This is expected because the crystal is thick enough to scatter essentially 100% of the beam photons that fall within the peak region in the rocking curve, so the wider is the rocking curve, the wider the energy bite of the broad-band beam that is scattered. It should be recalled that both crystals appeared clear and featureless under polarized light at visible wavelengths. Only X-rays can reveal the significant defect structure of these crystals.

The specification for a diamond radiator for use as a coherent bremsstrahlung radiator in HALL D is that the rocking curve width be no greater than 20 μr r.m.s. The conclusion drawn from the rocking curve measurements is that slice 2 is a good candidate for use in the GLUEX experiment, and that slice 3 is not. Having confirmed the quality of slice 2, it would have been possible to request that the manufacturer cut several wafers from the same region of the original stone, and expect that the quality of the new slices will be similar. This was not done because at that time the demand for new crystals was

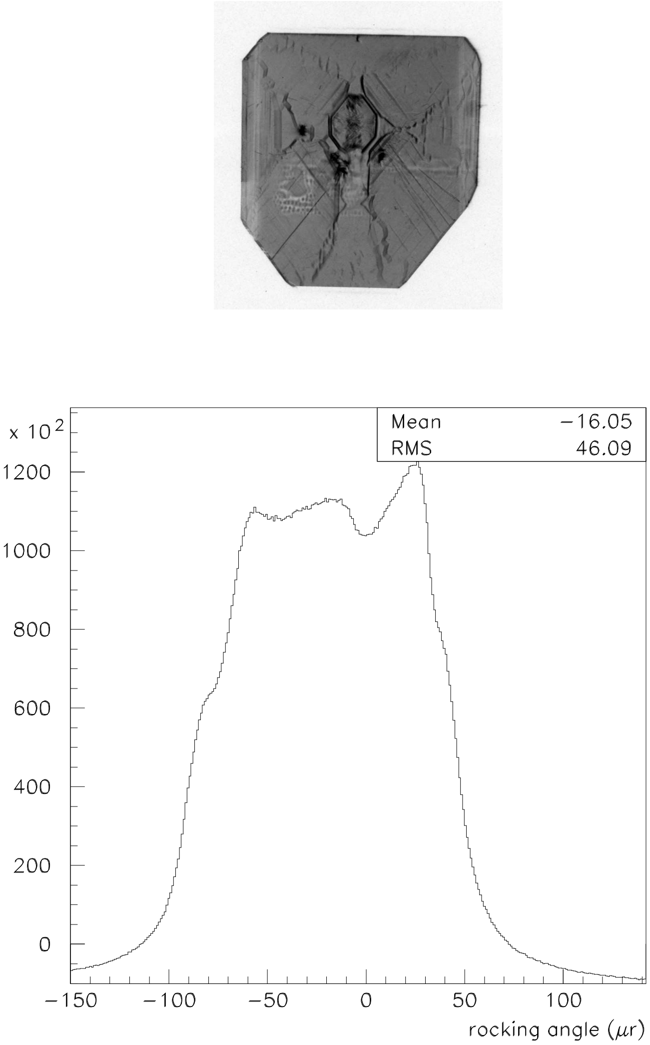

Figure 3.8: Experimental data collected using highly-parallel X-rays from the Daresbury SRS light source for stone 1482A slice 3 (close to the seed). At the top is shown a projection topograph of the wafer taken using the broad-band X-ray beam and a Polaroid film placed at the angle for reflection from the (0,4,0) planes. The image is a magnified by a factor of 5. The graph shows the rocking curve for the same set of planes, taken using a NaI counter and 1Å X-rays monochromated by a silicon crystal.

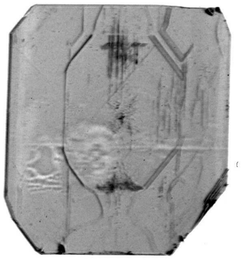

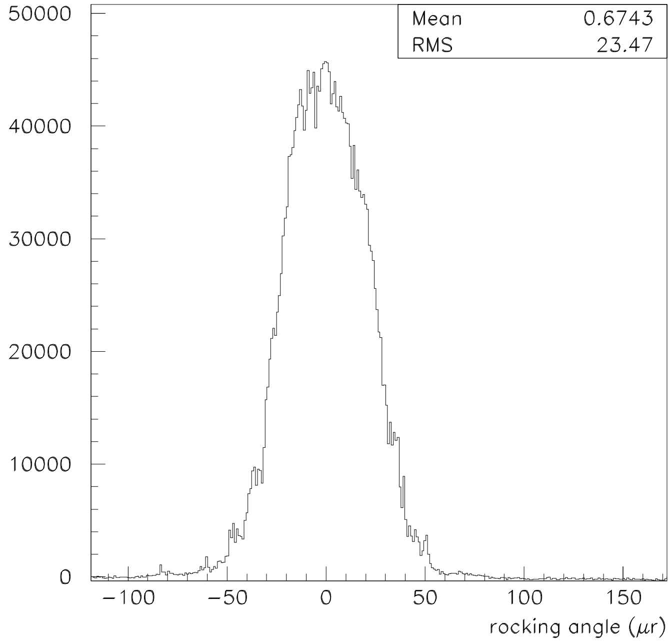

Figure 3.9: Experimental data collected using highly-parallel X-rays from the Daresbury SRS light source for stone 1482A slice 2 (further from the seed). At the top is shown a projection topograph of the wafer taken using the broad-band X-ray beam and a Polaroid film placed at the angle for reflection from the (0,4,0) planes. The image is magnified by a factor of 5. The graph shows the the rocking curve for the same set of planes, taken using a NaI counter and 1Å X-rays monochromated by a silicon crystal.

one or two every few years. In the case of HALL D it will be important to take advantage of such efficiencies in order to obtain a steady supply of new radiators to replace those damaged by radiation.

3.5 Crystal thickness

The range of permissible thicknesses for a crystal radiator is bounded both from above and below. It is bounded from above by multiple scattering of the electron beam as it passes through the radiator, which causes the divergence of the incident beam to grow, thereby enlarging the photon beam spot on the collimator face and degrading the degree to which collimation discriminates against the incoherent component in favor of the coherent part. It is bounded from below by the rate of radiation damage that increases for thinner crystals, as the electron beam current is increased to maintain the desired beam intensity.

There is a second and more fundamental lower bound imposed by the fact that the crystal must have some minimum thickness in order to achieve the full coherent gain. The calculation of the coherent bremsstrahlung cross section begins with the assumption of an infinite crystal, but practically this means only that the crystal is large compared to some characteristic scale. It is important to identify what the characteristic scale is in this problem in order to know how thin one can make the crystal without hurting performance. In the analogous case of the Mössbauer effect, one can estimate the number of atoms participating in the collective absorption by looking at the emission time of the photon (lifetime of the radiating transition) and asking how many nuclei lie within the envelope of the photon wave packet. In the coherent bremsstrahlung process, the lifetime of the radiating system is given in the lab system by the uncertainty principle and by how far the electron energy deviates from its on-shell value between absorbing the virtual photon and emitting the real one. The latter quantity is almost exactly given by q_z , the initial-state virtual photon momentum component along the incident electron axis. This means that the electron travels an average distance $\lambda = \hbar c/q_z$ during the interaction. For a given coherent peak at normalized energy x in the photon spectrum, the coherence length is given by

$$\lambda = \frac{2\hbar E(1-x)}{xm^2c} \tag{3.3}$$

From this simple argument one sees that the coherent gain goes linearly to zero at the end-point, a result that is borne out by the full QED calculation. One also sees that the lower limit on crystal thickness imposed by the coherence length depends upon both the electron beam energy and the photon energy. For 12 GeV electron beam energy and a 9 GeV coherent photon the coherence length is 6 nm, or about 17 unit cells for diamond. This shows that the coherence length does not impose a practical limit on how thin the radiator should be for GlueX.

The effects of multiple scattering are best presented by showing the calculated spectra for various radiator thicknesses. In Fig. 3.10 is shown the photon spectrum for diamond radiators of thickness 10, 20, 50, and 100 microns. The electron beam current in each case is rescaled to keep the rates in the tagger constant. The loss in normalized intensity with the thicker radiator and as the broadening of the left edge of the peak are due to the smearing out of the photon beam spot on the collimator face due to multiple scattering of the electron beam in the crystal prior to radiation. The plot shows that improvements in the coherent / incoherent flux ratio with decreasing radiator thickness saturate around 20 microns. The design for the GlueX photon source specifies diamond radiators of thickness 20 microns.

3.6 Crystal mount

It has already been shown that in order to achieve appreciable coherent gain the crystal must be oriented so that the coherent peaks appear well below the end point. Equation 3.2 then implies that the orientation must be such that the crystal momentum dotted with the beam momentum be of order m^2. For $p = 12GeV$ and $q \approx 10keV$, this amounts to requiring that p and q be mutually perpendicular to within about a degree, and within one degree of variation the coherent peak sweeps out nearly the full range in x from 0 to 1.

Hence, to have a stable photon beam with the coherent peak positioned at the right energy, the angle between the incident electron beam and the crystal radiator must be adjustable in steps of a few μr and remain stable at this level. Since the angle of the incident beam is fixed by the beamline optics and the position of the photon collimator, incidence angle adjustments are made by changing the orientation of the crystal. This is achieved with a precision goniometer (shown schematically in Fig. 3.11). A goniometer with three rotation axes and two translation axes gives the necessary control over both where the beam spot is located on the crystal and what its angle is with respect to the beam direction. Rotation about the azimuthal axis ϕ sets the orientation of the polarization plane. Rotations about the θ_v, θ_h axes select the energy of the coherent peak and provide an additional handle for eliminating

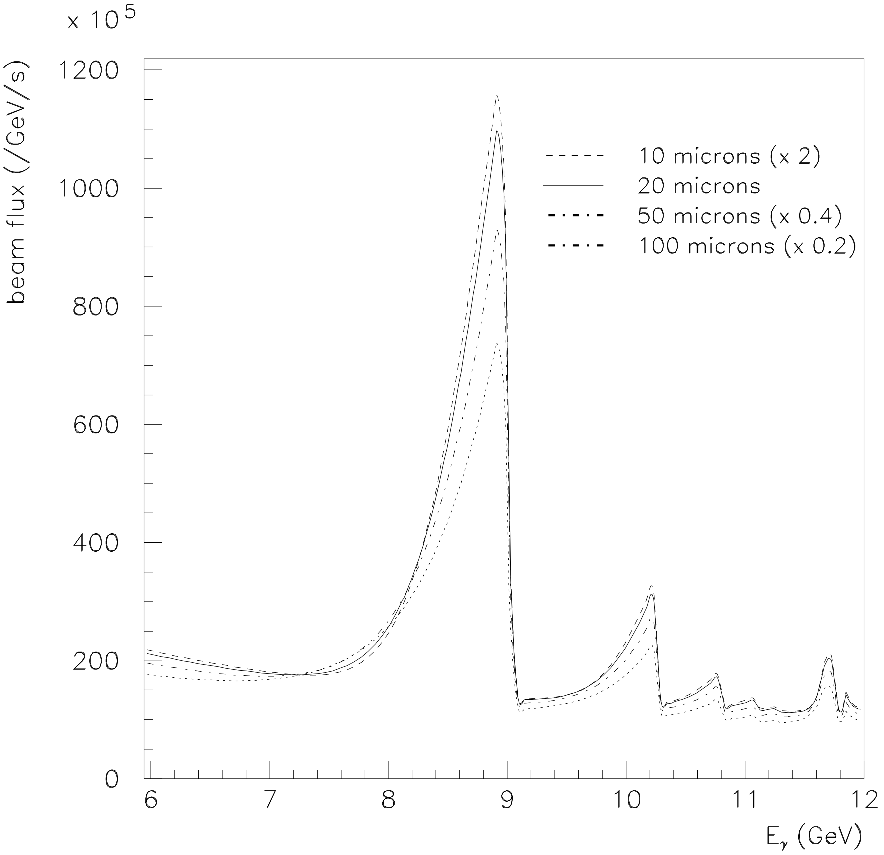

Figure 3.10: Collimated coherent bremsstrahlung spectrum from a 12 GeV electron beam using diamond radiators of different thicknesses. The beam currents have been renormalized to keep the rates in the tagger constant. The calculation assumes a 3.4 mm collimator located 75 m from the radiator, and standard values for beam emittance and crystal mosaic spread.

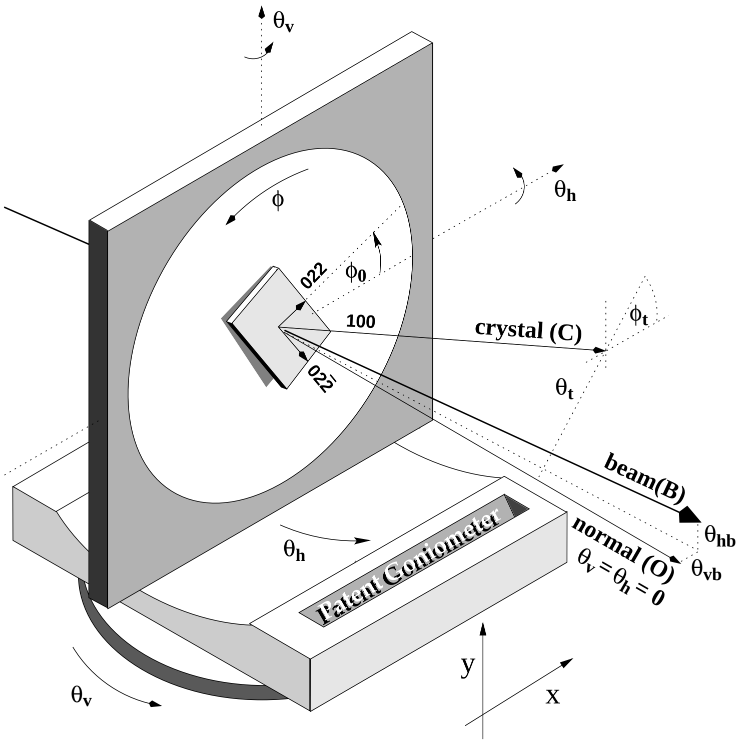

Figure 3.11: Schematic illustration of crystal mounted in goniometer

extra peaks in the spectrum from unwanted lattice vectors. The translational axes select the position of the beam spot on the crystal and allow for moving the crystal into and out of the beam. Estimates of the approximate range and step size for each of the axes are given in Table 3.2.

It is foreseen that the crystal goniometer will hold a target ladder in which several targets are mounted, which can be interchanged under remote control. The minimum requirement for the ladder is a diamond crystal, an amorphous radiator, a blank position, and a fluorescent screen to show the position and shape of the beam spot. A second diamond would also be useful, in case the first one is damaged in some way. A goniometer with the required precision can be obtained commercially. Remote control of all stages of the goniometer is part of the slow controls plan for the GlueX experiment.

Axis	**Motion**	**Range**	**Step size**
x	horizontal translation	-100 mm – +100 mm	0.1 mm
y	vertical translation	-20 mm – + 20 mm	0.1 mm
θ_v	vertical rotation	-100mr – +100mr	5μr
θ_h	horizontal rotation	-100mr – +100mr	5μr
ϕ	azimuthal rotation	-30° – +120°	0.01°

Table 3.2: Requirements for range and step size of goniometer axes. Commercially available goniometers yield up to five times higher accuracies.

3.7 Crystal alignment and monitoring

As can be seen in Fig. 3.11 the goniometer setting θ_v,θ_h defines the direction of the vector normal to its inner plate (O). Ideally at its zero setting $\theta_v = \theta_h = 0$ this normal vector would coincide with the electron beam direction (B), but in practice there are small offsets θ_{vb}, θ_{hb} which may vary slightly with the tune of the electron beam. There are also two other corresponding offsets that specify the direction of the (1,0,0) axis of the crystal with respect to the inner plate normal vector. These arise both from imperfections in the way that the crystal is mounted to its holder, and from imperfections in the way that the crystal was originally cut. These corrections can be parameterized in terms of the tilt θ_t of the (1,0,0) crystal axis from the O direction, and also its azimuthal vector ϕ_t. A third offset angle ϕ_0 is also needed to specify the azimuthal plane containing the (0,2,2) axis direction in the coordinate system of the goniometer mount. Once the goniometer angles θ_v and θ_h have been adjusted to align the (1,0,0) crystal axis with the beam direction B, then the (0,2,2) direction is normal to the beam and the goniometer azimuthal setting $\phi - \phi_0$ determines the plane of polarization of the beam relative to the horizontal.

Each time a new crystal is installed, the offsets θ_{v0}, θ_{h0} and ϕ_0 must be determined empirically by systematically rotating the crystal while monitoring the positions of the coherent peak in the coherent bremsstrahlung spectrum seen in the rates measured by the tagger focal plane counters. A collimated photon spectrum is not required for the alignment procedure, but it is essential to sample low enough in the photon energy spectrum to see the peaks at low x. For this reason, the tagger focal plane is instrumented with a broad-band counter array that covers the full energy spectrum from 3 GeV up to 11.7 GeV. Counting the singles rates in the broad-band array with scalers and plotting them in a two-dimensional histogram versus the wobble angle of the crystal provides the fast feedback that allows the alignment procedure to be completed in a relatively short period of time. The alignment procedure is detailed in [11].

During normal running after the alignment has been carried out, the broadband tagging counters provide essential online diagnostics to monitor drifts in angles caused by changes in the beam tune, thermal effects in the crystal mount, and radiation damage. If necessary a feedback system could be implemented via the slow control system, where any drift in the position of the coherent peak could be corrected by periodically adjusting the goniometer angles within predefined limits.

3.8 Crystal lifetime

There are no published results that give precise information about the kinds and densities of crystal defects in diamond as a function of dose. The best estimates for crystal lifetime in a coherent bremsstrahlung source are found in an unpublished SLAC report [12] which states that "serious degradation" of the coherent bremsstrahlung spectrum was observed after 2-5 Coulombs of electrons had passed through the crystal. The SLAC beam energy was 19.7 GeV, which should not be much different from 12 GeV for these purposes. The SLAC beam spot was large enough to fill the entire crystal, of approximate area 1 cm^2, although this is not to say that the beam intensity was uniform over that area. From these results can be derived a useful upper bound of about 0.25 Coulomb/mm^2 on the integrated current that can pass through a diamond before it must be replaced. In the same report claims are made that it was possible to recover acceptable performance from a damaged diamond by annealing it in a high-temperature oven. The annealing procedure was found to work over several use cycles, before the accumulated damage was so severe that the diamond could no longer be used.

The best quantitative information on crystal degradation from radiation damage comes from X-ray studies performed by the Glasgow group of a diamond which had been used in the MAMI coherent bremsstrahlung source at Mainz for several years[9]. The electron beam on the Mainz crystal had a full width of about 100 microns. It was estimated that 5-10 Coulombs of electrons had passed through the diamond during its use in the source. There was a small greenish black spot visible where the beam had passed through the diamond. This small beam spot means that the exposed region of this crystal had seen three orders of magnitude more integrated charge than allowed by the upper limit estimated above based on the experience reported by the SLAC group. Indeed, X-ray rocking curve measurements with a very small X-ray beam showed that in the center of the beam spot the rocking curve was split into many peaks, and that the full width was several mr. However 2 mm away from the damage center, a single narrow peak was seen in the rocking curve, with essentially the same width as had been observed for the pristine crystal. This confirms that the lifetime of a crystal can be extended by occasionally moving the beam spot on the face of the crystal.

The area of the beam spot on the damaged MAMI radiator is two orders of magnitude smaller than what is being planned for HALL D. A larger spot means a longer crystal lifetime before radiation damage substantially degrades the crystal properties. Appropriately scaled, the exposure of the Mainz crystal in the center of the beam spot corresponds to more than 10 years of running in HALL D at full intensity without a spot move. Plans for the HALL D source are to keep the local dose three orders of magnitude less than this. Based on the estimated upper limit stated above, the HALL D source can run at a full intensity of 2 μA for 100 hours before it is necessary to move the spot on the crystal. If it had no bad zones, a square crystal of area 5×5 mm^2 would accommodate 5 spot moves before the crystal would need to be replaced.

Measurements of crystal radiation damage rates will be made during the first two years of GLUEX running. During those two years, the source will operate at 10% of design intensity, permitting a single crystal to last for an entire year of running. These same estimates suggest that as many as 5 diamonds per year will be required to run the HALL D source at full intensity. It may or may not turn out to be economically advantageous to try annealing damaged crystals, depending on the availability and cost of new diamonds at that time.

Another issue related to crystal degradation is that of heat dissipation for very thin crystals. The heat from the ionization energy loss of the beam as it passes through the crystal must be dissipated either via conduction through the crystal mount or via thermal radiation. Although the ionization energy loss is small compared to that from bremsstrahlung, it is not entirely negligible at beam currents planned for HALL D. It can be calculated using the restricted energy loss formula, which yields 21 mW for a 20 micron crystal at a current of 2.1 μA. This is not much power, but the crystal is very thin. Diamond has a very high melting point; at low pressures it sublimates at about 4027°C. However it begins to transform into graphite above 707°C, at a rate that increase with temperature. It is essential that the crystal at the center of the beam spot stay well below this limit.

The diffusion equation including a heating term and one for radiative cool-

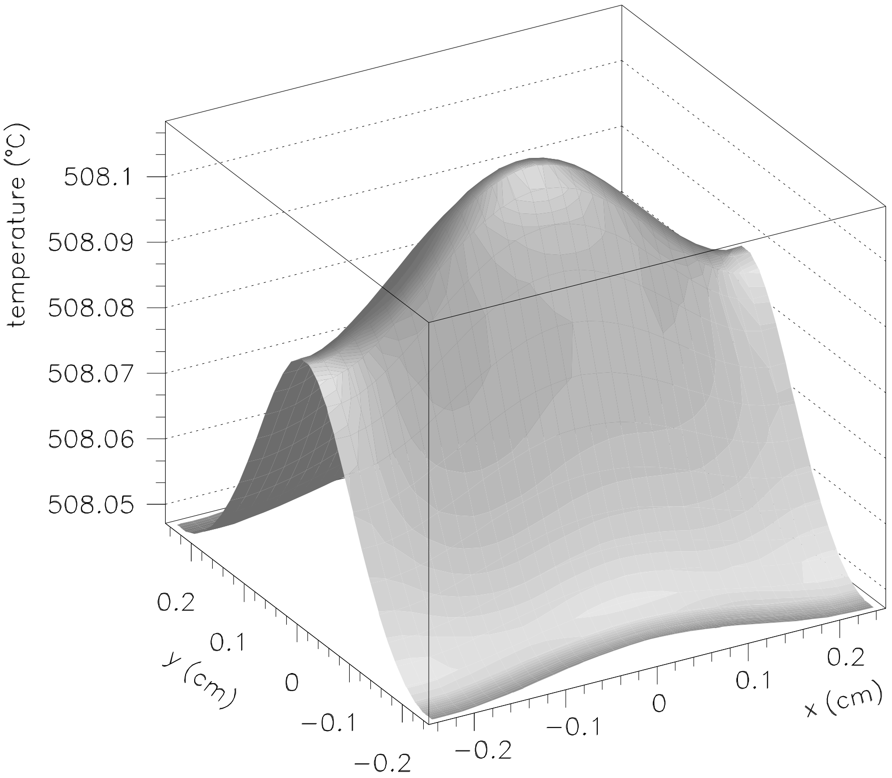

Figure 3.12: Calculated temperature profile of diamond crystal with a 12 GeV beam at the maximum electron beam current of 2 μA. The crystal dimensions are 5 mm × 5 mm × 20 microns. The ambient room temperature was taken to be 27°C (300°K). The azimuthal asymmetry is caused by the elliptical shape of the electron beam spot on the radiator.

ing can be written as

$$C_P\, a\, \frac{dT}{dt} = h(x,y) - 2\sigma \left(T^4 - T_0^4\right) + \kappa\, a \nabla^2 T$$

where the heating term $h(x,y)$ has units of power/area, σ is the Stefan-Boltzmann constant, C_P is the heat capacity and κ the coefficient of conduction for diamond, and a is the thickness of the crystal. T_0 is the ambient temperature of the environment and T is the local crystal temperature, a function of space and time coordinates. After a certain time, T converges to the steady-state solution shown in Fig. 3.12. The calculation used a crystal of dimensions 5 mm × 5 mm × 20 microns and a beam current of 2 μA. This calculation shows that the conductivity of diamond is sufficient to prevent significant temperature gradients across the crystal even for very thin wafers. It also shows that radiative cooling alone is sufficient to dissipate the heat being generated by the beam passing through the crystal and keep the entire crystal well below the graphite transition temperature. This calculation includes only radiative cooling, and shows that the crystal mount does not need to be designed to dissipate heat from the crystal. It does indicate, however, that the materials used to attach the diamond the mount must either be capable of maintaining their mechanical properties at 500°C or be sufficiently thermally conductive themselves to allow 20 mW of heat to be removed from the diamond by conduction to the mount.

Chapter 4

Electron beam

The performance of the photon source is dependent upon the parameters of the electron beam in several important areas. The most important parameters are listed in Table 4.1. The first column of numbers gives the set of parameters that have been adopted as the design goals for the source. These are the values that have been taken as input in calculating the characteristics of the coherent bremsstrahlung source. The second column of numbers was obtained from a concrete design of the Hall D beam line that was carried out by members of the Jefferson Lab Accelerator Division [13]. The exact choice of the final parameters has not yet been made, but the preliminary design exceeds the design goals for the most important parameters. In the original design goals the minimum stable current desired was 100 pA. These low current operation is needed only for calibration measurements using a total absorption counter. The presently listed minimum current of 1 nA is determined by the minimum current in the machine for the stable operation of the beam position and beam current monitors. For short runs a lower current should be possible which is sufficient for calibration purposes. The other parameters which does not meet the design goals are the dispersion in x and y. The dispersion effects the beam size through the following equation

$$\sigma(\mathrm{s}) = \sqrt{\varepsilon(\mathrm{s}) \times \beta(\mathrm{s})} + \mathrm{D}(\mathrm{s})\frac{\Delta \mathrm{p}}{\mathrm{p}} \tag{4.1}$$

where σ, ε, β, D, and p are the beam size, the emittance, the beta function, the dispersion, and the momentum respectively. A 400mm dispersion then increases the beam spot size by about 0.08 mm which is small contribution to total spot size at the radiator of 0.8 and 0.36 mm in x and y respectively. The reduction of the radiator-collimator distance from $80\,m$ to $76\,m$, which was decided in 2002, did not significantly affect the performance of the source.

parameter	design goals	2008 design
energy	12 GeV	12 GeV
electron polarization	not required	available
minimum stable current	100 pA	1 nA
maximum useful current	3 μA	5 μA
r.m.s. energy spread	< 10 MeV	2.5 MeV
transverse x emittance	10 $mm\cdot\mu$r	3 $mm\cdot\mu$r
transverse y emittance	2.5 $mm\cdot\mu$r	0.9 $mm\cdot\mu$r
x-dispersion at radiator	<2 cm	40 cm
y-dispersion at radiator	0	40 cm
x spot size at radiator	1.7 mm r.m.s.	0.82 mm r.m.s.
y spot size at radiator	0.7 mm r.m.s.	0.36 mm r.m.s.
x image size at collimator	0.5 mm r.m.s.	0.3 mm r.m.s.
y image size at collimator	0.5 mm r.m.s.	0.25 mm r.m.s.
distance radiator to collimator	80 m	76 m
position stability	± 200 μm	-
beam halo*	$< 1 \times 10^{-5}$	none

*Halo ≡ fraction of particles >5 mm from beam axis

Table 4.1: Electron beam properties that were asked for (column 2) and obtained (column 3) in the 2008 optics design for the transport line connecting the accelerator to the HALL D photon source.

Finally in Table 4.1 there is no quoted stability for the photon beam spot on the collimator. The reason for this is that the machine simulations do not give an estimate for this parameter. It will be described in later sections how the beam position is measured and stabilized.

The most important parameter in Table 4.1 is the electron beam energy. The electron beam energy defines the maximum photon beam energy and thus the range of meson masses which can be detected. With a 12 GeV beam the diamond can be oriented so that the peak in the coherent bremsstrahlung beam is at 9 GeV with an average linear polarization of 40%. This gives a sensitivity to mesons with masses up to about 3 GeV/c^2. If the beam energy were to decrease then either the photon beam energy would have to be decreased or the resulting polarization would decrease. Because of this the beam energy is seen as critical to the photon source and all simulations are based on a beam of this energy. For a fixed beam energy the beam emittance then determined how well one can use collimation to separate the coherent and incoherent bremsstrahlung components to the photon beam and also the energy width under the coherent peak. The emittance of the beam will be discussed in the next section followed by a beam polarization discussion.

The other way in which the electron bean can impact the performance of the photon source is through the generation of background in the tagging spectrometer detectors. The three main sources of electron beam generated background are from the beam halo, background from the electron beam dump, and showers generated by electrons striking the downstream end of the tagger vacuum chamber. The effect of beam halo and vacuum chamber background will be discussed with the design of the vacuum chamber and the beam dump background will be discussed when the electron dump is described.

4.1 Beam emittance

The values for the electron beam emittances shown in Table 4.1 are estimates based upon detailed calculations taking the $12 GeV$accelerator lattice as input and using both the optim and elegant machine simulation codes [13]. The definition of emittance used here is the product of the r.m.s. widths of the beam in transverse position and divergence angle. Because synchrotron radiation inside the accelerator occurs mainly in the horizontal plane, the emittance values in x are generally larger than those for y. This is reflected in the larger x emittance for the design goals and the 2008 design. The CEBAF accelerator division has produced an excellent beam transport design for the HALL Dbeam which results in an expected emittance which is more than a factor of 2 better than our original design goals.

The longitudinal emittance of the beam is important as it is the limiting factor in determining the ultimate energy resolution of the tagger. The design goal of 0.1% photon energy resolution is well matched to the energy spread expected for the CEBAF beam at $12 GeV$of 2.5 MeV.

The place where transverse emittance plays a critical role is at the photon collimator. For optimum effectiveness in collimation it is important that the virtual electron beam spot at the collimator position be as small as possible. The electron beam does not actually reach the photon collimator, being bent into the dump by the tagger magnet shortly after the radiator. But considering the optics of the electron beam as if the tagger dipole were switched off, the electron beam at the radiator can be projected forward to form a virtual image on the collimator entrance plane. The position and size of this virtual spot determines the definition of the 0° emission angle for the photons. If this spot is small compared to the collimator aperture and is correctly centered then the bremsstrahlung photons of a given emission angle α intersect the entrance plane of the collimator in a well-defined ring of radius $D\alpha$ concentric with the collimator aperture, where D is the distance between the radiator and the collimator entrance plane. In this way a collimator of diameter d passes only those photons of emission angle $\alpha \leq d/2D$. If however the size of the virtual spot is comparable to or larger than the collimator aperture then the ring image of photons of a given emission angle α is smeared out, so that the effect of collimation is simply to reduce the intensity of the beam but not to enhance the coherent component.

Note that this analysis does not place any specific limits on the size of the beam at the radiator. The beam spot can and should be larger there to increase the lifetime of the crystal between spot moves. For the SLAC coherent bremsstrahlung source the beam spot at the radiator was about $2\,mm$ r.m.s. focused down to a $1\,mm$ r.m.s. virtual spot at the primary collimator positioned $91\,m$ downstream of the radiator.

The superior emittance characteristics of the CEBAF beam allow the transverse dimensions to be much smaller than this for the HALL D source, more so in the vertical than the horizontal dimension. Previous experiments have reported significant changes in the performance of diamond radiators when the charge which passed through the crystal exceeded 0.25 C/mm^2. This corresponds to roughly 2 weeks of continuous running at maximum luminosity for GLUEX with existing size diamonds. With CEBAF's excellent emittance the spot size on the crystal can be varied to make the most efficient use of the diamond crystals. The beam can be tailored to the size of the uniform areas of the crystals and to adjust the time between spot moves.

The difference between the horizontal and vertical emittance of the CEBAF beam implies that making the spot round at the radiator implies an elliptical virtual spot at the collimator, and *vice versa*. It is difficult to construct a collimator with an elliptical aperture, so the choice was made to make the virtual spot round. This is why the beam spot on the radiator is asymmetric.

Figure 4.1 shows how the collimated photon spectrum depends upon the transverse emittance of the electron beam. To generate this plot the increases in emittance were simply translated into an increased virtual spot size on the collimator. This was done because it was assumed that the spot size of the electron beam on the radiator, already close to $2\,mm$ r.m.s., cannot be further inflated and stay contained within the limits of the crystal. When the virtual spot size becomes comparable with the collimator aperture then the collimation is rendered ineffective, and the photon spectrum and polarization revert to their uncollimated values. There is another connection between focal spot size and beam emittance that is connected with the requirement that

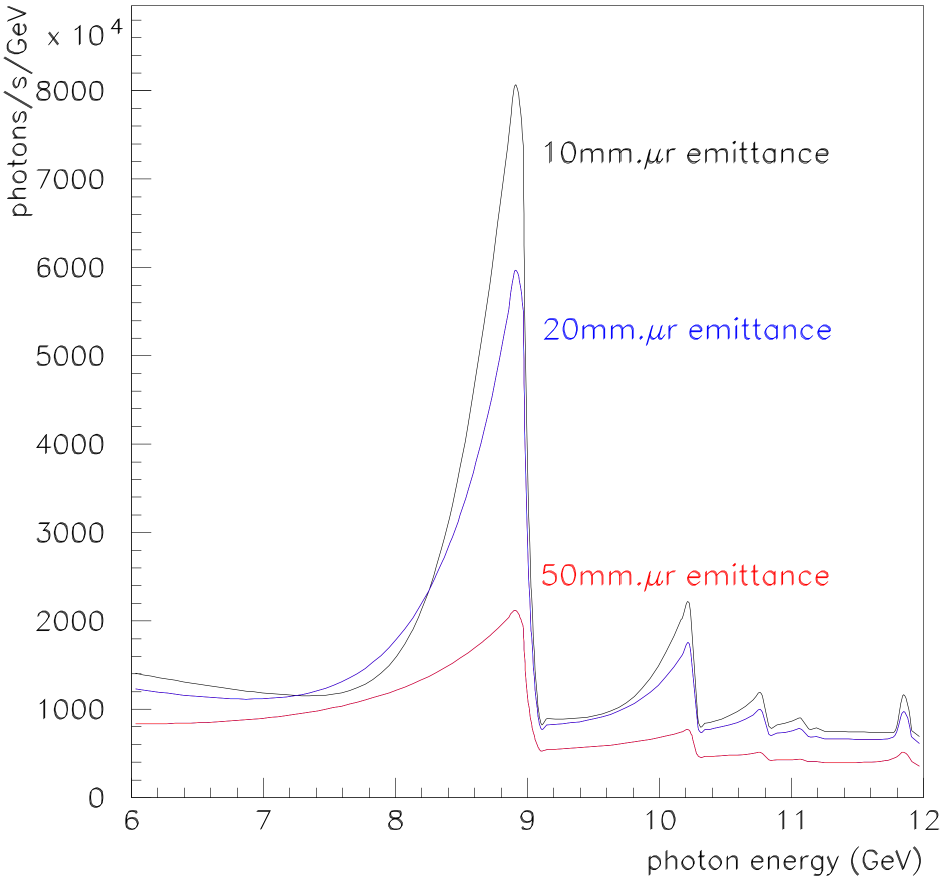

Figure 4.1: Coherent photon spectrum for three different values of the electron beam transverse emittance. The horizontal (shown on the plot) and vertical emittances are assumed to scale together. A 3.4 mm collimator located 80 m from the radiator was used for this calculation.

all electrons enter the radiator at the same incidence angle with respect to the planes of the crystal. Practically, the divergence does not broaden the coherent peak provided that it is kept below the mosaic spread of the crystal. A conservative value for the allowable angular divergence δ in the electron beam at the radiator would then be 20 μr . Taken together with a $500\,\mu m$ r.m.s. spot size at the focus, this leads to an emittance of $10\,mm{\cdot}\mu r$ at $12GeV$. This corresponds to the upper curve in Fig. 4.1.

Fig. 4.2 shows the horizontal and vertical r.m.s. beam size from the 2008 beam optics. The size of the beam is shown from 100 m upstream of the diamond radiator and projected to 100 m downstream. The design of the upstream elements allows the ratio of the spot sizes at the radiator and collimator to be adjusted over about an order of magnitude simply by changing the current in the beam line elements. In this way it will be possible to optimize the optics for a given size of crystal and collimator after beams are delivered to the hall, and more precise values for the emittances are in hand.

4.2 Beam polarization

It has already been stated that to generate bremsstrahlung photons with linear polarization it is necessary to use an oriented crystal radiator. However photons with circular polarization are produced by ordinary incoherent bremsstrahlung any time the incident electrons are longitudinally polarized. In fact for $9GeV$ photons produced by $12GeV$ electrons, the transfer from electron beam longitudinal polarization to photon beam circular polarization is greater than 80%. This raises the question of what happens when one has longitudinally-polarized electrons incident on an oriented crystal radiator. What happens in this case is that the photon beam is elliptically polarized; it carries both circular and linear polarization. There is a sum rule that limits the sum of the squares of the linear plus circular polarizations to be no greater than 1. Hence one sees the linear polarization in coherent bremsstrahlung going to zero as one approaches the end-point energy (see Fig. 3.5) while at the same time the circular polarization goes to 1 at the end-point (assuming electrons of 100% longitudinal polarization).

The statement in Table 4.1 that electron beam polarization is not required for the GlueX experiment in Hall D is correct, but it is not correct to assume that the photon source is independent of the state of polarization of the electron beam. The presence of a non-zero circular polarization in the Hall D photon beam will, in principle, produce observable effects in the angular distributions measured in photoproduction reactions. This means

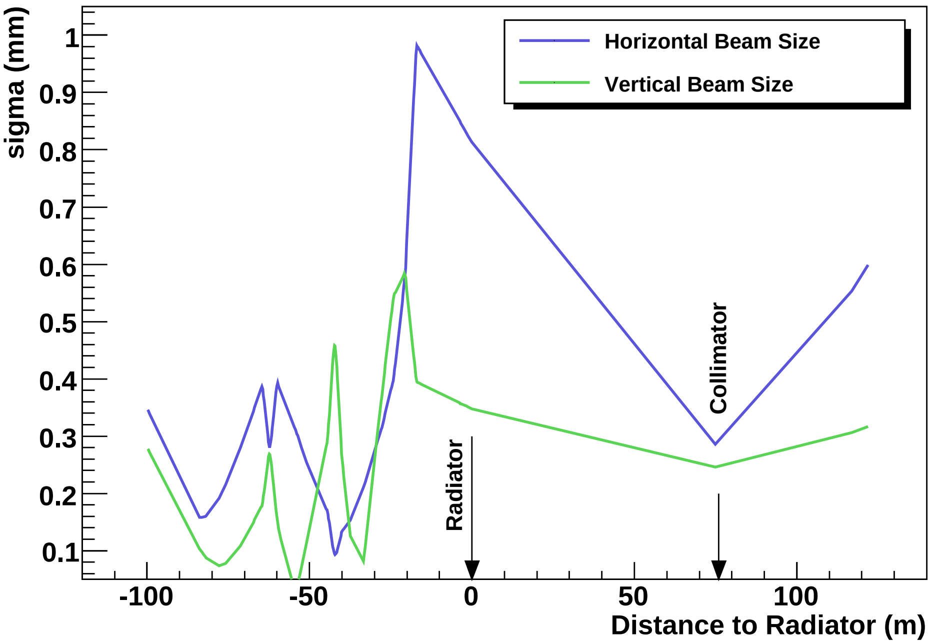

Figure 4.2: Horizontal and vertical r.m.s. envelopes for the electron beam in the region of the photon source. The origin of the z coordinate has been placed at the radiator. In the region between the radiator and the collimator the envelope refers to the projected image of the electron beam, and does not describe the size of a physical beam that exists in that region.

that there will be an important coupling between the GlueX program and the other experimental halls whose programs sometimes require them to have control over the beam polarization. This coupling can be eliminated by setting up the tune of the electron beam line to Hall D such that the longitudinal component of the electron beam polarization is rotated to zero at the crystal radiator. Whether the decision is made to rotate it away or simply to measure its value periodically, this consideration underlines the importance of having a means to measure photon beam polarization in a way that does not rely on *a priori* knowledge of the properties of the electron beam.

Although the ability of the source to produce photon beams with both circular and linear polarization complicates operation when one of them is desired without the other, it does increase the versatility of the source. The two kinds of polarization are controlled independently of one other, and together they give access to a more complete set of polarization observables than would be possible with only one or the other.

4.3 The electron beam line

The beam transport between CEBAF and Hall D is now completely designed. The elements in this design were used as input to the beam transport codes which produced the simulations shown above[13]. Details of the beam transport to the tagger hall are beyond the scope of this document. Here the electron beam inside the tagger hall will be described. The preliminary design of the Hall D electron beam line inside the Tagger Hall is shown in Fig. 4.3. At the entrance to the tagger hall is an instrumentation girder on which are mounted steering coils, beam position monitors, a beam profile monitor and a low current beam current monitor.Additionally a phosphor screen can be inserted into the beam during the setup phase of the accelerator and then remotely removed. The official designation and exact location of the devices is given in Table 4.2. An ion pump and a gate valve are the last devices in the beam before the start of the Hall-D photon source. Upon entering the tagger hall the electron beam passes through the goniometer, a quadrupole magnet, and is bent by the tagger dipole magnet towards the electron beam dump. Details of the quadrupole and tagger dipole will be given in the next section. After the tagger magnet is another machine vacuum isolation valve. The electron beam dump is also shown in Figure 4.3. Beam position monitors, a beam current monitor, and another phosphor screen are mounted in the beamline near the dump to monitor the beam as it enters the dump.

These devices plus additional magnets and instrumentation upstream of

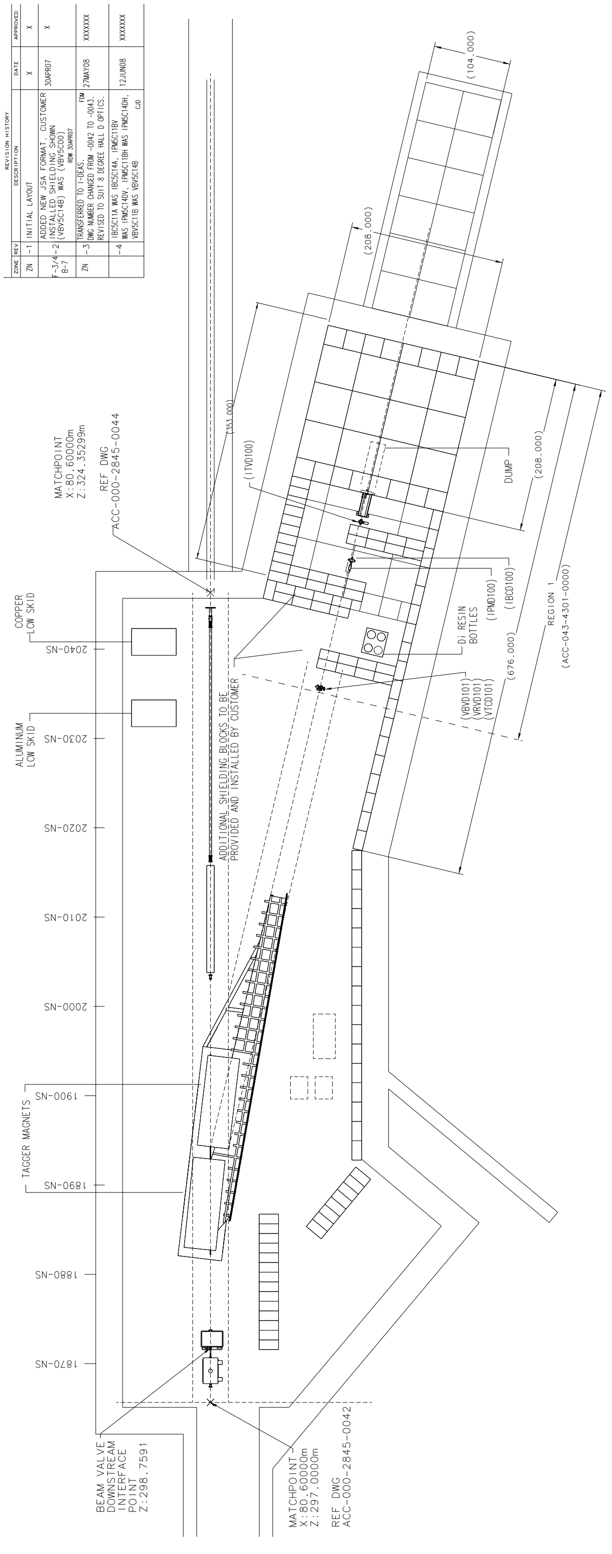

Figure 4.3: Layout of the tagger hall including equipment from the Machine Group.

Upstream devices			
Device Name	Description	Z pos (m)	X pos (m)
IPM 5C11B	Beam Position Monitor (BPM)	-4.1511	0
IHA 5C11A	Harp wire scanner	-3.9871	0
ITV 5C11A	Viewer (phosphor screen)	-3.8621	0
MBD5C11AH	Horizontal steering magnet	-3.6363	0
MBD5C11AV	Vertical steering magnet	-3.4402	0
VIP5C11A	Ion Pump	-3.2185	0
iCLnApm2	Low-current BPM	-1.1263	0
Downstream devices			
Device Name	Description	Z pos (m)	X pos (m)
IPMD100	Beam position monitor (BPM)	26.3013	-4.7576
1BCD100	Beam current monitor	26.4973	-4.8043
VBVD101	Beam Viewer	27.8581	-5.1285

Table 4.2: Summary of the Hall-D electron beam instrumentation. The first column is the name of the instrument, the second column is a description of the instrument, and the last two columns are the location in X and Z of the devices in the goniometer coordinate system. The table is grouped into instruments upstream of the goniometer and devices downstream of the tagger magnet's vacuum chamber

the tagger hall are sufficient to center the beam on the goniometer crystal and steer the beam into the beam dump. However with 76 m between the radiator and the collimator additional diagnostics and controls are needed if the photon beam is to be centered on the collimator with a precision 200 μm. In order to maintain a stable beam position on the collimator, the SLAC experiment [2] instrumented the collimator with a secondary-emission detector. The detector was of the "pin-cushion" design and was installed between segments of the collimator near the position of the shower maximum. The readout was divided into four quadrants, which read equal currents when the beam was properly aligned on the collimator. The readout was connected via a feedback loop to the last steering elements on the electron beam line prior to the radiator. Over that distance a bend of only 10 μr results in a shift of $1\,mm$ at the collimator position. The small deflections that are necessary to keep the beam centered on the collimator do not produce appreciable walk in the beam-crystal angle. This means that an active feedback system can be set up between the instrumented collimator and deflection coils just upstream of the radiator, that can operate independent of the crystal alignment system to keep the electron beam aimed at the center of the collimator. Based on the SLAC design a "pin-cushion" secondary emission counter has been partially constructed and tested at JLAB. This detector is described in detail it the photon beam line chapter. The experimental program in parity violation at Jefferson Lab has already demonstrated a position stabilization circuit that is able to keep the beam position steady to within $20\,\mu m$ over a $20\,m$ lever arm. A less sophisticated version of this circuit will meet the position stability requirements for the Hall D photon source.

4.4 Electron beam dump

The electron beam is dumped in the horizontal plane, as shown in Figure 4.3. The horizontal bend offers several advantages over dumping the beam into the ground. The tagger magnet is easier to support if it sits in the horizontal position. It is also easier to mount and service the focal plane in this position. The dump itself is also more accessible in case it needs to be serviced. An above-ground dump also affords the possibility of running parasitic beam dump experiments that do not interfere with the operation of the experimental hall.

The design requirement for the electron beam dump is that it has a sufficiently high capacity to handle beams of the highest intensities foreseen for the GlueX experiment in Hall D. A $60\,kW$ design would provide for operation of a $12 GeV$ beam at $5\,\mu A$ and sufficient capacity to handle $3\,\mu A$at $20 GeV$ in

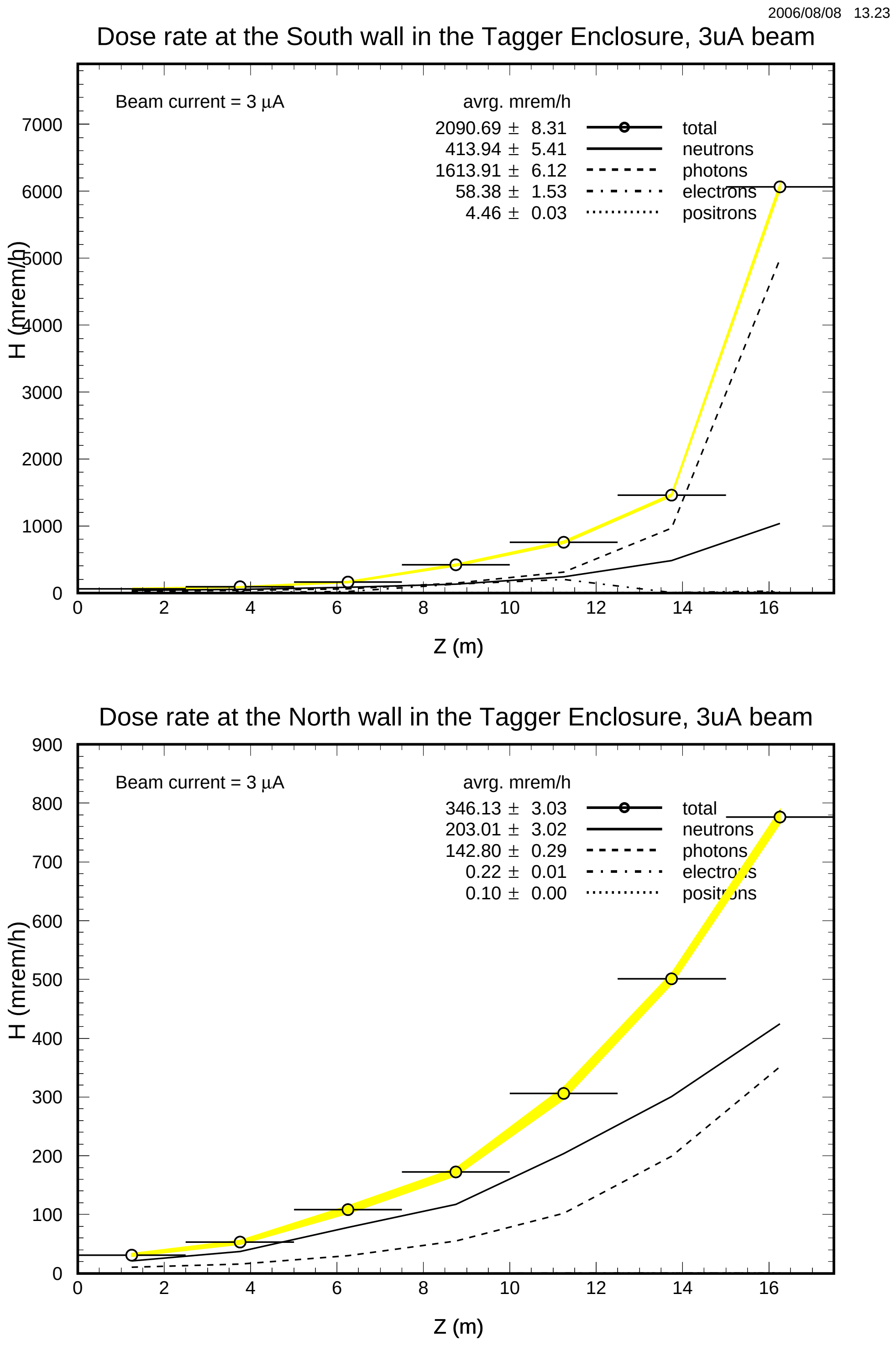

Figure 4.4: The simulated dose in the tagger hall is shown along the hall's South (top panel) and North (bottom panel) wall. z=0 is at the entrance to the hall.

the case of a further upgrade.

One major concern influencing the design of the electron beam dump is the effect of radiation streaming from the dump enclosure causing background in the experimental equipment in the tagger hall. The layout was optimized to provide adequate distance from the dump to the tagger hodoscope and thickness of the labyrinth walls separating the dump from the tagger area. Figure 4.3 provides a view of the electron dump. This layout calls for a labyrinth of two 3-foot thick concrete block walls, and two SEG (IRON) block widths, with 2 doors of at least one inch thick borated polyethylene sheets that help to absorb the thermal neutrons created from attenuation of the fast neutrons. The dose in the hall along the North and South walls of the tagger hall were simulated in GEANT and are shown in Figure 4.4.[14] The simulation assumed typical run conditions of 3 μA and 12 GeV. This simulation indicated an insignificant contribution to the hodoscope detector rates from the dump, compared to the radiation produced by the showers in the tagger vacuum chamber and in the South wall. The final design satisfies the physics requirement of less than 1% background interference from backscattered radiation from the dump.

4.5 Electron beam containment and shielding

The Personnel Safety System (PSS), Machine Protection System (MPS) and Beam Envelope Limit System (BELS) are engineered controls that ensure the CEBAF accelerator is operated safely. The PSS is comprised of access controls and safety interlocks that ensure personnel are protected from prompt ionizing radiation. No personnel are allowed entry to the beam enclosure during beam operations. The tagger area PSS will have access controls similar to the existing CEBAF experimental halls. An access room, located at the top of the tagger truck ramp includes an interlocked ante-room; exchange key entry system, and remote video monitoring. When the tagger area is open for access beam transport from the CEBAF linacs to the tagger is blocked by two monitored beam stoppers and shut down of the vertical bend dipole magnets. Accesses during search and secure and controlled access operations are monitored by a qualified safety system operator in the machine control center. An additional safety function not found in the existing experimental halls is the requirement to prevent electron beam transport from the tagger to Hall D. To achieve this three additional PSS controls will be used:

1. A Beam Transport Monitor that will only permit beam transport if the energy setting of the vertical bend is equal to the energy setting of the

tagger dipole magnet.

2. A permanent magnet placed in the photon line that deflects charged particles out of the photon beam line.
3. Ion chambers to detect transient beam loss associated with failed optics.

The tagger Machine Protection System (MPS) is an extension of the existing CEBAF MPS architecture. Fast shutdown (FSD) modules are linked in a tree structure back to the CEBAF injector. The FSD will monitor interlocks on the beamline and tagger dump. FSD inputs include vacuum/valve status, beam dump cooling, radiator status, and the experiments inhibit. Beam Loss Monitors (BLM) will be positioned at tight apertures and bends where loss is most likely. Ion chambers (ICs) will be positioned near the radiator to detect beam loss in a thick target. The existing CEBAF Beam Current Accounting (BCA) System will include a cavity monitor at the tagger beam dump. The BLM, ICs, and BCA trip the beam off through the FSD network when a fault is detected. If any gate valve closes or there is a vacuum failure the beam will also be disabled. The Beam Envelope Limit System (BELS) system monitors the total beam power in CEBAF to ensure the JLab operations and DOE safety envelopes are not exceeded. The existing BELS will be extended to account for beam power directed to the tagger/Hall D. Energy calculated from the BTM is multiplied with the value of the current measured in the BCA system. A local limit for the tagger area will provide protection for the beam dump. In addition, the beam power in the tagger dump is combined with the beam power for the other experimental areas to verify the total beam power for the facility.

4.5.1 Other Engineered Controls

The tagger area is constructed of concrete shielding and an earthen berm. Dedicated simulations of the shielding for the tagger hall have been performed by the JLAB radiation control group and shielding requirements incorporated in to the civil design. The existing design exceeds the requirements of JLab radiation control policy and 10CFR 835. The power for the dipole magnets that bend the electron beam up towards the surface then bend it back horizontal in the tagger area will be connected in series so that failure of a magnet supply or current control electronics cannot result in the beam being steered into the ceiling of the tagger building.

Chapter 5

Tagging spectrometer

5.1 Specifications and introduction

To satisfy the needs of the GlueX physics program, the tagged photon spectrometer should meet the following specifications:

1. Photon energy detection from 70% to 75% of E_0 with energy resolution of about 0.1% r.m.s. Percentages refer to the primary beam energy E_0, i.e. for a $12 GeV$ beam an energy resolution of $12 MeV$ is needed for photons between 8.4 and $9 GeV$.

2. A detector system which allows a counting rate of at least 5×10^6 electrons per second per 0.1% over this range of photon energies.

3. An additional capability for photon energy detection from 25% to 90% of E_0 (3 to 10.8 GeV if E_0=12 GeV), with less stringent resolution and count rate requirements.

4. A quadrupole magnet between the radiator and dipole spectrometer which images the beam spot on the radiator onto a line on the focal plane. This feature makes it possible to envision the use of focal plane counters with two-dimensional readout, with which one could enhance the tagging efficiency of the source. Focal plane detectors with two-dimensional readout are considered as a possible upgrade beyond the baseline design presented in this chapter. Any improvements obtained using this technique would be over and above the performance figures presented in this report.

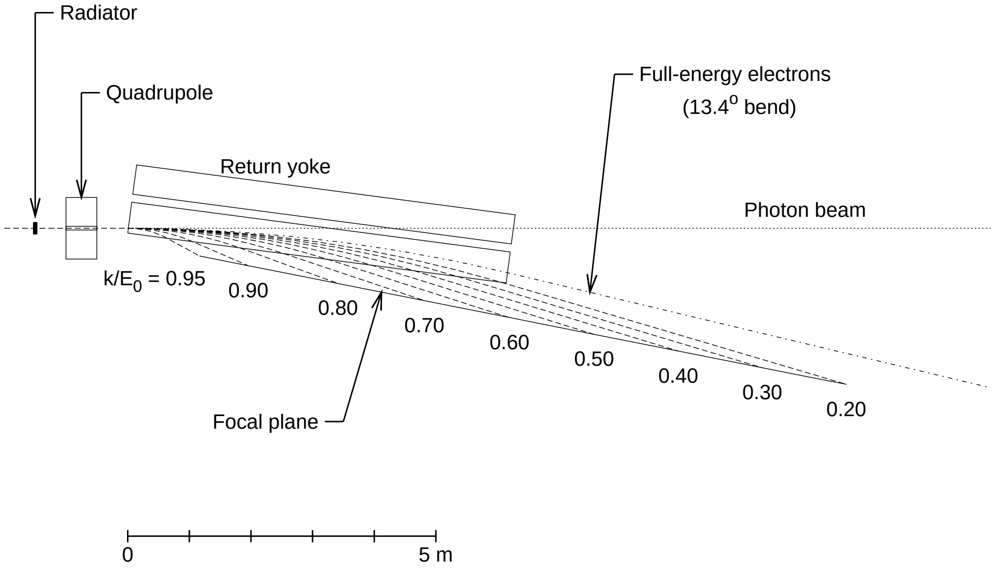

Figure 5.1: A plan view of the tagging spectrometer from above, showing the path of the primary beam and the trajectory of post-bremsstrahlung electrons of various recoil momenta.

The system described below, based on a room-temperature design, meets all of these criteria. The option of a superconducting design was also studied. With a superconducting magnet, the spectrometer could operate at much higher fields, offering the possibility of some space savings in the size of the tagger focal plane array. An iron yoke design was found which would clamp the 5 T field sufficiently to make it possible to operate normal phototubes on the nearby tagger focal plane. However, as shown below, rate considerations require a degree of segmentation in the tagging counters such that it is impractical to increase the dispersion along the focal plane above what is provided by a 1.5 T room temperature magnet. Given that there was no liquid helium available in the tagger hall, the savings in electrical power did not justify the additional cost and complexity of a superconducting magnet.

The tagging spectrometer is an Elbek-type spectrometer and is shown schematically in Figure 5.1. The 12 GeV electrons pass through the radiator target where a small fraction undergo a bremsstrahlung interaction. The electrons then pass through a focusing quadrupole and are bent by the 6.3 m long tagger magnet. The majority of the electrons which did not interact with the radiator are bent by 13.4° and then propagate straight to the electron beam dump. A large vacuum vessel is integrated into the magnet and extends out to the spectrometer focal plane so only the small amount of multiple scattering inside the diamond radiator and in the exit window effect the resolution. The spectrometer detectors are positioned immediately outside the focal plane.

The detector package is divided into two parts: a set of 190 fixed scintillation counters spanning the electron momentum range from 0.6 to 9 GeV, and a movable "microscope" of 500 scintillating fibers optimized for normal operation spanning the energy range from 8.4 to 9 GeV.

The fixed array provides access to the full tagged photon spectrum, albeit at a modest energy resolution of 0.5% and reduced photon spectral intensity. These detectors are well suited for running with a broadband incoherent bremsstrahlung source. They enable experiments to be performed with the highest photon energies possible with the source. When running with a coherent source they play an essential role in the crystal alignment procedure, and provide a continuous monitor of the performance of the source. The microscope is needed in order to run the source in coherent mode at the highest polarization and intensities, and whenever energy resolution better than 0.5% is required. Using the microscope, the source is capable of producing photon spectral intensities in excess of 2×10^8 photons/GeV, although accidental tagging rates will limit normal operation to somewhat less than this.

5.2 Magnet

The tagger magnet (Fig. 5.2) is similar to the existing tagger magnet in Hall B of Jefferson Lab [15]. The higher energy of the HALL D beam is largely compensated for by going to smaller bend angles, so the sizes of the magnets are comparable, and much of the experience from Hall B can be carried over. Unlike the Hall B tagger, which bends vertically, the HALL D tagger will deflect electrons in the horizontal plane, with both the detector hall and the beam dump constructed above ground.

The main parameters of the magnet are given in Table 5.1 and a cross sectional view is shown in Figure 5.2. The magnet is 1.13 m wide 1.41 m high and 6.3 m long and weighs a total of 80 metric tons. The pole tips are 470 mm wide 6.2 m long with a gap of 30 mm. The nominal operating field is 1.5 T though the coils are designed to operate at enough current for 1.8 T.

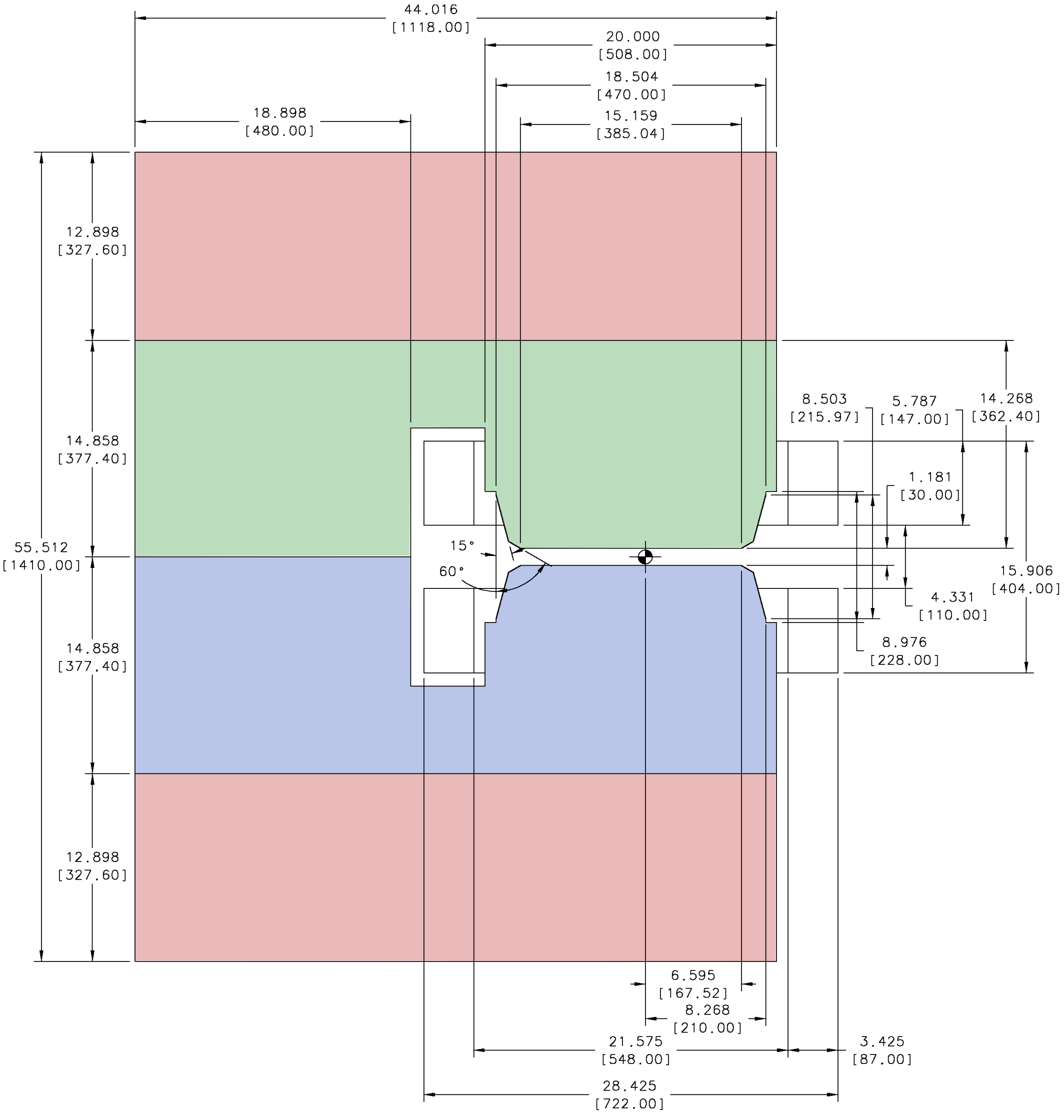

Figure 5.2: A section view of the tagging spectrometer's dipole magnet. The magnet is constructed of four 6.3 m long iron slabs. The two water cooled copper coils are shown but not the vacuum chamber. Dimensions are inches [mm].

Radius of curvature	26.7 m
Full-energy deflection	13.4^{O}
Field at 12 *GeV*	1.5 Tesla
Gap width	3.0 cm
Length of pole	6.3 m
Weight	80 tons
Length of focal plane (25% to 97% of E_0)	10.1 m
Coil power	220 A at 105 V

Table 5.1: Design parameters for the tagging spectrometer dipole magnet

At 1.5 T, the magnetic field inhomogeneity should be less than 1 part in 10^4 along any 100 mm length lying inside an area defined by the root of the pole stem. Within this area the maximum variation in the magnetic field should be less than 1 percent. To achieve this the pole faces must be parallel such that the variation in the pole gap is less than 0.02 mm along any 100 mm length on a pole surface. The variation in gap size should be less than 0.2 mm over the complete area of the poles. The variation in the pole gap between zero field and a field of 1.5 T should be less than 0.2 mm at any point on the vacuum chamber sealing surface. The magnet is constructed of four iron pieces which are bolted and pinned together. The maximum weight of a single piece is 25 t.

At the previous review in December 2006 a two magnet design was presented. Recently the advantages of a one magnet versus a two magnet design were investigated. In the present design the weight of the individual pieces is the same as in the previous two magnet design. Therefore the infrastructure for assembling the magnet is the same for both options. The raw material to manufacture the 6.3 m long magnet is available and several companies have facilities to manufacture these components. Detailed inquires into known magnet manufacturers indicated that only minimal cost difference existed between the two designs. The single magnet design has several performance advantages over the two magnet design. With a single magnet one does not have to align the two magnets to each other. This simplifies the magnet support and reduces the risk of vacuum leaks at the o-ring seal between the vacuum chamber and pole tip. Each pole tip will be made from a single piece of iron which will minimize variations in the magnetic field along the length of the magnet coming from chemical variations in the iron. The pole tip can be machined at the same time as the return yoke's horizontal plane. Therefore, the surfaces which define the poles relative alignment can be machined at the same time the pole

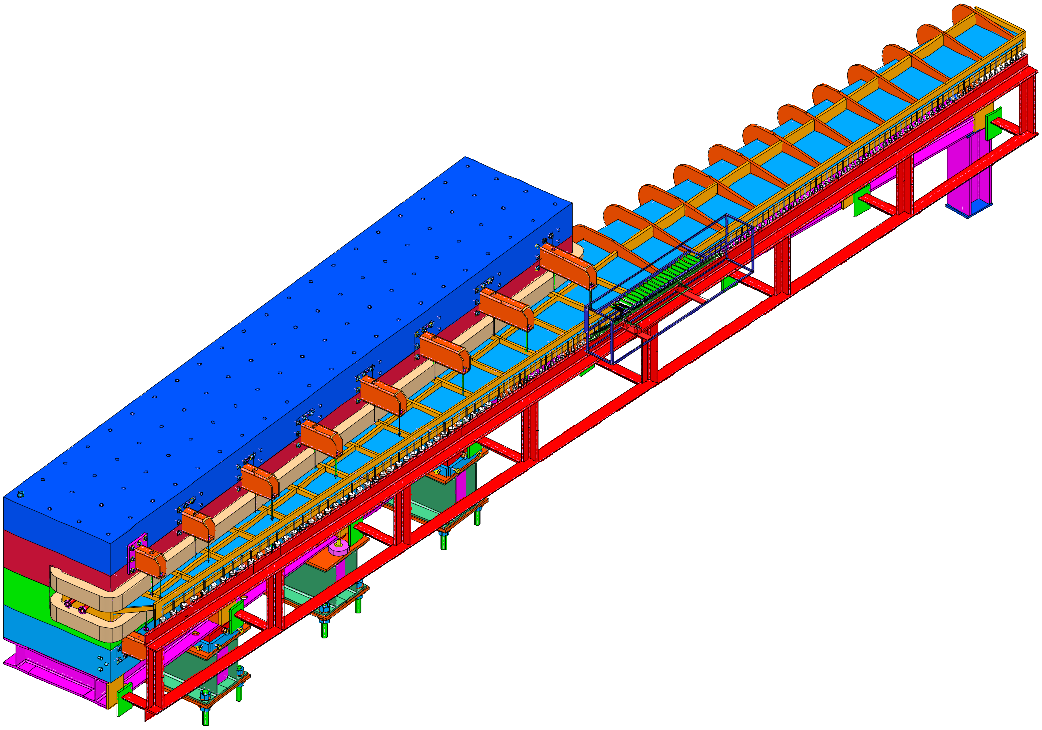

Figure 5.3: A 3-D model of the Hall D tagging spectrometer. The dipole magnet with the integrated vacuum chamber is shown. The magnet is supported with a 3 point adjustable support. Also shown in this figure are the fixed hodoscope array and the microscope detector package.

is machined, resulting in the best relative alignment possible. The alignment of the vacuum chamber is also simplified as there are only two sealing surfaces. Based on this it was decided to go back to the one magnet design.

The complete assembly of the magnet an vacuum chamber with the detector packages is shown in Figure 5.3. The magnet will be supported and adjusted from 3 points underneath. The deflection of the magnet due to it's own weight with this support is less than 25μm. The adjustment hardware consists of wedges that allow ±9 mm of adjustment in the vertical direction. In the horizontal plane, adjustment capability will be ±1 cm. This will easily compensate for the 1 inch maximum differential settling of the tagger hall and Hall D. Feducial marks will be provided for alignment on the iron yoke and transfer measurements performed to exactly measure the location of the feducials relative to the pole tips. Both hand calculations and a finite element

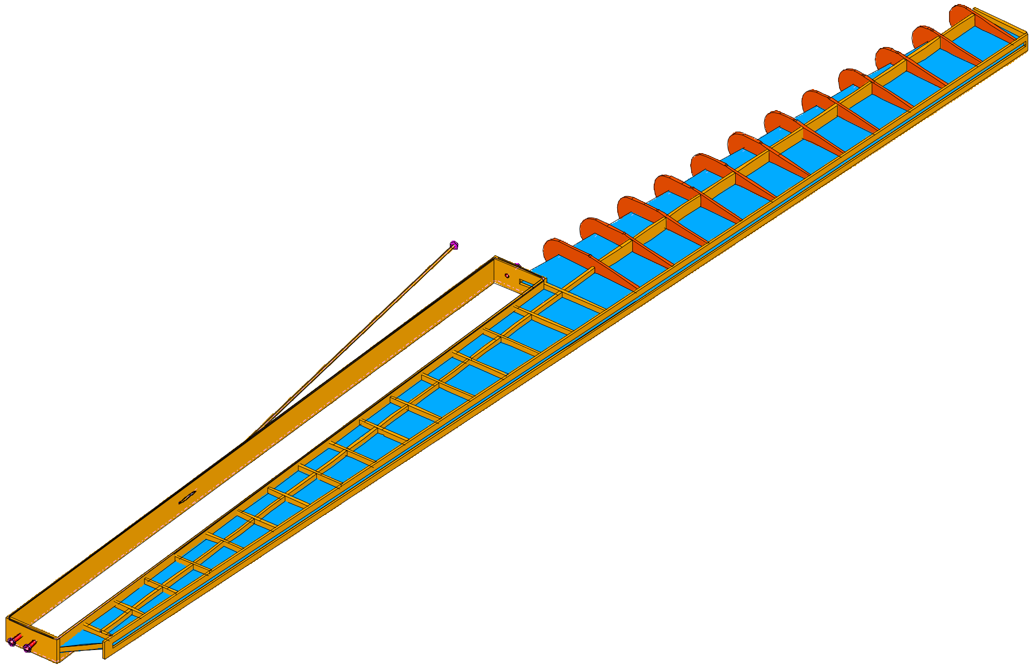

Figure 5.4: A 3-D model of the Hall D tagging spectrometer's vacuum chamber.

simulations estimated the magnetic force between the poles to be about 240 tonnes[16]. This is much more than the vacuum forces on which are about 75 tonnes. The magnetic force must be carried by the bolts which hold the iron plates together. An array of 1.5" (3.8 cm) bolts spaced every 12" (30 cm) which are installed under predefined load are sufficient to keep the assembly under tension. With this construction the total deflection of the poles under full load is about 0.1 mm. In this design 16 brackets are used to support the vacuum chamber from the magnet yoke.

The vacuum chamber for the tagging spectrometer is shown in Figure 5.4. The vacuum chamber is constructed with a 1/4" stainless steel shell and 1" reinforcing ribs. Maximum deflection of anywhere in the chamber is limited to 2.5 mm. Since the nominal opening in the chamber is 45 mm and only 30 mm is required, this is acceptable. The flange for the 11 m long exit window is 1" thick. The frame running around the pole tips is constructed of $1 - 1/4"$ and 3/4" Stn.Stl. plate. The plan to use o-rings to seal the vacuum chamber to the poles has been explored.

Radiation levels are assumed to be low enough to not degrade the elasticity of the o-rings for several decades. A 3/8 inch (9.5 mm) diameter viton o-rings of Shore A hardness of 70 will be used. In order to compress this o-ring to nominally 25%, 27,000 lbs will be required. The weight of the magnet alone will be sufficient to compress the o-ring. The tolerances on the machined parts are designed to ensure there is a minimum of 20% and a maximum of 30% compression in the o-ring. This will ensure vacuum integrity is maintained. The downstream photon beamline is 1" in diameter and ends in a standard conflat flange. The exit window will be constructed of thin aluminum foil. The downstream end of the vacuum chamber is still being designed. The design will be determined based on background in the fixed hodoscope array and the microscope.

The magnet will be assembled in place in the tagger hall. 12.5 t lifting eyes in the hall ceiling in the entry allow the pieces to be lifted from a truck and placed on rollers on the floor. Two lifting eyes will be used to lift each section. The pieces are moved next to the stand where a fixed crane will pick them up and stack them on the magnet stand. Care must be taken with the vacuum chamber; spacer blocks must be inserted in the chamber gap to support the 27,000 lbs load caused by the o-ring compression. As the weight of one of the iron plates is roughly the force needed to compress the o-ring no additional clamping is needed for this. The spacer blocks can be removed after the support brackets are installed.

5.3 Spectrometer optics

The optical properties of the tagging were optimized using the TRANSPORT program. For this and all other simulation in this section the CEBAF 12 GeV electron beam design goal parameters which were summarized in Table 4.1 were used. The setup of the TRANSPORT simulation is shown in Figure 5.5. A hard edge approximation was used for the fringe fields in this simulation and a magnetic field of 1.5 T in the high field region. If the input edge of the magnet is not perpendicular to the electron beam the entrance to the magnetic field will act as a lens. However the focal length associated with realistic entrance angle is much longer than the the total drift distance so this effect is not important for this design. Therefore it is assumed in these studies that the pole tips are rectangular. The remaining free parameters then are the distance between where the electrons enter the magnetic field and the outer corner of the field (I-B in Figure 5.5) and the and the angle between the output edge of the magnet and the original electron beam axis (this is the rotation angle of the magnet). A solution was sought which provided the optimum

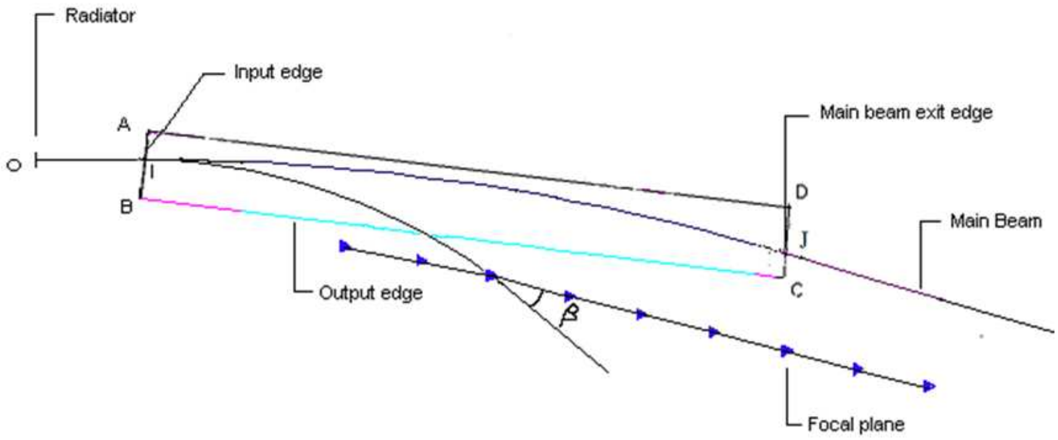

Figure 5.5: Tagger spectrometer geometry used in a TRANSPORT simulation. The magnetic field was modeled with a hard edge approximation. The two parameters which were optimized were the angle between the output edge of the magnet and the beam axis and the horizontal distance from point I and point B (Horizontal shift in the magnet). A field of 1.5 T was assumed.

momentum resolution with the minimum length of the focal plane. As the budget for the magnet is fixed solutions which required much wider poles than the previous design were rejected. The design requirement needed to fulfill the physics goals of GlueX is that the momentum resolution between electron energies of 3 and 11 GeV be better than 0.1%. The resolution is defiend as

$$\mathrm{R} = \frac{\Delta\omega}{\mathrm{D}} \tag{5.1}$$

where $\Delta\omega$ is half the radial image size in the focal plane and D is the dispersion.

The best solution found was when the magnet is rotated by 6.5° and the distance from the point where the electrons enter the field to the magnet output edge (I-B in Figure 5.5) is 210 mm. The results of this study compared to the previous best design based on two magnets is shown in Figure 5.6. The point-to-point focus is the location where all electrons of a given energy which start at a single point on the radiator will be focused to a point. The parallel-to-point focus is the point where all particle traveling parallel to each other will be focused to a single point. The focal planes for both point-to-point and parallel-to-point focusing are slightly curved. A straight focal plane has the advantage that the detectors then lie on a line making construction and alignment easier. Therefore a straight focal plane between the other two

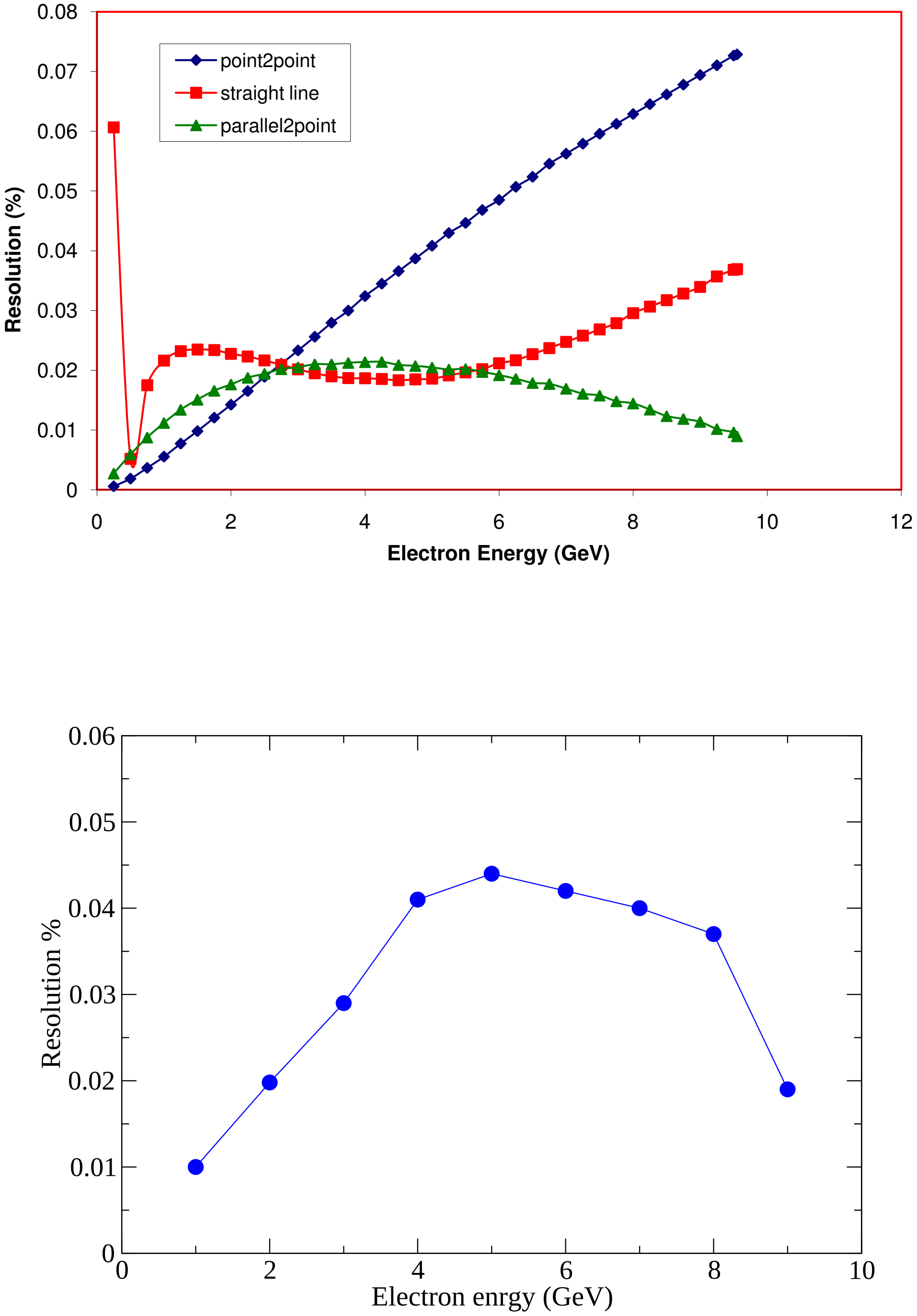

Figure 5.6: The tagger resolution as a function of electron energy as calculated with the TRANSPORT program. The top panel shows the resolution for the new single magnet design and the bottom panel the resolution for the older two magnet design. A 1.5 T field was used for both designs.

options was also studied. In Figure 5.6 the straight focal plane is optimal solution. It has resolution which is fairly flat between 500 MeV and 10 GeV. The resolution is typically between 0.02 and 0.04% of E_0. This is much better than the design requirement of 0.01% of E_0 and is also significantly better than the resolution found in the previous two magnet design.

Based on the very positive results from the TRANSPORT simulations a detailed model of the magnet was developed in TOSCA. This magnet fulfills the requirements all the requirements listed in the magnet section. Ray tracing calculation were then performed to generate exact numbers for the dispersion and resolution. The results of these calculations are summarized in Table 5.2. In general the resolution is very similar to what was found using TRANSPORT.

At the focal plane, the characteristic bremsstrahlung angle corresponds to a few millimeters of transverse displacement. The vertical beam spot size at the radiator (0.5 mm r.m.s.) contributes a comparable amount because of the large transverse magnification in the dipole transport matrix. However, placing a quadrupole magnet between the radiator and the tagger dipole magnet reduces this magnification nearly to zero over a substantial range of photon energies without substantially changing the other optical properties. Including the quadrupole in the design makes possible a future upgrade of the photon source to employ tagging detectors with two-dimensional readout. The impact of the quadrupole is demonstrated in Figure 5.7. Here 3 GeV electrons were traced through all magnetic fields up to the focal plane. In this study particles were tracked which start with the same angle but different positions on the diamond radiator. The top panel show the trajectories of particle when the quadrupole field is zero. The bottom panel shows the trajectories when the quadrupole is properly adjusted. The quadrupole which will be used is the JLAB QP quadrupole which has a pole tip half aperture of 1.81 cm, an effective length of 31.26 cm, and a maximum gradient of 27 T/m. In this model the distance from the end of the quadrupole to the entrance to the dipole field is 220 cm. The optimum operating gradient was -0.5215 KGs/cm (-5.215 T/m).

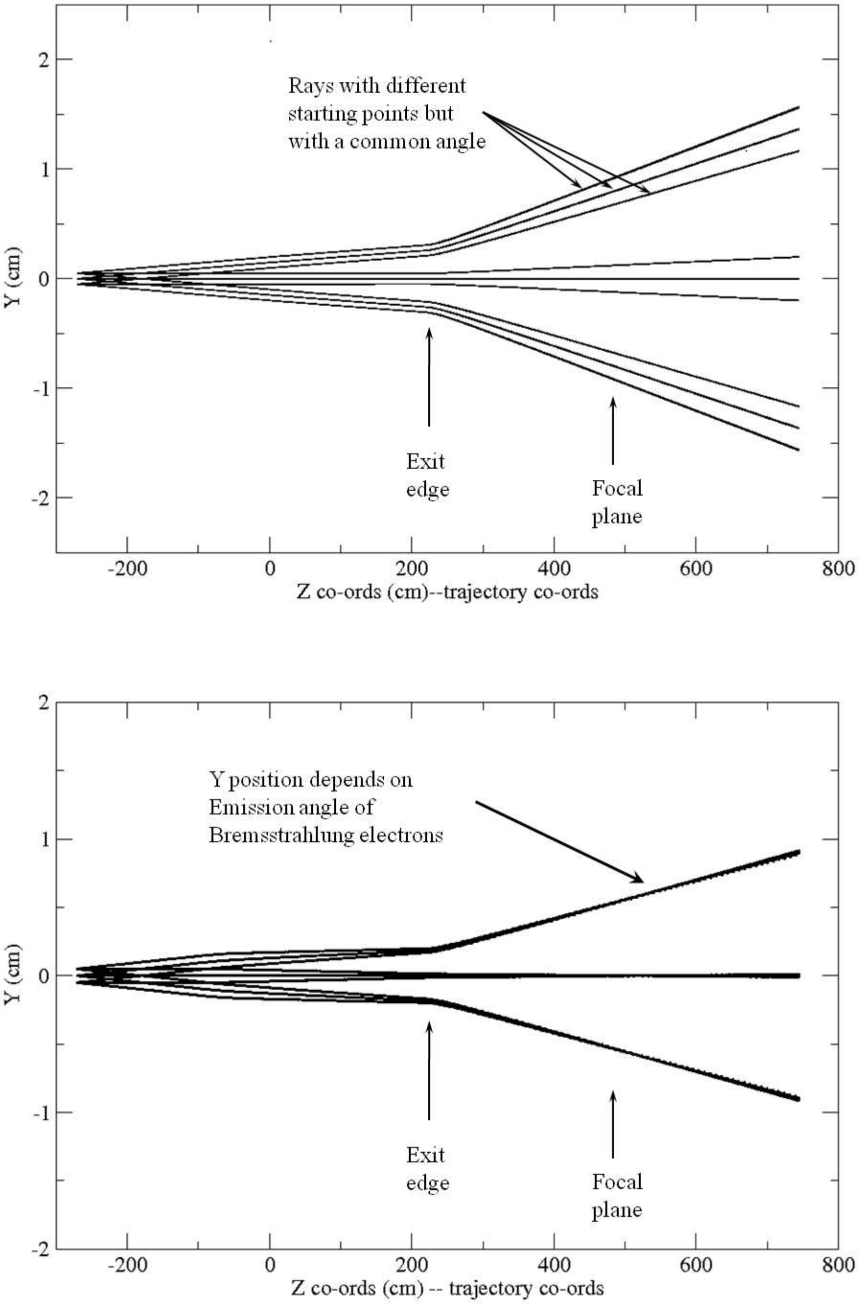

Figure 5.7: The vertical spot size on the focal plane is shown with and without the quadrupole between the diamond radiator and the tagger magnet.

k	(x x)	(y y)	(y y')	Δk_{beam}	Δk_{spot}	Δk_{tot}	Δy_{tot}	y_{char}
(GeV)	(mm/mm)	(mm/mm)	(mm/mr)	($\%E_0$)	($\%E_0$)	($\%E_0$)	(mm)	(mm)
Without quadrupole:								
6	-0.3196	2.1520	19.886	0.080	0.0305	0.0856	1.0760	0.8451
7	-0.2842	2.1072	17.832	0.080	0.0265	0.0843	1.0536	1.0610
8	-0.2444	2.0537	15.739	0.080	0.0235	0.0834	1.0269	1.3378
9	-0.2002	1.9869	13.576	0.080	0.0215	0.0828	0.9935	1.7310
10	-0.1535	1.8966	11.284	0.080	0.0202	0.0825	0.9483	2.3977
11	-0.1265	1.7464	8.657	0.080	0.0157	0.0815	0.8732	4.0472
With quadrupole: (length = 30.126 cm, gradient = -0.52 kGauss/cm)								
6	-0.1934	0.6513	18.921	0.080	0.0212	0.0828	0.3256	0.8041
7	-0.1422	0.5048	16.802	0.080	0.0186	0.0821	0.2524	0.9997
8	-0.0810	0.3032	14.613	0.080	0.0187	0.0822	0.1516	1.2421
9	-0.0054	0.0002	12.299	0.080	0.0202	0.0825	0.0001	1.5681
10	0.0915	-0.5318	9.722	0.080	0.0228	0.0832	-0.2659	2.0659
11	0.1930	-1.8441	6.346	0.080	0.0216	0.0829	-0.9220	2.9666

Table 5.2: Optical properties and resolutions of the tagging spectrometer at the focal plane, for $E_0 = 12\ GeV$: (x x),(y y),(y y') = first-order transport matrix elements where x and y are radial and transverse coordinates respectively; the focal plane is defined by (x x')=0.; Δk_{beam} = r.m.s. energy resolution due to beam energy uncertainty; Δk_{spot} = r.m.s. energy resolution due to spot size on radiator; Δk_{tot} = total r.m.s. energy resolution excluding detector size; Δy_{tot} = transverse r.m.s. position resolution due to spot size on radiator; y_{char} = transverse size corresponding to one characteristic electron angle $\theta_{Ce} = (m/E_0)(k/(E_0 - k))$.

5.4 Tagger detectors

The Hall-D tagging hodoscope serves the momentum analysis of electrons that scattered off the radiator producing bremsstrahlung photons. The photon energy E_γ is determined as difference between initial electron beam energy (E_0) and energy of the scattered electron (E_e) deflected towards the focal plane. Arrays of scintillation counters along the focal plane allow for detection of scattered electrons with coarse resolution for almost the full energy range and high resolution for energies near the coherent peak. This is realized by instrumentation of two separate detector components:

1. a movable high-resolution device covering the coherent peak, nominally positioned to cover the energy range between 8.5 to 9 *GeV* (see Section 5.4.1);
2. a coarse resolution device sampling the full energy range from 25% to 97% of E_0 (see Section 5.4.2).

5.4.1 Focal plane microscope detectors

The design energy resolution of 0.1% r.m.s. (see Table 5.2) could be met by non-overlapping detectors which span an energy range of 0.2% each (the r.m.s. deviation of a flat distribution of width W is $W/\sqrt{12} = 0.29W$.) The principal limitation on detector size is imposed by the design goal of tagging collimated photons at rates up to 100 *MHz* over the coherent peak. The nominal collimated coherent peak has its highest intensity between about 8.5 and 9 *GeV* (see Fig. 3.3). However, the the tagger sees the scattered electrons for both collimated and uncollimated photons, and the total tagging rate in this region is about twice the collimated rate (see Fig. 3.3), about 200 *MHz*. If a single phototube can count reliably at 5 *MHz*, then the energy range detected by a single scintillation counter should be $5\,MHz/200\,MHz \times 600 MeV = 15 MeV = 0.12\%$ of E_0. Thus a detector width of 0.1% would satisfy the requirements of both resolution and rate. According to Table **??**, such a detector would have a width of 2.5 *mm* perpendicular to the electron direction, and detectors for individual channels would be spaced about 17 *mm* apart along the focal plane.

5.4.2 Fixed focal plane array

Tagging of photons over the full range from 25% to 97% of E_0 is not required as part of the physics program here proposed for GlueX, but is desirable for two separate reasons. First, it will increase the flexibility of the source by allowing other possible experiments using highly polarized photons below $8GeV$, or incoherent bremsstrahlung up to $11.7GeV$. This capability is not available elsewhere at JLab, since the Hall-B tagger will not handle beam energies above $6.6GeV$ and the linear photon polarization will be quite low for photon energies above about $4.5GeV$. Second, the process of aligning the crystal radiator for coherent bremsstrahlung requires rotation about several axes and rapid observation of the resulting energy spectra, as described in section 3.7. The low-energy portion of the spectrum, between about 25% and 50% of E_0, is most sensitive to these rotations, and experience with the coherent bremsstrahlung beam at Mainz [17, 18] and in Hall B indicates that the alignment process would be severely compromised if photon energies below 0.5 E_0 were not measurable. In addition, the high-energy part of the fixed focal plane array can be used as (software) veto in case that more than one electron from a same beam bucket undergo scattering in the radiator with one of them hitting the high-resolution device. In this case the energy balance in the GlueX detector will not match the assumed photon energy detected in the microscope. Photons with energies below the coherent peak do not have to be considered since they would not cause a surplus of longitudinal momentum, which cannot be resolved in a (1C) kinematic fit.

A high energy resolution in the tagger is not deemed necessary for these purposes. A counter width spanning 0.25% of E_0 is considered sufficient in most cases. For operations with an amorphous radiator, these counters would be capable of running a broad-band photon beam with the highest intensities compatible with tagging. Crystal alignment procedures are not carried out at full source intensity, so rate capacity is not a limitation in that application. If a need arose to operate the source in collimated-coherent mode at lower photon energies, for example to obtain increased polarization, then full-intensity operation would always be possible by repositioning the microscope on the focal plane. In this case, the fixed array would be useful in the energy calibration of the movable segment. When used as the primary tagging detectors, the fixed array would be capable of pre-collimated intensities up to 150 MHz/GeV. The initial instrumentation will provide 50% sampling of 60 MeV energy bites below 9 GeV and full coverage of 30 MeV wide counters above 9 GeV photon energy.

5.5 Beam dump optics

Although the full-energy beam leaving the tagger magnet is diverging in both directions, the range of angles is small enough that the beam does not blow up rapidly. For a dump distance of 30 m the r.m.s. beam size is 6.3 mm horizontal (dominated by the 0.08% beam energy spread) and 0.7 mm vertical (combination of vertical spot size and multiple scattering in a 10^{-4} radiation length radiator.)

These values scale approximately linearly with distance from the magnet to the dump, and are not very sensitive either to the quadrupole or to small rotations of the exit edge of the tagger magnet. Thus the beam dump design is quite insensitive to the beam optics, and depends only on the lateral and longitudinal spread of the shower in the absorber.

Chapter 6

The Photon Beamline

6.1 Introduction

The photon beam starts at the crystal mounted in the goniometer and coexists with the electron beam up to the tagger magnet where the two beams are separated in the dipole's field. The photon beam propagates a total of 76 m from the radiator before interacting with the primary collimator where about 85% of the beam is scraped off. The remaining 15% travels 12 m before passing through the GlueX target and on to the photon beam dump. A vacuum beamline is needed between the tagger spectrometer and the GlueX detector to prevent photon losses and the generation of background. The photon beamline consists of the vacuum pipe for the photon beam and the collimation system needed to collimate the beam without generating background in GlueX. The photon beamline is described in the next two sections and then the Monte Carlo simulation is presented which was used to estimate the background generated in GlueX from the photon beam with this design.

6.2 The Photon Beam in the Tagger Hall

The photon beam passes through the tagger magnet's return yoke in a 1" beam pipe welded to the tagger magnet's vacuum chamber. The photon beamline in the tagger hall connects to the end of this pipe and runs to the entrance of the HALL Dcollimator area. The tagger hall photon beamline is shown in Figure 6.1. After the tagger magnet a short piece of 1.5" diameter beamline is inserted up to just in front of the permanent magnet dipole. Here a vacuum isolation valve is inserted to isolate the vacuum in the tagger magnet region from the photon beamline leading to HALL D. The section of beamline between

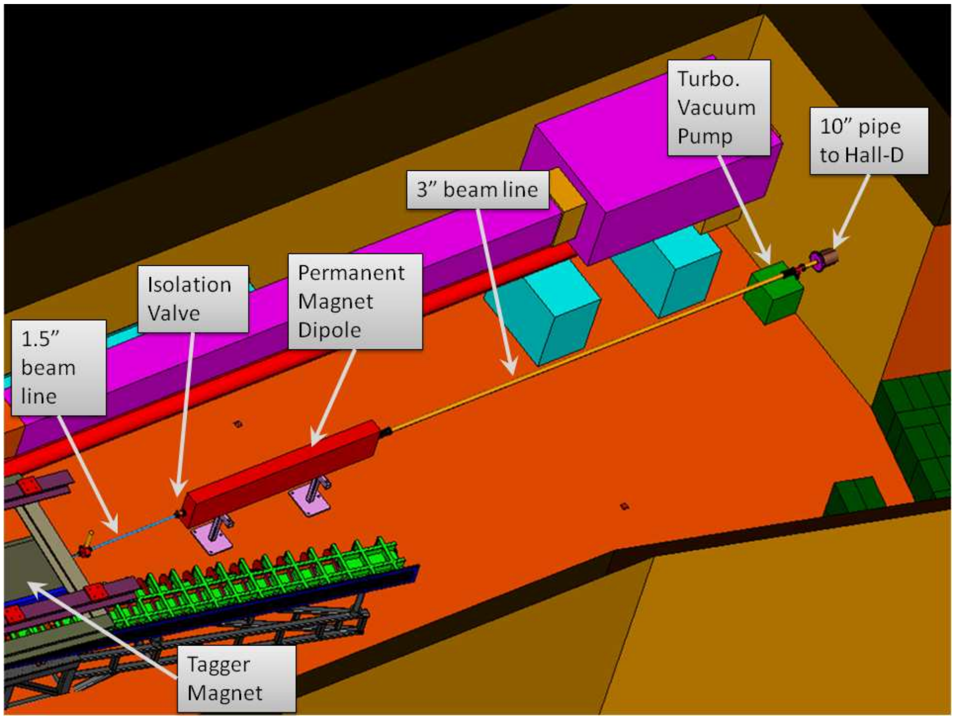

Figure 6.1: The layout of the photon beamline in the tagger hall.

this valve and the collimator area is 63m long. As this beamline has a large surface area and volume it important to be able to isolate this vacuum section from all other sections which minimizes the need for venting and subsequent evacuation . After the isolation valve is a permanent magnet dipole of type FermiLab PDV which has an effective length of 140" and an integrated field strength of 0.822 T·m. This magnet would deflect any charged particles in the photon beam toward the floor making it impossible for them to enter the beam pipe which leads to Hall D. Inside the magnet is a 1.5" by 3.5" stainless steel beampipe. After the dipole magnet a transition is made to 3" beam pipe for the remaining path to the East wall. At the wall there will be a turbomolecular pumping system with about 60 l/s pumping speed and the prevision for attaching a JLAB standard roots blower pumping station. The roots blower has a large pumping speed and will be used for pumpdown. A 10" schedule 40 stainless steel pipe connects the tagger hall to the Hall D cave extension. This 50 m long pipe is specified to be clean and helium leak tight. The pressure in the beamline will be monitored with a pirani vacuum gage and a cold cathode high vacuum gage both mounted near the 250 μm

Kapton (or Aluminum) exit window at the downstream end of the 50 m long pipe.

The vacuum pipe between the halls has enough surface area and volume that the the time needed to evacuate the beamline and the effects of outgassing must be estimated. The 10" beam pipe between the tagger hall and the Hall D cave extension is 50 m long and has a radius of 12.7 cm which results in a surface area of 40 m^2 and a volume of 2,500 l. Given the pumping speed of the turbomolecular pump and the volume of the vacuum chamber the time needed to evacuate the chamber can be evaluated. The pump down time from atmosphere to 1×10^{-5} Torr was estimated to be about 90 minutes and is dominated by the pumping speed in the viscus region. Once the molecular flow region is reached only about 100 seconds are required to reduce the pressure by an order of magnitude.

If an outgassing rate for stainless steel of 10^{-10} Torr $\cdot\, l$/sec per cm^2 of surface area is assumed then the total outgassing rate for the 10" beam pipe is 4×10^{-10} Torr $\cdot\, l$/sec. The resulting ultimate pressures in the beamline at the downstream exit window and at the pumping station are then 1×10^{-6} and 5×10^{-7} Torr respectively. The initial outgassing rate will be much higher but after the system has been under vacuum for a time the vacuum requirement for the photon beamline of 1×10^{-4} Torr will clearly be met.

6.3 The Photon Beam in Hall D

A preliminary drawing of the floor plan to Hall D is shown in Figure 6.2. The photon beam enters the hall through the 10" buried beamline on the left of the figure. The first room the beam enters is referred to as the "collimator cave extension" houses all equipment for the collimation of the photon beam. At the entrance to Hall D proper is a pair spectrometer for beam diagnostics followed by the GlueX detector. The pair spectrometer is descried in detail in the next chapter. On the right of the hall is the photon beam dump.

6.3.1 The Collimator Cave Extension

A 3 μA 12 GeV beam interacting with a 20 μm diamond radiator will produce a beam of about 2.2×10^{10} photons/second for $e_\gamma > 1.2$ MeV. The characteristic opening angle for bremsstrahlung is $m_e/E = 42\mu$rad. After 76 meters of drifting in vacuum the beam has grown to roughly 6.4 mm in diameter. This beam which is a mix of coherent and incoherent bremsstrahlung photons is then strongly collimated to enrich the coherent bremsstrahlung fraction in the beam.

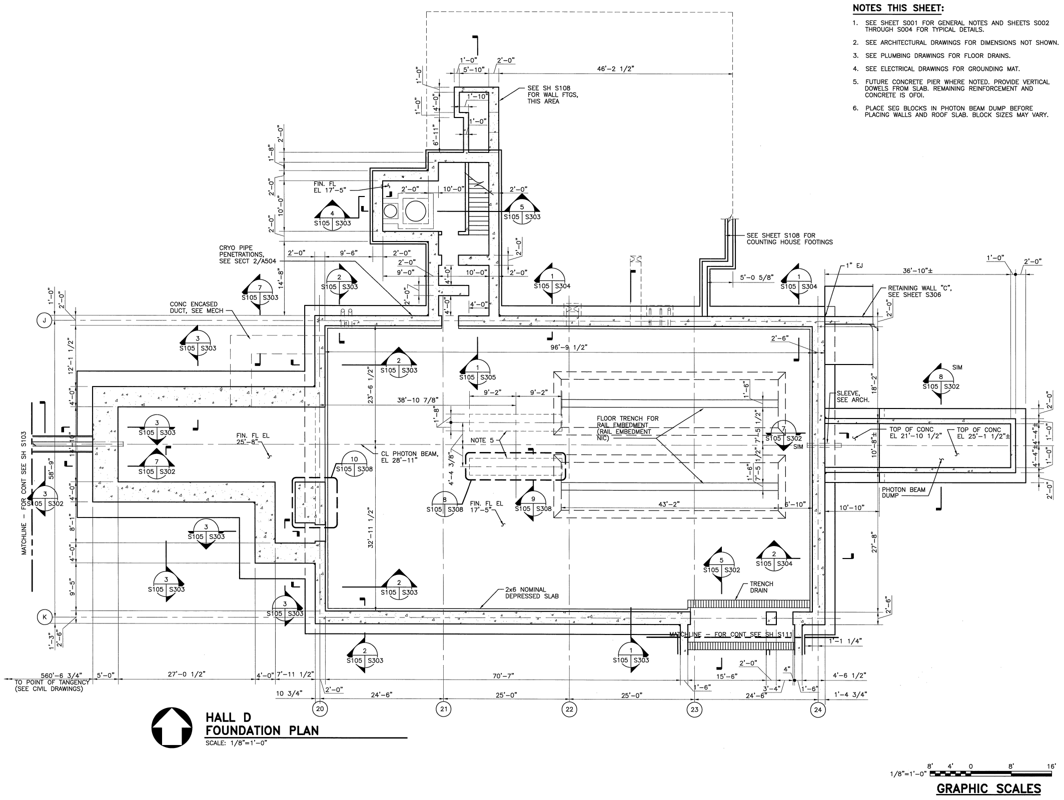

Figure 6.2: A preliminary drawing of the foundation for Hall D.

This collimation reduces the number of photons in the beam from 2.2×10^{10} to 3×10^{9} of which 10^{8} photons have energies in the coherent bremsstrahlung region of 8.4 to 9 GeV. The large number of photons interacting with the collimator has the potential to produce a large background rate in the GlueX detector. They also produce a significant amount of radiation which is a concern for radiation safety.

Due to the radiation safety requirements and the concern for optimal shielding for GlueX it was decided to construct a tunnel at entrance to HALL D into which the entire collimation system is mounted. The collimator cave extension is $14' \, 10"$ (4.5 m) wide $41'$ (12.5 m) long and $8' \, 10"$ (2.7 m) high. $13'$ of concrete and earth above the cave insure that all radiation safety requirements are met.

Figure 6.3 shows the layout of the equipment in the collimator cave extension. The photon beam enters the cave extension from the left through a thin 250 μm Kapton window 8" (203mm) in diameter and immediately interacts

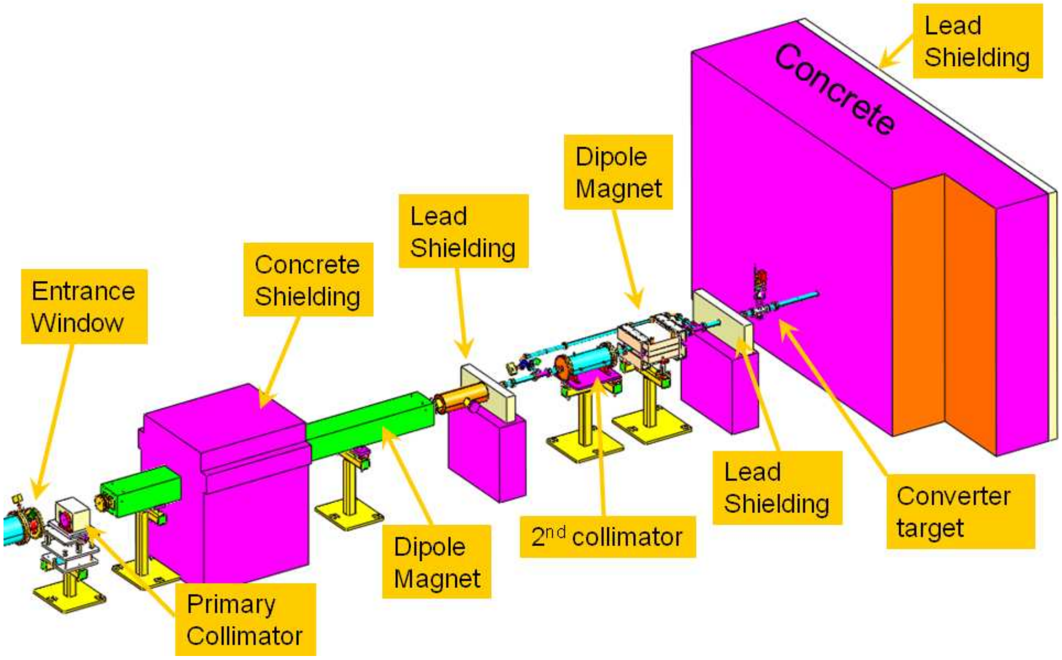

Figure 6.3: The layout of the collimator cave.

with the primary collimator. The primary collimator consists of two main components an active collimator which measures the centroid of the photon beam and a hybrid tungsten lead passive collimator. The active collimator is electrically isolated, has an inner aperture of 5 mm, and is precisely mounted in front of a 3.4 mm hole in the passive collimator. The active collimator is described in detail in section 6.3.2. Its purpose is to measure the position of the centroid of the photon beam with an accuracy of 200 μm. The passive collimator is constructed of 2" thick tungsten plate 10" wide and 8" deep. Two inches from one edge is the 3.4 mm hole which will be used under normal running for the primary collimation. Two inches from the other edge will be a 10 mm hole which can be used if the CEBAF beam quality is too poor for production data running. The tungsten collimator is mounted on an $X-Y$ table so that one can switch between collimator remotely and also adjust the vertical position if necessary. The tungsten collimator is surrounded in 8" of lead for additional shielding.

A large flux of particles are generated in the passive collimator and some lie along the photon beam. A sequence of sweeping magnets with collimation are required to remove the unwanted particles from the photon beam. The energy spectrum of the charged particles generated in the passive collimator extends

Magnet Type	PDV
Magnet Description	Permanent magnet dipole
Physical length	145 IN
Magnetic Length	140 IN
Integrated Strength	0.8220 T m
Magnetic material	type 8 Strontium Ferrite
Pole tip material	1008 steel
Time Stability	ΔB/B < 0.02% /yr
Radiation Resistance	ΔB/B < 0.02% for 1 GigaRad

Table 6.1: Summary of the main features of FermiLab's PDV dipole magnet.

to the full 12 GeV CEBAF energy. A strong magnetic field is needed to sweep these particles from the beam. The two of the FermiLab PDV permanent magnet dipoles are available within the HALL D group at Jefferson Laboratory. Three of these magnets were obtained from FermiLab when the decision was made to insert one of these magnets in the photon beamline in the tagger hall. The specifications for the PDV magnet (Shown in Table 6.1) are well suited for use as the first sweeping magnet after the primary collimator. Results of a Monte Carlo study shown in Figure 6.4 show that particle under 7.5 GeV strike the yoke of the magnet. The higher energy particles are swept out to distance of about 7.5 cm from the beam 70 cm after the end of the magnet. A 4 inch thick lead wall is positioned 67 cm after the end of the magnet to absorb these particles. The advantage of using a permanent magnet is that no power supply is required and there are no parts to fail. As the field is well suited to our applications and the magnet is available we decided to use this magnet as our primary sweeping magnet.

Monte Carlo studies indicated that if the photon beam is allowed to propagate through air between the active collimator and the GlueX detector a large amount of electromagnetic background will be generated. Therefore the photon beam will re-enter vacuum at the start of the PDV dipole magnet. Here a 1 inch diameter 150 μm thick Kapton window is foreseen. The vacuum system will be pumped by a 60 l/s turbomolecular pumping station located outside the collimator cave. The Monte Carlo simulations also indicated that the background produced in the short air section between the entrance to the collimator cave area and the entrance of the first sweeping magnet was small.

A second collimator is located after the lead shielding wall of the first collimator. This collimator is made of stainless steel and is 20" long and 8" in

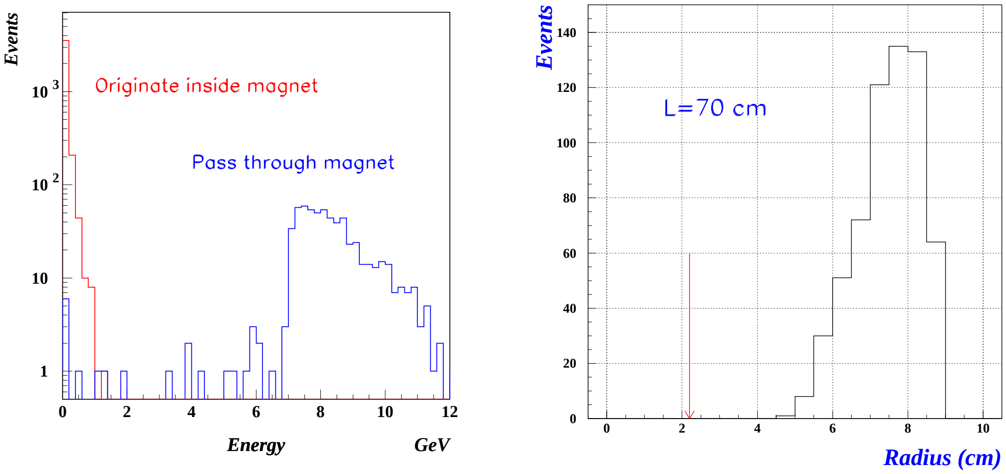

Figure 6.4: The left panel shows the energy distribution of particles passing through the first sweeping magnet. The right panel histograms the number of particles as a function of distance from the beamline 70 cm after the magnet.

diameter. A 1 cm hole is bored along the axis of the collimator and it is design so the the effective aperture can be adjusted to 6, 8, or 10 mm by inserting stainless steel tubes in the collimator aperture. The purpose of this collimator is to scrape off photons which were produced by low angle scattering on the bore of the primary collimator. A second sweeping magnet is mounted directly after the second collimator. As the photons which interact with the second collimator have a much lower energy a much smaller magnet can be used here. The magnet which we selected was the type DW which was originally designed for the Jefferson Laboratory's free electron laser program, but is no longer used

Maximum Field	0.248 T
Magnetic Length	0.408 m
Maximum Current	200 A
Maximum Voltage	11 V

Table 6.2: Summary of the main features of Jefferson Laboratory DW dipole magnet.

for that application. The magnet has the properties shown in Table 6.2 and was acquired on permanent loan from the Navy Department of Research. A second lead shielding wall is placed after this magnet. At the downstream end of the collimator cave a wall of 1.4 m of concrete and 2 inches of lead shield Hall D from particles large distances from the beam in the cave area.

The initial equipment installation will be performed with the aid of a fork-lift. However, once the concrete wall is in location this is no longer possible. Therefore three I-beams will be mounted in the roof and equipped with hoists for use in mounting and repair after the initial installation. Entry to the collimator cave will be through the labyrinth shown in Figure 6.1. A locked gate under the control of the radiation protection division at the entry to the labyrinth will prevent unauthorized entry.

6.3.2 The Active Collimator

6.3.3 Beam Transport to GlueX and the photon beam dump

Once the photon beam leaves the collimator cave it enters Hall D where it is roughly 10 m away from the GlueX target. The upstream section of the photon beamline in Hall D is shown in Figure 6.5. The first section of beamline in Hall D is the pair spectrometer which will be described in detail in the next chapter. The photon beam continues in vacuum from the pair spectrometer up to the target. The detail of the interface between the photon beamline and the liquid hydrogen target will be resolved once the design of the target has begun. A solution with no windows would be preferred but the final design will be fixed by safety conditions. An option of placing a small additional collimator directly upstream of the target is being investigated but no decision has yet to be made. In the present design the GlueX detector has been moved 2 m downstream to give space between the pair spectrometer and the solenoid for maintenance of the target and central drift chamber if needed. In Figure 6.5 the target and start counter have been pulled back for maintenance. After the GlueX detector the beam will enter either another vacuum beamline or a helium filled volume which runs from the detector to the photon beam dump. The total power in the beam after final collimation is only 1-2 W so no cooling is required for the dump. The design is simply a set of iron blocks set into the East wall of Hall D.

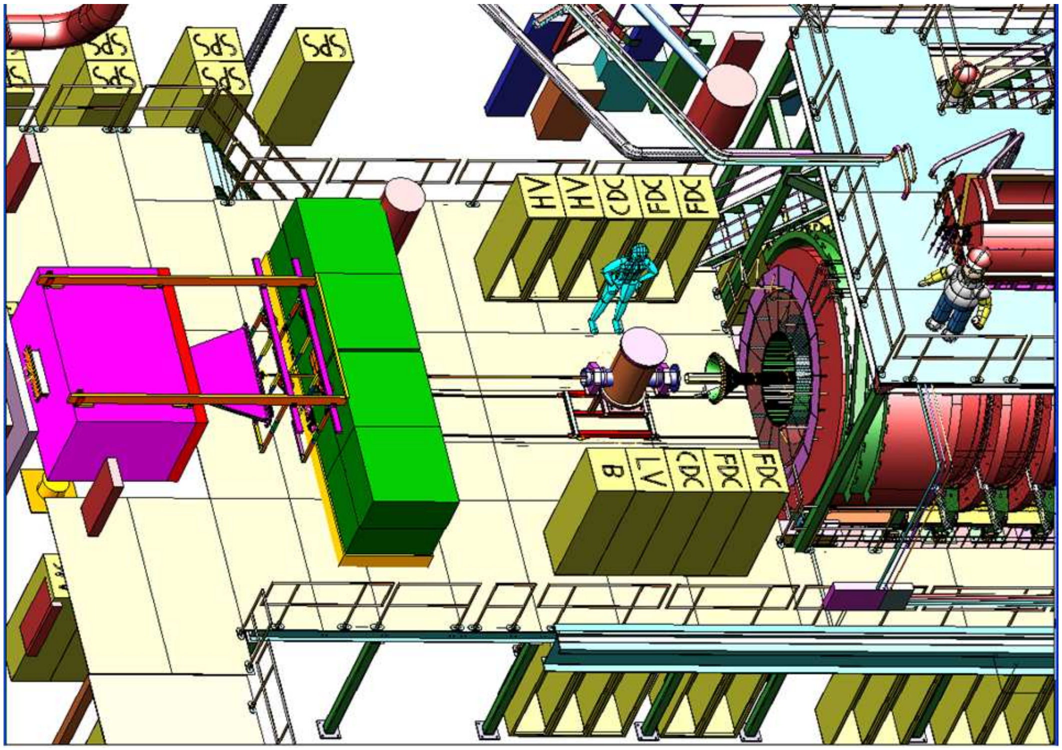

Figure 6.5: The 3-D model of the upstream end of Hall D is shown. On the left the photon beam enters Hall D from the collimator cave and on the right is the solenoid magnet for the GlueX experiment

6.4 Collimator Cave and Pair Spectrometer Background

In order to enhance the fraction of linearly polarized photons in the beam, bremstrahlung photons produced on a diamond radiator have to pass through a 3.4 mm diameter collimator situated in the collimator cave about 20 m upstream from the GlueX detector. The collimator reduces the total flux of incident photons by about factor of seven, from 22×10^9 γ/sec to about 3×10^9 γ/sec in the photon energy range of 1.2 MeV $< E_\gamma <$ 12 GeV. Interactions of photons with the collimator result in background particles produced inside the collimator cave. To prevent most of this background from entering to the detector region, we instrument shielding components inside the collimator cave and directly in front of the GlueX detector. The design of the shielding components with regard to positions, sizes, and materials has been optimized by studying sources of different types of background produced inside the collimator cave using a detailed GEANT 3.21 [19] detector simulation. Fluxes of background particles, γ, $e^{\pm}$, $\mu^{\pm}$, and neutrons, have been calculated for various collimator cave component layouts at planes placed perpendicular to the photon beamline at different z-positions along the beam. To simulate hadronic interactions of electro-magnetic particles we use the Gelhad package [20] which has been integrated into the GEANT simulation. The flux of background neutrons has been independently checked by a custom version of GEANT developed by the JLab radiation safety group that includes a more sophisticated model of photo-nucleus interactions [21, 22]. The most recent collimator cave geometry implemented into the GEANT simulation is presented in Fig. 6.6. Layouts of the following main components have been studied in detail:

- Primary and secondary collimator
- Sweeping magnets
- Vacuum chamber
- Concrete blocks and a lead wall

Rates of background particles in front of the GlueX detector are presented in Fig. 6.7. The background is dominated by secondary photons that originate from the primary collimator and travel inside the beam pipe. These photons are in the first bin of a histogram on the upper plot of Fig. 6.7. The mean energy of these photons is about 400 MeV and the rate of these photons corresponds to $2 \cdot 10^6$ photons per second. They constitute about 0.1% of the total number of the beam photons. The distribution of background photons in the x-y plane is shown on the left plot of Fig. 6.8. Most background photons situated in the beam pipe have a relatively small polar angle with respect to the beam direction, $\sin\theta < 8 \cdot 10^{-4}$. This angle is mainly defined by the geometrical sizes of the primary and secondary collimators and a relative distance between them. The major fraction of these photons that do not interact with the detector material is expected to remain within a 2 cm radial distance from the beamline at the end of the detector. Background outside the beam pipe consists of low-energy photons with a mean energy of about 4.8 MeV. At a relatively large radial distance from the beamline, larger than 1 m, the background is dominated by photons that punch-through the lead wall of the collimator cave. At radial distances close to the beamline, the main contribution comes from photons that originate from secondary interactions of the beam-pipe background photons with the beam pipe wall in the region close to the GlueX detector. The z-coordinate of the origin of photons is shown on the right plot of Fig. 6.8.

The rate of $e^{\pm}$ background is shown on the middle plot of Fig. 6.7. Background $e^{\pm}$ originate mainly from secondary interactions on the beam pipe wall after the pair spectrometer's SEG shielding blocks and, as a result, have a relatively small mean energy of about 37 MeV. Background rates for $\mu^{\pm}$ and neutrons are shown in the bottom plot of Fig. 6.7. The main source of the muon background is the primary collimator. The average energy of the muons is 1.8 GeV. Background neutrons are mainly produced inside the concrete wall of the collimator cave and in the primary collimator. The fluxes of $\mu^{\pm}$ and neutrons are small.

We estimate the influence of the collimator cave background particles on the GlueX detector. The rates in different GlueX sub-detectors induced by the collimator cave background particles are compared with that produced by ordinary electromagnetic interactions in the GlueX detector. As an example, the FDC and FCAL rates are presented in Fig. 6.9. As can be seen from these plots the rates produced by the collimator cave background particles are more than two orders of magnitude smaller than the rates from electromagnetic interactions. As a consequence, the collimator cave background has no impact on the particle reconstruction in the GlueX detector and on the Level-1 trigger performance. A detailed description of the Level-1 trigger simulation can be found in [23].

We subsequently estimate background in the GlueX detector induced by the pair spectrometer's converter. In this studies, we eliminate background originating inside the collimator cave. The pair spectrometer geometry implemented into the GEANT simulation is presented in Fig.6.2. It consists of the following main components: 0.89 mm (10^{-3}) radiation length thick aluminum converter, dipole magnet, vacuum chamber, and hodoscope counters. $e^{+}e^{-}$ pairs produced in the spectrometer are dumped into a lead band made of a standard-size bricks ($5 \times 10 \times 20$ cm^3). The size of the band corresponds to $220 \times 30 \times 10$ cm^3. This band also reduces electromagnetic background that originates on the edges of the magnet aperture. Background is further reduced by four SEG blocks which are maid mainly of iron, and are positioned after the lead band. This blocks are used in JLab and have a typical size of $132 \times 132 \times 66$ cm^3. The SEG blocks also provide additional suppression of remaining background from the collimator cave.

Occupancy distributions of photons and $e^{\pm}$ after the vacuum chamber are shown in Fig. 6.10. As expected, most background photons and $e^{\pm}$ are produced on the edges of the magnet aperture. They can be seen as two distinct spots on x-y distribution around $x = \pm 100$ cm. A narrow horizontal band in the occupancy distribution of $e^{\pm}$ corresponds to the signal pairs originating from the converter. The rates of background photons and $e^{\pm}$ after the shielding SEG blocks (placed about 4 meters upstream from the GlueX detector) are shown in Fig. 6.11. The rate of background photons produced by the converter inside the beam pipe constitutes about 6.5 kHz which is very small compared with the rate of beam photons and the rate of the collimator cave beam related background. We found no background directly behind the SEG blocks. Soft background photons, with an average energy of about 6 MeV, observed at a large radial distance from the beamline are produced on the edges of the magnet aperture at a relatively large polar angle; their flux is small in the detector region. We found that all types of backgrounds produced by the pair spectrometer are negligibly small. It is worth mentioning that background originating inside the pair spectrometer magnet can be further reduced by installing a tapped lead collimator in to the magnet aperture. Specifically, the collimator will allow one to decrease the rate of random coincidences between electron and positron scintillator counters required by the pair spectrometer trigger. This option has been studied in detail.

Details on the simulation of the collimator cave and pair spectrometer background are described in [24].

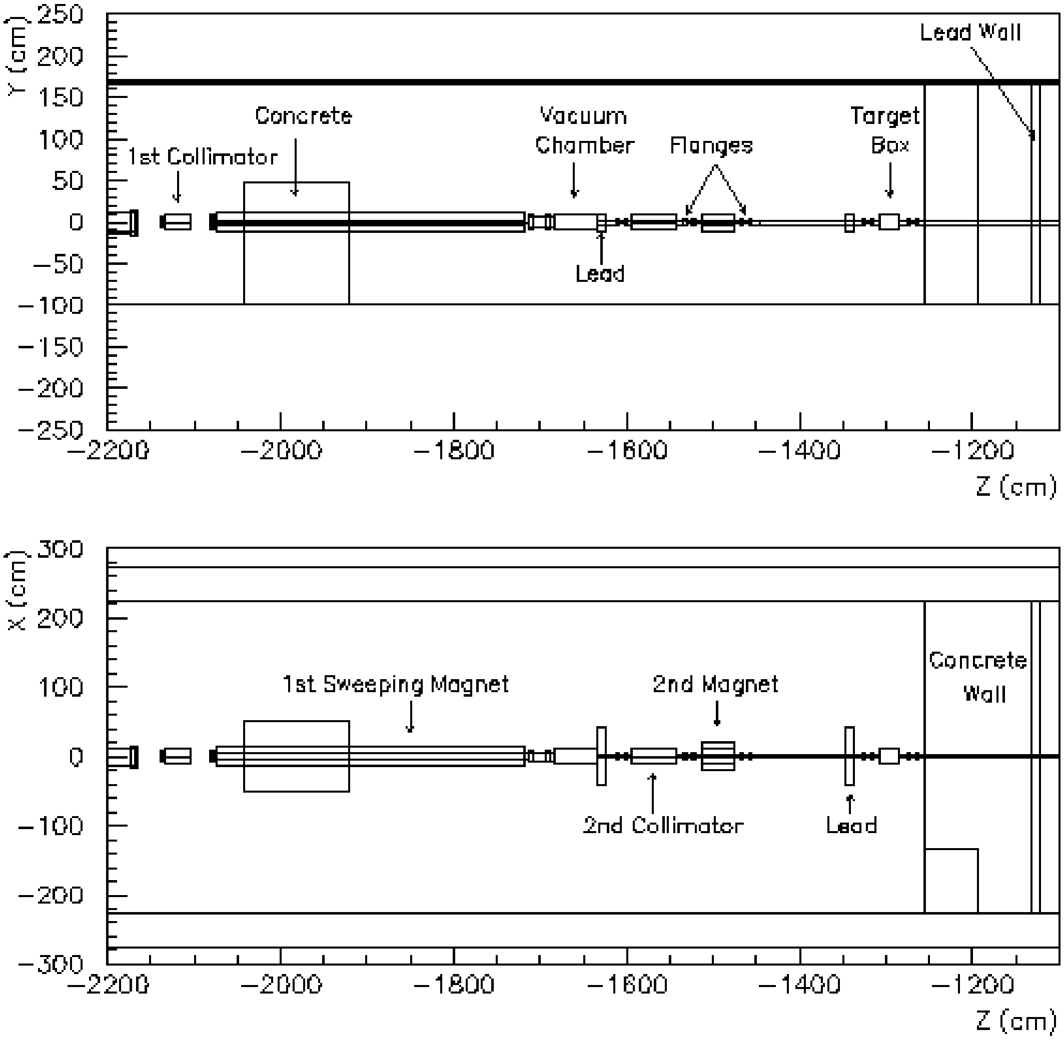

Figure 6.6: Collimator cave geometry implemented into GEANT simulation. The top plot corresponds to the side-view and the bottom plot corresponds to the top-view.

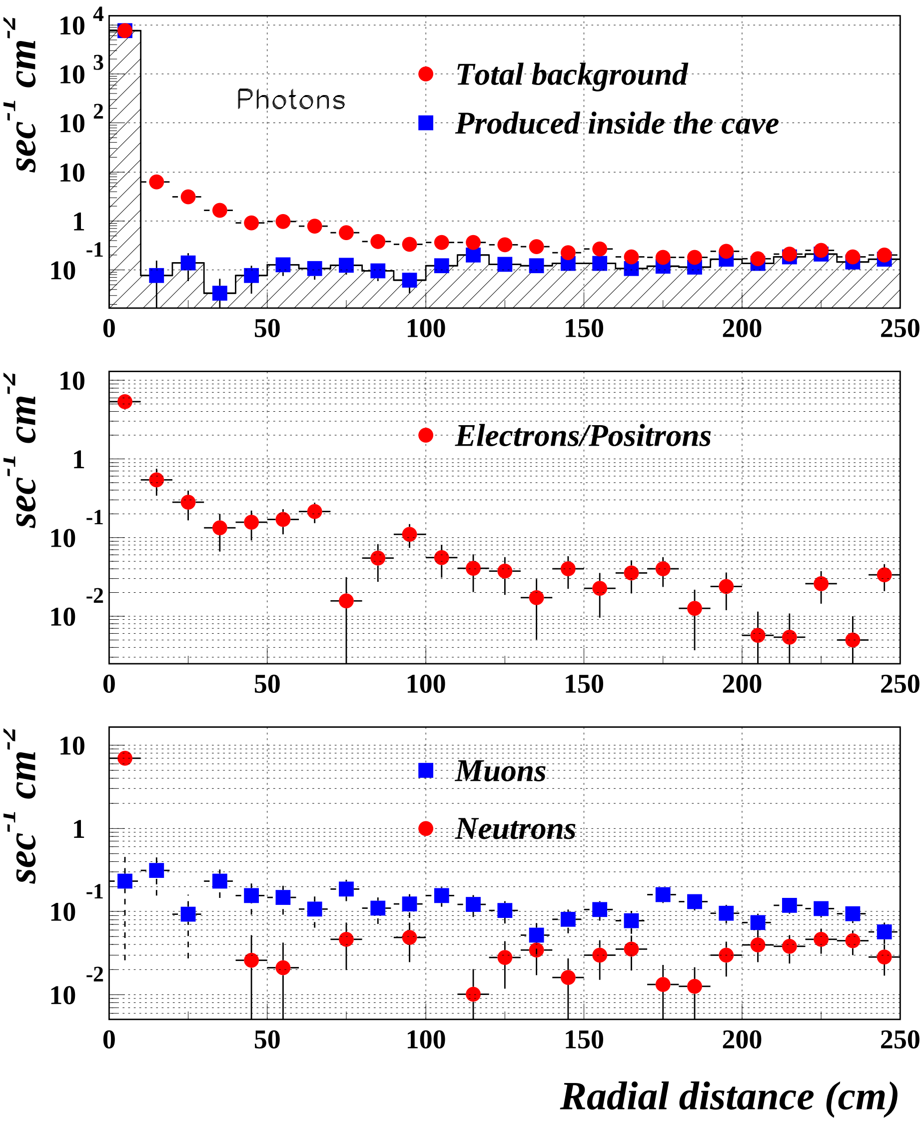

Figure 6.7: Flux of background particles in front of the GlueX detector as a function of the radial distance from a beamline. The top plot corresponds to background photons. The hatched histogram denotes photons produced inside the collimator cave, i.e., about 10 m upstream from the GlueX detector. The middle plot corresponds to background $e^{\pm}$ and the bottom corresponds to $\mu^{\pm}$ (boxes) and neutron (circles) backgrounds.

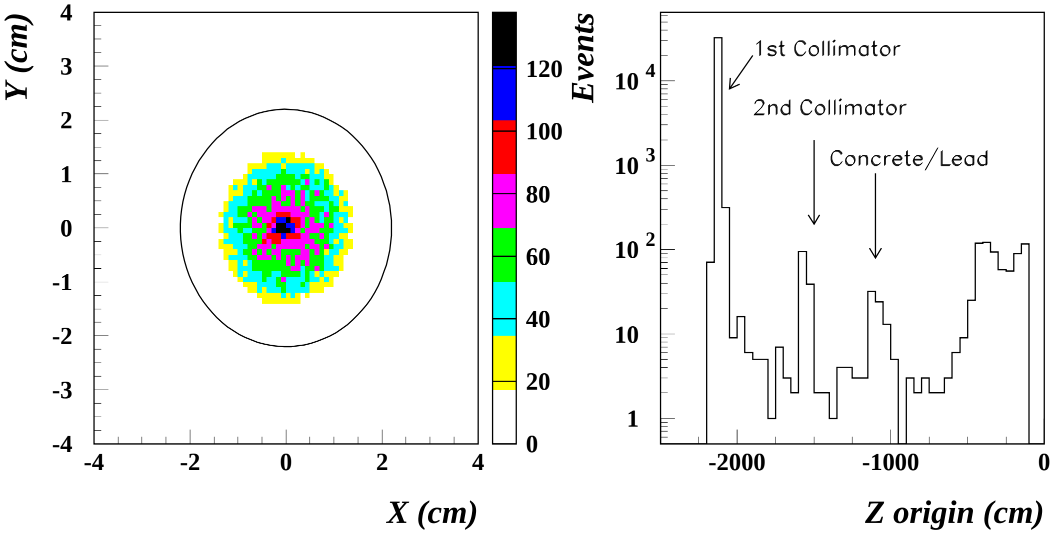

Figure 6.8: X versus Y distribution of background photons inside the beam pipe (left). The circle represents the beam pipe. Z coordinate of the photon's origin (right).

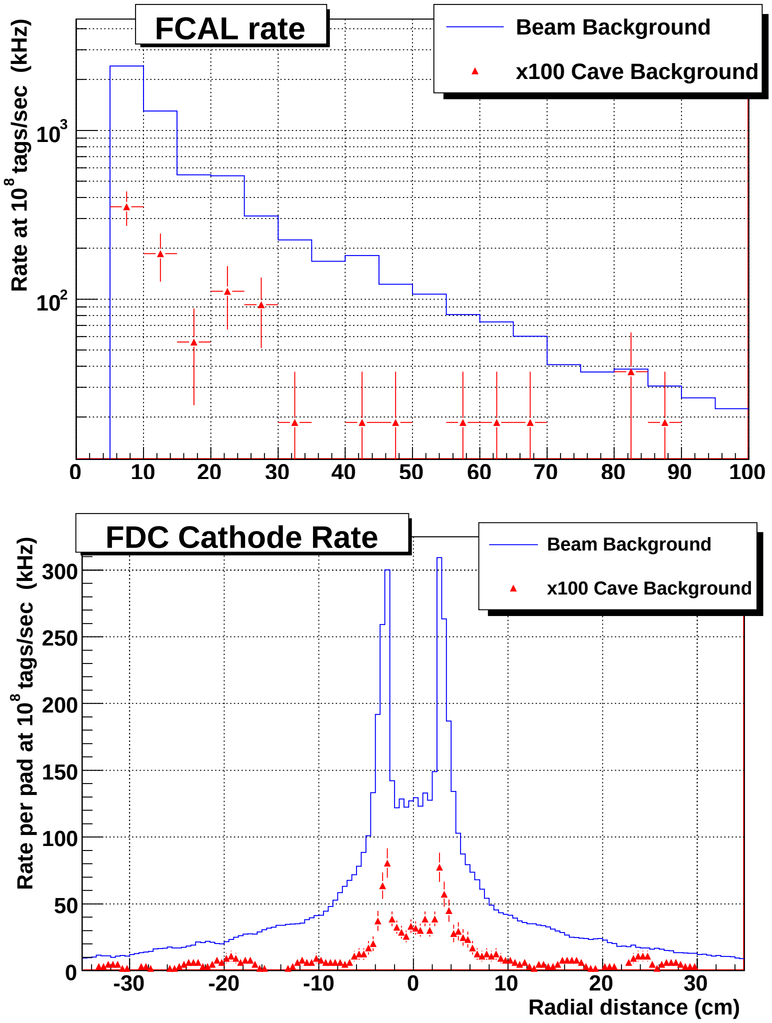

Figure 6.9: FCAL and FDC Cathode rates as a function of the radial distance from the beamline. Solid curves represent electromagnetic background produced by the photon beam. Polymarkers represent the rates scaled up by a factor of 100 induced by the collimator cave background.

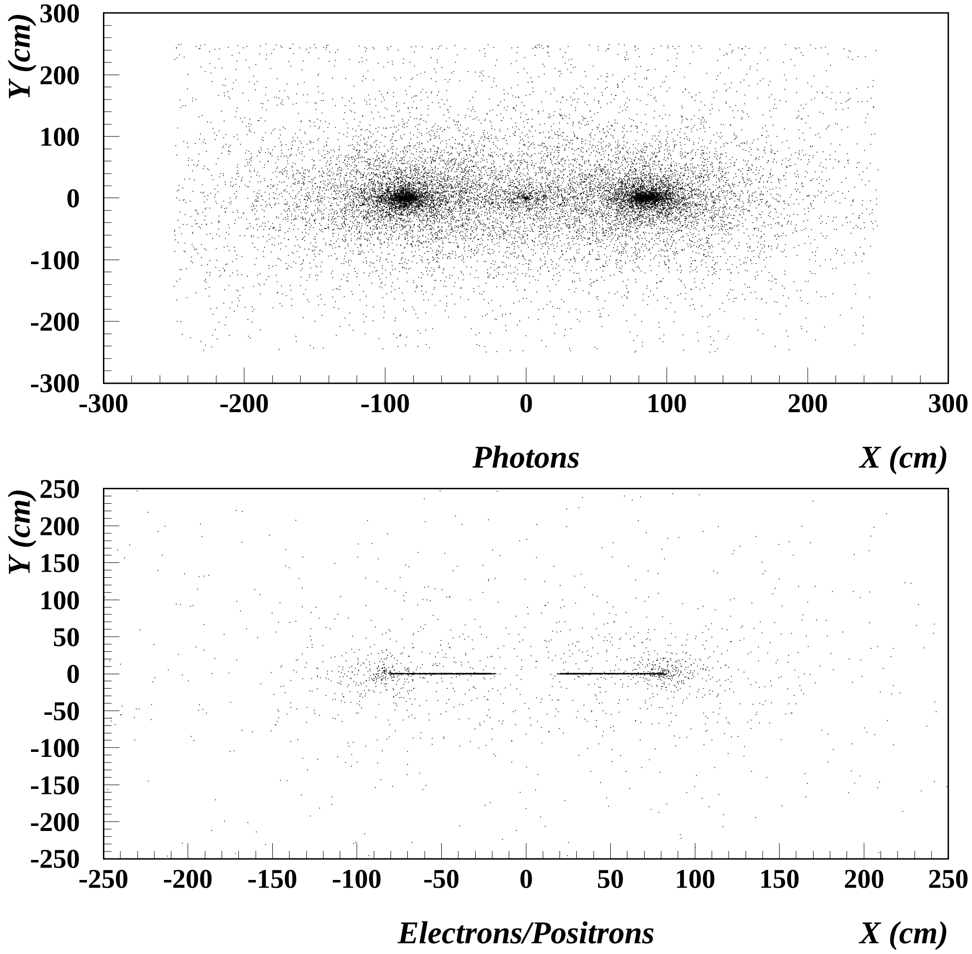

Figure 6.10: X versus Y distributions of photons (top) and $e^{\pm}$ (bottom) after the pair spectrometer's vacuum chamber.

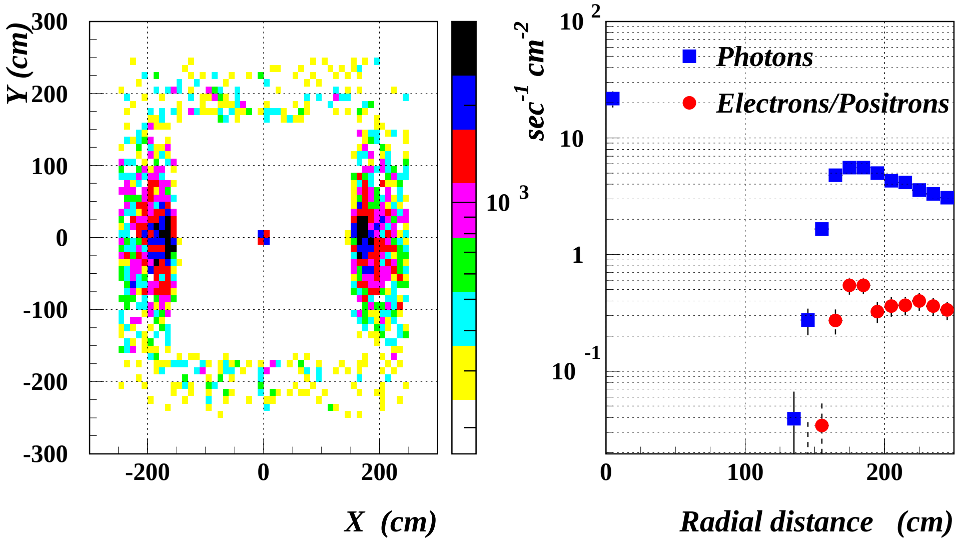

Figure 6.11: Rate of background photons after the shielding SEG blocks (left). The rate is given in Hz per 10 × 10 cm^2. The right plot represents the rate of photons (boxes) and $e^{\pm}$ (circles) as a function of the radial distance from the beamline.

Chapter 7

Polarimetry and instrumentation

7.1 Introduction

The most important diagnostics for the photon beam are the count rates in the tagger's fixed hodoscope array and the microscope. By studying the electrons which underwent the bremsstrahlung interaction, one can learn a wealth of information about the photon beam with the tagging spectrometer. Careful measurement of the electron energy spectrum gives precisely the photon energy spectrum of the photon beam in front of the collimators $\mathrm{I}_\gamma^{\mathrm{uncoll}}(\mathrm{E})$. As the shape of the incoherent bremsstrahlung spectrum is precisely known, if the photon energy spectrum is measure far above and below the coherent edge the incoherent bremsstrahlung contribution can be subtracted. The polarization of the photon beam can then be calculated by analyzing the coherent bremsstrahlung spectral shape. The polarization of the final photon beam is estimated by assuming the influence of the collimation system is well understood. Details of this analysis are presented in the next section. This very powerful tool has the advantage that the count rates in the hodoscope are very large so $\mathrm{I}_\gamma^{\mathrm{uncoll}}(\mathrm{E})$ can be continuously monitored.

The spectral shape analysis technique does have several limitations. The photons forming the beam to Hall-D are only about 15% of the tagged photons because of the collimation. In order to predict the polarization of the photon beam after the collimators one has to assume that the collimators are correctly aligned. The absolute luminosity will depend strongly on the exact details of the collimation. Thus an accurate measurement of the energy dependent luminosity requires an exact knowledge of the target thickness and the photon energy spectrum after collimation $I_\gamma^{coll}(E)$. Therefore a direct measurement of the photon beam energy spectrum, luminosity, and polarization after all collimation is needed. All these quantities can be precisely determined if the photon flux function $I_\gamma^{coll}(E)$, which is the number of photons in the beam as a function of the photon's energy, is precisely measured after the last collimator. $I_\gamma^{coll}(E)$ combined with the target thickness gives directly $\mathcal{L}(E)$. A spectral shape analysis can be performed similar to the one planned for the tagger to extract the beam's linear polarization for the collimated beam. In order to have a precision measurement of the characteristics of the photon beam, it is necessary to base the measurement on a well understood cross section. It is proposed to use pair production which is a well understood QED process as the basis for the luminosity measurement and polarization determination. The proposed pair production spectrometer consists of a thin foil placed in the photon beam to generate electron/positron pairs through pair production. A magnetic spectrometer then measures the momentum of the electrons and positrons in coincidence. The photon energy is then simple the sum of the electron and positron energies. The pair production spectrometer is described in detail in section 7.3. It should be pointed out that this pair production spectrometer can never replace the tagger. Any photon interacting in the converter foil is lost to the photon beam. The tagger is needed to measure the energy of the photons which interact in the GlueX target. The pair spectrometer can however accurately measure the average properties of the photon beam.

7.2 Polarization prediction using spectral shape analysis

The majority of bremsstrahlung photons produced in the radiator are absorbed in the collimator system. If the radiator and collimator system are well aligned, the photon spectrum behind the collimators is dominated by the coherent peak. The photon beam energy spectrum and polarization can be determined by using the intensity spectra from the tagger.

7.3 Pair Spectrometer

The layout of the pair spectrometer is shown in Figure 7.1. The photon beam is uniformly sampled with a thin converter foil positioned after the last collimator upstream of Figure 7.1. The electrons and positrons produced in the converter are swept away from the photon beam in a strong dipole field and

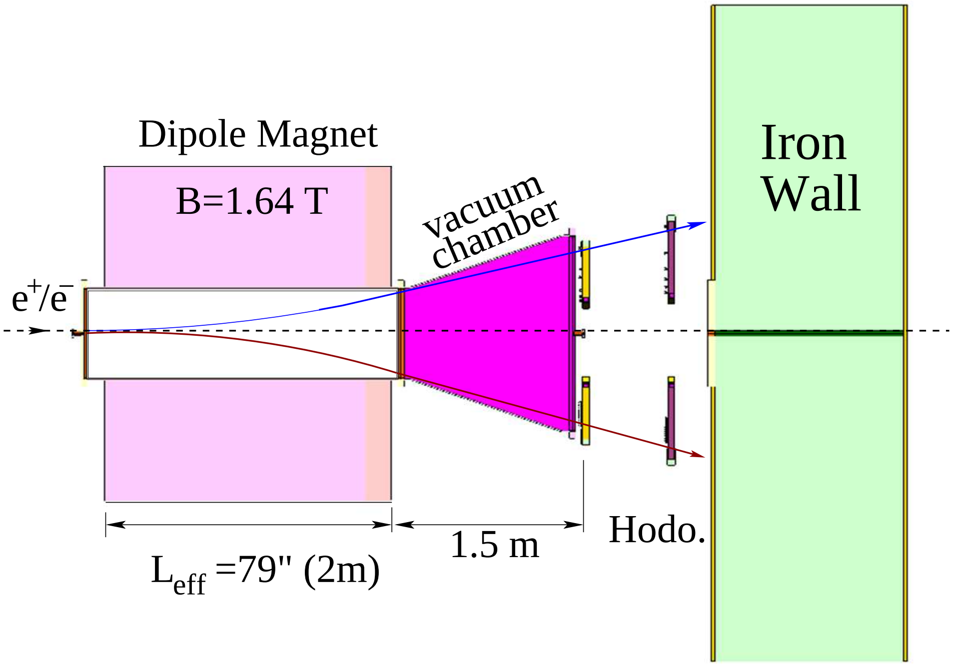

Figure 7.1: Layout of the pair spectrometer. On the left is a thin 10^{-3} radiation length converter followed by a strong spectrometer magnet. The vacuum chamber extends beyond the end of the magnet to the front of the first hodoscope plane. The first scintillator hodoscope is placed 1.5 m beyond the end of the magnet. A second hodoscope plane is placed 80 cm behind the first plane and is used for triggering.

are subsequently detected in scintillator hodoscopes placed 1.5 and 2.3 m after the magnet. It is planned to use a converter which is about 1×10^{-3} radiation lengths thick. This is thin enough to have minimal impact on the photon beam but the pair production cross section is sufficiently large to still give a good coincidence rate in the hodoscopes. Studies of the rate and background will be presented below after the spectrometer description. The converter foil will be placed about 0.5 m in front of the spectrometer dipole magnet. It is planned to have foils of several thicknesses mounted on a target holder and the ability to completely remove all foils for background studies. The beamline is being constructed to allow the converter to also be placed 2.5 m in front of the dipole magnet instead of 0.5 m. This allows additional diagnostic devices to be inserted between the converter and the magnet in a future upgrade.

The dipole magnet for the pair spectrometer should have as large an integrated magnetic field ($\int \mathrm{B}\cdot d\ell$) as possible. The larger the integrated magnetic field the more dispersed the electrons and positrons will be on the hodoscope plane, and the better the momentum resolution. The magnet's pole tip needs to be wide enough to let the particles with the lowest momentum which one wants to measure pass through without striking the aperture of the magnet. In order to extract the beam polarization from the the photon flux function $\mathrm{I}_{\gamma}^{\mathrm{coll}}(\mathrm{E})$, the flux function must be measured above and below the coherent bremsstrahlung peak. This implies that the pair spectrometer must measure $\mathrm{I}_{\gamma}^{\mathrm{coll}}(\mathrm{E})$ between E_{γ} of 6 and 12 GeV. The pair spectrometer scintillator hodoscopes will measure electron momenta between 3 and 4 GeV/c and positron momenta between 3.3 and 8.3 GeV/c, thus covering E_{γ} from 6.3 to 12.3 GeV.

The magnet's vertical gap must be large enough to accommodate the vertical spread of the scattered positrons and electrons. The angular divergence of the electrons and positrons produced in pair production is typically $\mathrm{m_e/E} = 42 - 85\mu\mathrm{rad}$ The distance from the converter to the detector plane is about 4 m, so the vertical position spread on the detector plane is about 0.2 to 0.5 mm. Multiple Coulomb scattering dispersion, assuming a converter thickness 10^{-3} X_o, is $55 - 145\mu rad$ which translates to 0.2 to 0.6 mm. Finally the photon beam vertical spot size at the converter is about 4 mm with a sigma of about 1mm. The photon beam spot size clearly dominates the vertical emittance of the $\mathrm{e}^+/\mathrm{e}^-$ pairs. If the vacuum chamber inside the dipole magnet has a height of 30 mm then the $\mathrm{e}^+/\mathrm{e}^-$ pairs will have more than 10σ clearance.

A search for an available magnet which fulfills all the above requirements has been performed and Brookhaven National Laboratory's 30D72 magnet was selected as the best candidate. This magnet has a nominal pole width of 30" (762 mm) and a nominal effective length of 72" (1.83 m). It has a gap of 6" (152 mm) and a maximum field of 2 T. The most important parameters of this magnet are summarized in Table 7.1

The only characteristic of this magnet which is not optimal for this purpose is the magnet's gap. However if 1.5" plates are added to the poles then the gap will be reduced to 3" (76 mm). The vacuum chamber inside the magnet gap needs to have a 3/4" wall thickness which would result in a 1.5" (38) mm gap for the $\mathrm{e}^+/\mathrm{e}^-$ pairs. Reducing the gap by a factor of 2 will also reduce the power consumption by a factor of 4, saving a great deal of power and reducing the water cooling requirements to below what is already foreseen for the pair spectrometer in the Hall-D civil design. It is planned to operate the dipole magnet at about 1.64 Tesla which is well below the 2 T maximum field of the magnet. At the lower field the effect of saturation on the magnetic field should be small. If the magnet is operated at 1.64 Tesla, electrons and

Maximum Field	20.0 KG
Voltage	150 V
Current	2500 Amps
Mean Effective Length (Approx)	79.0 IN
Gap Width	30 IN
Gap Height	6 IN
Gross Weight	64 TONS
Water Consumption	34 GPM
ΔP	160 PSI
ΔT	75° F
Resistance	0.600 Ω

Table 7.1: Summary of the main features of the Brookhaven National Laboratory's 30D72 magnet.

positrons with a momentum of 3.0 GeV/c have a horizontal displacement at the end of the magnet of 28 cm, thus the gap width of 30" (76.2 cm) is sufficient. Additionally, there is enough extra room in the pole gap to add collimation along the outside envelope of the 3 GeV/c trajectories in order to scrape off lower momentum particles. These particles could otherwise cause accidental coincidences in the hodoscopes.

The vacuum chamber downstream of the magnet is limited in length to about 1.5 m by space requirements necessary for equipment in the GlueX detector. The driving factor is the requirement to have enough space between the pair spectrometer and GlueX to shift the target and CDC upstream for maintenance. Therefore it was decided to place the hodoscope detectors 1.5 m after the magnet. Given the magnet's characteristics, the chamber needs to be 1.6 m wide at the downstream end. One necessary condition on the spectrometer design is that 12 GeV/c electrons or positrons generated in the converter must be able to pass through the exit window at the end of the vacuum chamber and strike a shielding wall. This protects GlueX from unnecessary background. With this design 12 GeV/c electrons or positrons will exit the vacuum chamber 18 cm from the photon beam axis leaving sufficient space for a flange to couple to the photon beamline and the exit window mount. The vacuum chamber is constructed of non-magnetic material (aluminum or stainless steel).

The scintillator hodoscope detectors are shown on the right in Figure 7.1. The Fine Spacing Forward (FSF) hodoscope (positron arm) and Wide Spac-

Counter Number	Minimum Momentum	Maximum Momentum	Momentum Uncertainty	Distance to beamline	Counter width
	GeV/c	GeV/c	MeV	m	mm
1	3.0000	3.0417	12.0281	0.7519	11.1
2	3.0417	3.0833	12.0281	0.7408	10.8
3	3.0833	3.1250	12.0281	0.7300	10.4
4	3.1250	3.1667	12.0281	0.7195	10.1
5	3.1667	3.2083	12.0281	0.7094	9.9
6	3.2083	3.2500	12.0281	0.6995	9.6
7	3.2500	3.2917	12.0281	0.6900	9.3
8	3.2917	3.3333	12.0281	0.6807	9.1
9	3.3333	3.3750	12.0281	0.6716	8.8
10	3.3750	3.4167	12.0281	0.6628	8.6
11	3.4167	3.4583	12.0281	0.6542	8.3
12	3.4583	3.5000	12.0281	0.6459	8.1
13	3.5000	3.5417	12.0281	0.6377	7.9
14	3.5417	3.5833	12.0281	0.6298	7.7
15	3.5833	3.6250	12.0281	0.6221	7.5
16	3.6250	3.6667	12.0281	0.6146	7.3
17	3.6667	3.7083	12.0281	0.6072	7.2
18	3.7083	3.7500	12.0281	0.6000	7.0
19	3.7500	3.7917	12.0281	0.5931	6.8
20	3.7917	3.8333	12.0281	0.5862	6.7
21	3.8333	3.8750	12.0281	0.5795	6.5
22	3.8750	3.9167	12.0281	0.5730	6.4
23	3.9167	3.9583	12.0281	0.5667	6.2
24	3.9583	4.0000	12.0281	0.5604	6.1

Table 7.2: Summary of the design of the fine spaced forward (FSF) hodoscope. Trajectories for positrons generated on the beam axis with the given momentum range for each counter were calculated. This momentum range corresponds to 1GeV/c/24 = 41.67 MeV/c for each counter and would result in a uniform uncertainty in the momentum of $41.67/\sqrt{12}$=12.03 MeV/c in the absence of effects from the beam spot size, multiple scattering, and the production opening angle. The distance from the beam axis to the counter and the counter width is calculated from these trajectories.

ing Forward (WSF) hodoscope (electron arm) are used for the energy determination while the Fine Spacing Backward hodoscope (FSB) and Wide Spacing Backward hodoscopes (WSB) are used for triggering purposes. On the positron side the FSF hodoscope will consist of 24 close packed scintillator counters measuring momenta between 3 and 4 GeV/c in equally spaced momentum bins. On the electron side the WSF is a sequence of 6 narrow scintillators placed at intervals corresponding to a 1 GeV/c spacing and covering the range 3.25 to 8.25 GeV/c. A coincidence between one counter in the FSF and one in the WSF corresponds to one photon energy bin. This arrangement gives $6 \times 24 = 144$ photon momentum bins equally spaced in energy between 12.25 and 6.25 GeV. This spectrometer design provides uniform acceptance over the energy range from 6.25 GeV to 12.25 GeV using a minimum number of counters and readout channels.

The number of counters in the FSF fixes the number of photon energy bins per GeV. The number of energy bins must be large enough so that the bin size does not limit the error on the polarization extraction using the spectral analysis technique. The Yerevan group has studied the effect of binning and finds that with 24 bins the error on the fit of the peak in the coherent bremsstrahlung spectrum is less than 2% which leads to a contribution to the estimated polarization uncertainty less than 1%. The FSF is designed to consist of 24 scintillator counters each spanning 1 GeV/c/24 = 41.67 MeV/c. The nominal momentum uncertainty for each counter is then $41.67/\sqrt{12}$=12.03 MeV/c, but effects from the beam spot size, multiple scattering, and the finite production opening angle will slightly degrade this resolution. The exact error on the photon energy will be calculated later using a Monte Carlo simulation. Trajectories for positrons generated on the beam axis with the minimum and maximum momentum for each counter were calculated analytically. The distance from the beam axis to the counter and the counter width is then calculated using these trajectories. Table 7.2 summarizes the design of the FSF hodoscope. The individual counters varies from 6 to 11 mm in width and the distance from the beamline to inner edge of the first counter is 0.554 m. The distances given in Table 7.2 are from the beamline to the lower momentum edge of the counter.

The uncertainty in the photon energy and the energy resolution are given by

$$\sigma_\gamma = (\sigma_+^2 + \sigma_-^2)^{1/2} \tag{7.1}$$

$$\sigma_\gamma/E_\gamma = (\sigma_+^2 + \sigma_-^2)^{1/2}/(E_+ + E_-). \tag{7.2}$$

where σ_γ is the uncertainty in the photon energy, σ_+ and σ_- are the uncertainties in the positron and electron energies, and E_+ and E_- are the positron and

Counter Name	$\mathrm{p}_{\mathrm{MAX}}$	$\mathrm{p}_{\mathrm{MIN}}$	$\delta\mathrm{p}_e$	Distance to beamline	Counter Width
	GeV/c	GeV/c	MeV/c	m	mm
WSF1	3.3089	3.2500	17.00	0.690	13.08
WSF2	4.3089	4.2500	17.00	0.520	7.38
WSF3	5.3089	5.2500	17.00	0.419	4.76
WSF4	6.3089	6.2500	17.00	0.350	3.33
WSF5	7.3089	7.2500	17.00	0.301	2.46
WSF6	8.3089	8.2500	17.00	0.264	1.89

Table 7.3: Summary of the design of the wide spaced forward (WSF) hodoscope. the nominal momentum range, nominal resolution,and counter width are shown.

electron energies. It is clear from the above equations that once the segmentation and therefore the resolution of the FSF has been chosen the optimum design of the WSF is highly constrained. The FSF counters are designed to cover 41.67 MeV/c each resulting in a constant positron momentum resolution of 12 MeV/c. The wide spaced front WSF scintillators are designed such that each counter covers a fixed momentum span. This ensures that the uncertainty in each photon bin is roughly constant. The momentum range for each counter is chosen so that the final uncertainty in the photon energy is equal to 1/2 the momentum bin width in the FSF. The WSF counters widths are then adjusted so that the nominal uncertainty in the photon energy is given by

$$\sigma_\gamma = (\text{FST momentum bin width})/2 = 20.8 \text{ MeV} \tag{7.3}$$

In order to achieve this each counter must have an energy resolution of $\sigma_- = \sqrt(\sigma_\gamma^2 + \sigma_+^2) = 17\text{MeV}$ which requires a momentum span of $\Delta p = 17 \times \sqrt{12} = 58.9$ MeV. Table 7.3 summarizes the design of the WSF scintillator hodoscope. Similar to Table 7.2, electron trajectories are calculated for electrons generated on the photon beam axis with momenta corresponding to the bin edges, in order to compute the counter positions and widths. The width of a counter ranges from 13.1 mm for 3 GeV/c electrons to 1.9 mm for 8 GeV/c electrons. WSF6 is the counter in this design closest to the photon beam axis. With the 30D72 magnet and a 1.5 m drift distance this counter is placed 0.264 m from the beamline.

A detailed Monte Carlo has been developed to study the pair spectrometer described above. Figure 7.2 shows the volumes modeled in GEANT. The converter target in this model is located 2.5 m upstream of the dipole magnet which is the largest distance considered. The inner dimensions of the dipole magnet correspond to the dimensions of the vacuum chamber which fits in the gap. The vacuum chamber downstream of the magnet is modeled with 6 mm thick stainless steel walls and a 250 μm thick Kapton exit window. Each individual scintillator is modeled with the correct width dimensions and distance to the beamline. 10 mm thick scintillators are modeled presently. The scintillators in the present model are not rotated to match the electron/positron bending angle. In the next version of the simulation the counter thickness will be reduced to 5 mm and the counters will be rotated to the correct angle. One meter downstream of the first hodoscope is a row of lead bricks placed in the horizontal plane for shielding. Behind the lead wall are 8 large iron blocks for additional shielding. The Monte Carlo simulation also includes the collimation system upstream of the pair spectrometer. The simulation starts the photon beam upstream of the first collimator and uses the detailed model of the coherent and incoherent bremsstrahlung flux generated in the diamond radiator based on the expected emittance of the CEBAF 12 GeV electron beam. This accurately models the position and angular spread of the photon beam in addition to producing a realistic photon flux function $\mathrm{I}_\gamma^{\mathrm{coll}}(\mathrm{E})$. It also includes background generated in the collimators and windows.

With an accurate model of the photon beam the rates and resolutions of the pair spectrometer can be properly computed. The effects of the beam spot size on the converter target, multiple scattering, and the pair production opening angle are correctly taken into account and can be studied. In Figure 7.3 the coincidence rate in each of the 144 energy bins is plotted. In this simulation a photon flux to GlueX of 10^8 photons per second in the coherent peak and a pair spectrometer converter target thickness of $\mathrm{X}_0 = 5 \times 10^{-3}$ were assumed. The energy spectrum is now dominated by the coherent bremsstrahlung component. As seen in Figure 7.3, the coincidence rate near the coherent peak is about 250 Hz while the energy bins far from incoherent bremsstrahlung have rates of 25 to 50 Hz. For a converter thickness of $\mathrm{X}_0 = 1 \times 10^{-3}$ the rate would be about 50 Hz at the coherent peak and 5 to 10 Hz away from the peek. Under these conditions a measurement of the energy spectrum with 1% accuracy will take about 15 minutes. The total count rate of all coincidences is about 10 kHz for 10^8 photons/s which is acceptable for the GlueX data acquisition system. Near the endpoint the rate is a few Hz making an endpoint measurement possible. These rates will reduce somewhat when the correct counter thickness and rotation angle are used.

The momentum resolution as a function of energy is plotted in Figure 7.4 for the FSF and WSF. For every event which produced a coincidence between the FSF and WSF hodoscopes, the generated electron and photon energy were recorded. The momentum resolution is then taken to be the RMS of the distribution for each counter. The resolution for the FSF ranges from 15.5 to 18.5 MeV in this simulation compared to the expected 12 MeV. The WSF resolution ranges between 23 and 47 MeV compared with 17 MeV . Most the degradation in resolution comes from not rotating the counters to be perpendicular to the electron and positron trajectories. In the next version of the Monte Carlo this will be corrected. Even with this sub-optimal model photon resolutions of 28 to 50 MeV are achieved.

Accidental coincidences were also studied. The accidental rate could be reduced to about 1% if two simple lead wedges are placed outside the 3 GeV/c particle trajectory. These wedges shield the counters from low energy particles which would otherwise shower on the wall of the vacuum chamber. The accidental rate from particles back scattering from the lead and iron shielding is low. The background rate in the GlueX detector from the collimator cave and the pair spectrometer is estimated to be twice the cosmic ray background rate.

The entire pair spectrometer consists of a total of 42 counters: FSF(24), FSB(4), WSF(6), and WSB(6). In Figures 7.5 and 7.6 the implementation of the readout based on GlueX standard electronics is presented. The scintillators are read out using photomultiplier tubes which are powered by a CAEN SY2527 based high voltage system. The signals from the FSF and WSF are discriminated using CAEN V812 constant fraction discriminators and then readout using the F1TDC. The backward layer hodoscopes are used to form the pair spectrometer trigger and are readout with the fADC250 operating in "HIT BIT Mode". A bit pattern containing the information as to which of the back hodoscope channels was hit is formed in the fADC250 and passed to the crate trigger processor (CTP). The CTP passes this information to the subsystem processor (SSP) and the SSP passes it to the global trigger processor (GTP). The GTP checks for coincidences between the WSB and FSB hodoscopes and generates a pair spectrometer trigger if one is found.

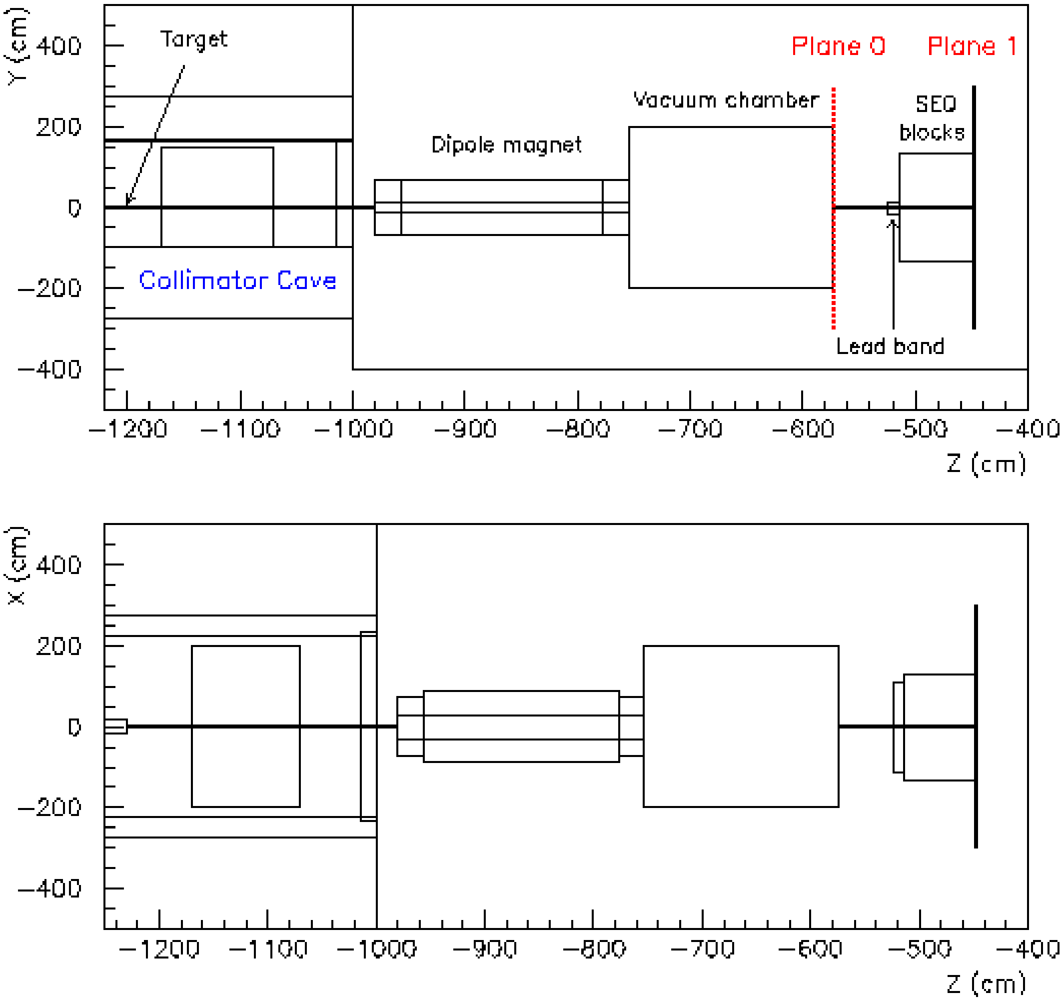

Figure 7.2: The model of the pair spectrometer which is implemented in GEANT is shown. The top panel is a side view of the GEANT volumes and the lower panel is the top view. The pair spectrometer converter is placed 12 m upstream of GlueX in this model. The dipole magnet is located at the entrance to Hall-D and is followed by a vacuum chamber. The hodoscopes are located in plane 0. A lead wall followed by large iron blocks then shield GlueX from the produced e^+/e^- pairs. z=0 in GlueX coordinates is located at the upstream edge of the solenoid magnet.

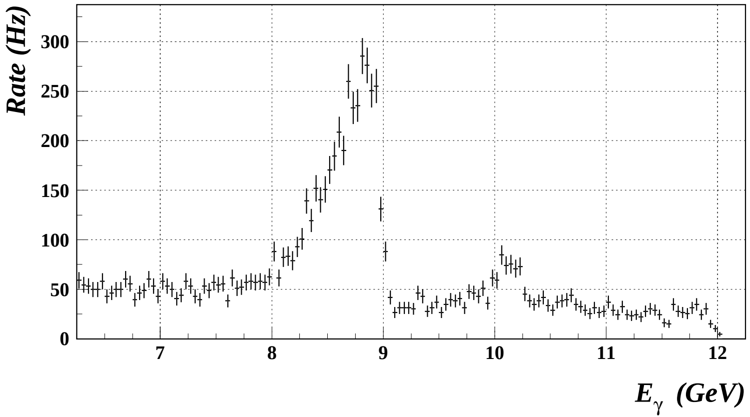

Figure 7.3: The rates for each of the 144 energy bins is plotted. In this simulation a photon flux to GlueX of 10^8 photons per second in the coherent bremsstrahlung region and a pair spectrometer converter target thickness of $X_0 = 5 \times 10^{-3}$ were used.

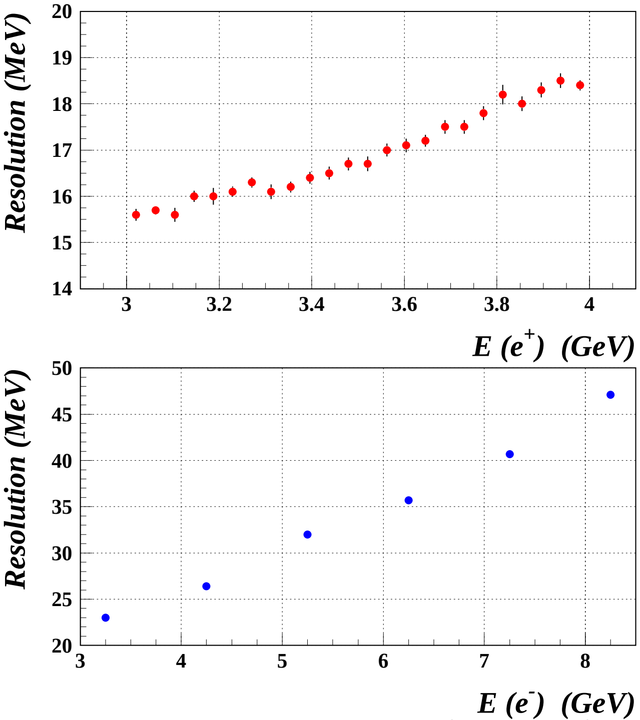

Figure 7.4: The uncertainty in the momentum for each of the 26 counters in the FSF (TOP panel) and 6 counters in the WSF (BOTTOM panel) is plotted versus the mean bin energy. The uncertainty was taken to be the RMS of the energy distribution for particles which strike the counter and form a left-right coincidence. A converter thickness of $X_0 = 5 \times 10^{-3}$ was simulated.

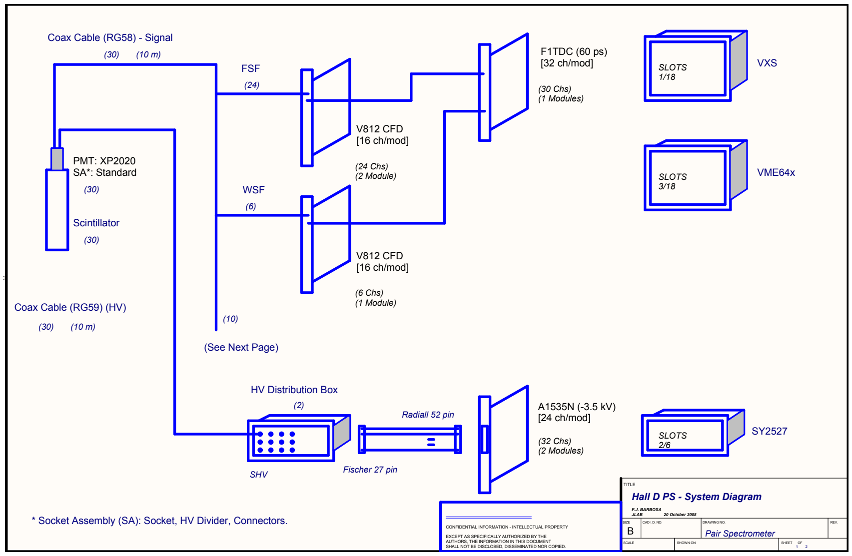

Figure 7.5: Electronics design for the readout of the pair spectrometer. The readout is based on the CAEN V812 constant fraction discriminators and the GlueX F1TDC.

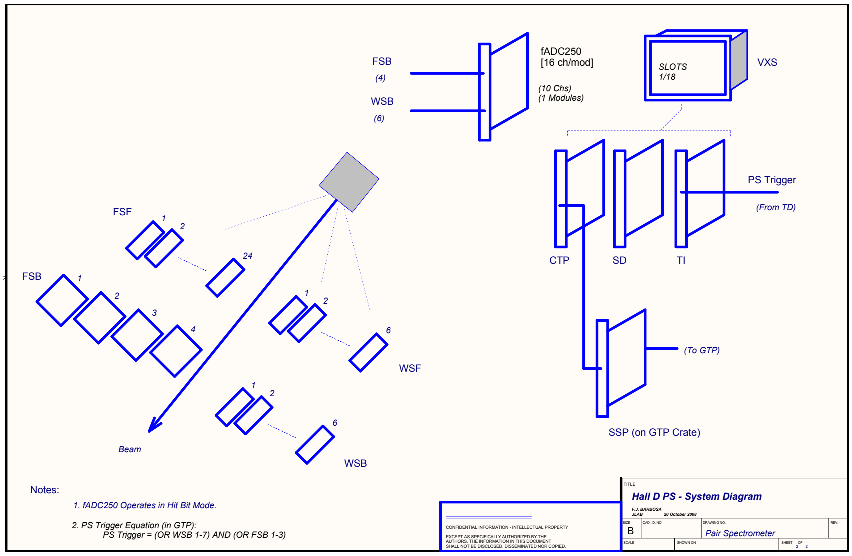

Figure 7.6: The electronics design of the pair spectrometer trigger. This trigger scheme is based on a GlueX fADC250 running in "Hit Bit Mode". The bit pattern corresponding to the hit trigger counters is passed to the GlueX trigger processing chain. The present trigger design is a simple left right OR.

7.4 A Possible Alternate Polarimeter

It is also possible to directly measure the polarization parameters – degree (P_γ) and direction (ϵ_γ) – of the collimated linearly polarized photon beam by measuring the azimuthal asymmetry in pair production. The asymmetry of the pair production process is well understood within theory (QED) and the measured beam asymmetry can be compared with theoretical expectations.

Implementing such a polarimeter would involve additional hardware components on the beamline between the collimator system and the GlueX detector. The converter for the pair spectrometer would have to be upgraded to include a scintillator target. Additionally a field free drift length followed by a detector package is needed. The pair spectrometer trigger counters are usable as the trigger for this polarimeter. Space is planned upstream of the pair spectrometer dipole for the insertion of the needed detectors if it is decided to build this instrument.

One possible implementation of this polarimeter consists of a thin scintillator ($d = 50\,\mu m$) as an active target, $1.5\,m$ in front of a silicon microstrip detector arrangement, followed by the pair spectrometer dipole magnet and two scintillators $10\,cm$ apart from the beamline for triggering on symmetric e^+e^- pairs. The microstrip detector needs four layers of silicon wafers with 512 channels each. The spatial width for a single channel is $25\,\mu m$. The second and third layer are oriented at $\pm 60^\circ$ with respect to the first layer, the fourth perpendicular to one of the previous layers, thus allowing to measure the full angular range of produced e^+e^--pairs without any gap in the acceptance. A Monte Carlo simulation of this device including multiple scattering in the target, the microstrip detector, and foils in the vacuum system (using GEANT) shows that an analyzing power of 25% is achievable (cf. fig 7.7). QED calculations predict an angular distribution for pair production proportional to $(1 + P_\gamma \alpha \cos 2(\phi - \epsilon_\gamma))$ with an analyzing power of $\alpha = 0.28$ for incident photons in the range of 6-10 GeV. Because of the thickness of the microstrip layers ($300\,\mu m$) and limitations due to radiation damage it is not possible to continuously measure the polarization using such a device. Instead the sensors and target would be inserted each time the orientation of the crystal radiator or the electron beam parameters have changed and a fifteen minute beam polarization measurement would be taken. The scintillator target as well as the detector device have to be mounted on motor driven stages so that they can be removed from the beamline. At present, due to budget constraints, this detector is not part of the scope of the project. However it is desired as a future upgrade.

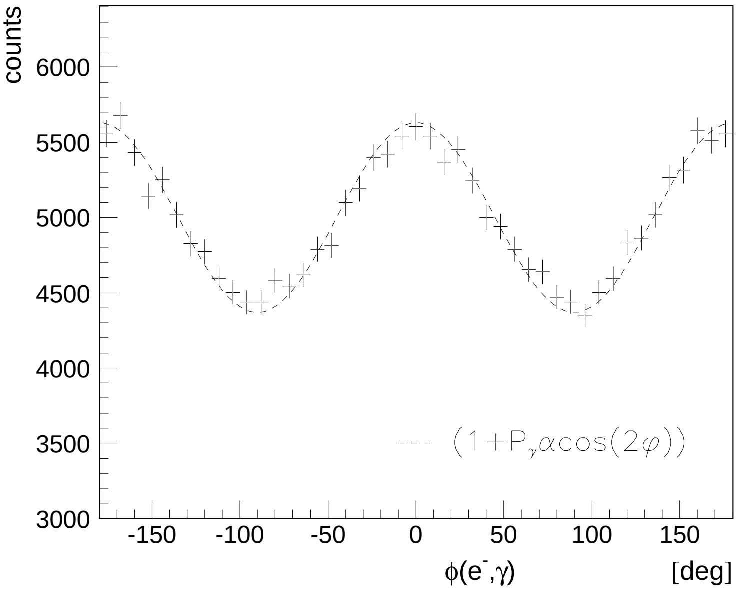

Figure 7.7: Angular distribution for pair production by linearly polarized photons as measured by a polarimeter in comparison with theoretical prediction (*dashed line*). The count rate corresponds to 15 minutes of data taking.

List of Figures

List of Tables

Bibliography

[1] C. Keppel. Development of a Compton-backscattered photon source for Hall B at Jefferson Lab. In Alex Dzierba, editor, *Physics with 8+ GeV Photons Workshop*, 1997. Workshop in Bloomington IN, July 14-16 1997, proceedings available from Jefferson lab.

[2] W. Kaune, G. Miller, W. Oliver, R.W. Williams, and K.K. Young. Inclusive cross sections for pion and proton production by photons using collimated coherent bremsstrahlung. *Phys. Rev.*, D**11**(3):478–494, 1975.

[3] H. Bilokon, G. Bologna, F. Celani, B. D'Ettorre Piazzoli, R. Falcioni, G. Mannocchi, and P. Picchi. Coherent bremsstrahlung in crystals as a tool for producing high energy photon beams to be used in photoproduction experiments at CERN SPS. *Nuclear Inst. and Meth.*, **204**:299–310, 1983.

[4] G. Diambrini-Palazzi. *Revs. Mod. Phys.*, **40**:611, 1968.

[5] U. Timm. *Fortschr. Phys.*, **17**:765, 1969.

[6] F. Mucklich and G. Petzow. Development of beryllium single crystal material for monochromator applications. *Mineral Processing and Extractive Metalurgy Review*, 13:193, 1994.

[7] S.L. Clewes, N. Perkins, M.L. Markham, H.K. Dhillon, I. Friel, D.J. Twitchen, and representing Element Six LTD G.A. Scarsbrook. Synthetic single crystal diamond: State of the art.

[8] A. Ueda, Y. Akahane, Y. Nishibayashi, and LTD. T. Imai, representing Sumitomo Electric Industries. Development and evaluation of a diamond electron source for electron beam instruments.

[9] J.D. Kellie, P.J.M. Clive, G.L. Yang, R. Beck, B.C. Evans, C. Gordon, C. Hall, J.W. Harris, R.T. Jones, D. Laundy, K. Livingston, I.J.D. MacGregor, J.C. McGeorge, J. Malone, A. Schmidt, P.A. Slaven, R.M. Vrcelj,

and D. Watts. The selection and performance of diamond radiators used in coherent bremsstrahlung experiments. *Nuclear Inst. and Meth.*, A**545**:164, 2005.

[10] K. Tamasaku, T. Ueda, D. Miwa, and Tetsuya Ishikawa. Goniometric and topographic characterization of synthetic iia diamonds. *J. Phys. D: Appl. Phys.*, **38**:A61, 2005.

[11] K. Livingston. The Stonehenge Technique. A new method for aligning coherent bremsstrahlung radiators.

[12] R. Schwitters. The slac coherent bremsstrahlung facility. *SLAC technical note*, SLAC-TN-70-32, 1970. (unpublished).

[13] J. Benesch and Y. Roblin Private Communication.

[14] P. Detiarenko E. Abkemeier and K. Welch. Shielding Basis for Hall D Complex. Technical Report JLab TN 08-033, Jefferson Lab., 2008.

[15] D. I. Sober, *et al. Nuclear Inst. and Meth.*, A**440**:263, 2000.

[16] G.Yang. Stress Analysis for the Hall D Tagger. Technical report, University of Glasgow, 2006. GlueX-doc-588.

[17] Anthony, *et al. Nuclear Inst. and Meth.*, A**301**:230, 1991.

[18] J. Hall, *et al. Nuclear Inst. and Meth.*, A**368**:689, 1996.

[19] R. Brun *et al.* GEANT Detector Description and Simulation Tool. Technical report, 1993. CERN Program Library.

[20] A. Snyder. `http://www.slac.stanford.edu/BFROOT/www/Computing./Offline/Simulation/gelhad.html`.

[21] P. V. Degtyarenko and M. V. Kossov. Monte Carlo program for nuclear fragmentation. Technical Report ITEP-11, 1992.

[22] P. V. Degtyarenko. Applications of the Photonuclear Fragmentation Model to Radiation Protection Problems. In *Proceedings of the Second Specialist's Meeting on Shielding Aspects of Accelerators, Targets and Irradiation Facilities (SATIF2)*, pages p.67–91., CERN, Geneva, Switzerland,, October 1995.

[23] E. Chudakov and A. Somov. Level-1 trigger of the GlueX experiment. Technical report, 2008. GlueX-doc-1137-v1.

[24] A. Somov. Simulation of Collimator Cave and Pair Spectrometer background. Technical report, 2008. GlueX-doc-1084-v1.